The immersed boundary projection method and its application to simulation and control of flows around low-aspect-ratio wings

Thesis by

Kunihiko Taira

In Partial Fulfillment of the Requirements
for the Degree of
Doctor of Philosophy

California Institute of Technology
Pasadena, California

2008

(Defended - May 13, 2008)

To my parents, Kunio and Yasuyo

Acknowledgements

My advisor, Professor Tim Colonius, is gratefully acknowledged for his support and teachings throughout my graduate studies. His passion for research and sharp eyes for analyzing flow physics have been a great source of inspiration. I have truly enjoyed the moments discussing numerical methods and fluid mechanics with him on the whiteboard and by the round table in his office. Professors Morteza Gharib, Melany Hunt, and John Dabiri have offered enlightening comments and graciously agreed to serve on my committee.

I was also fortunate to be involved in a multi-disciplinary research initiative (MURI), receiving insightful comments by Professors Clarence Rowley (Princeton Univ), David Williams (Illinois Inst of Tech), Gilead Tadmor (Northeastern Univ), and Doctor William Dickson. Funding for this research was provided by the US Air Force Office of Scientific Research and some of the computations were made possible by the US Department of Defense High Performance Computing Modernization Program.

I must also thank Professor Jay Frankel (Univ of Tenn) for his guidance during both my undergraduate and graduate studies. He certainly has been a great influence on me for pursuing graduate studies. Appreciation also goes to Professor Raj Pal Soni (Univ of Tenn) for teaching me a series of unforgettable courses in Mathematics.

My research experience would not have been this fruitful without the help from my laboratory members, especially, Guillaume Brès and Kristján Gudmundsson for their interesting and helpful comments on my research. I enjoyed stimulating

discussions with Eric Johnsen, Keita Ando, and Rick Burnes on fluid mechanics. Special thanks go to Jeff Krimmel and Jennifer Frank, who have been very kind and selfless in maintaining the computational resources. Won Tae Joe and Sunil Ahuja (Princeton Univ) are also thanked for patiently using my immersed boundary code and reporting bugs therein. Their inputs have been very valuable in improving the code.

Many of my other friends have made my life at Caltech enjoyable as well. Joseph Klamo and I sat together in many of the aeronautics courses (his note-taking skills were quite impressive). There were the three o'clock meetings with Mohamed El-Naggar and Kaushik Dayal that were just priceless. Tomonori Honda has helped me tremendously, particularly during my first year at Caltech, and has been a person I admire for his mathematical talent. Michael Wolf, Nicolas Hudson, Alexandros Taflanidis, and Chang Kook Oh have also been great friends. I cannot mention everyone here but I am thankful to all of those who have influenced me during my years at Caltech.

My parents, Kunio and Yasuyo Taira, have always supported and encouraged me in every choice I have made in life. I would not have been able to come this far without their constant support and care. Thank you. Appreciation also goes to my sister, Tomoko, for her support and occasional packages from Japan. With the completion of my graduate studies, I do hope I am able to make my father's old dream come true.

At last, the largest appreciation goes to my wonderful wife, Yuki, and my cheerful son, Kai, for their unconditional love. I am indebted to Yuki for her moving from New Zealand to Los Angeles to join me and offer warm support. She has always stood by me. My wife and son have been my joy and motivation. They have brightened me with their smiles and provided encouragement. I look forward to continuing cherishing the time with my family.

Abstract

The immersed boundary projection method and its application to simulation and control of flows around low-aspect-ratio wings

by

Kunihiko Taira

California Institute of Technology

First, we present a new formulation of the immersed boundary method that is algebraically identical to the traditional fractional step algorithm. This method, called the immersed boundary projection method, allows for the simulations of incompressible flows over arbitrarily shaped bodies under motion and/or deformation in both two and three dimensions. The no-slip condition along the immersed boundary is enforced simultaneously with the incompressibility constraint through a single projection. The boundary force is determined implicitly without any constitutive relations for the rigid body formulation, which in turn allows the use of high CFL numbers in our simulations compared to past methods.

Next, the above immersed boundary projection method is used to analyze three-dimensional separated flows around low-aspect-ratio flat-plate wings. A number of simulations highlighting the unsteady nature of the separated flows are performed for $Re = 300$ and 500 with various aspect ratios, angles of attack, and planform geometries. The aspect ratio and angle of attack are found to have a large influence on the stability of the wake profile and the force experienced by the low-aspect-ratio wing. At early times, following an impulsive start, topologies of the

wake vortices are found to be the same across different aspect ratios and angles of attack. Behind low-aspect-ratio rectangular plates, leading-edge vortices form and eventually separate as hairpin vortices following the start-up. This phenomenon is found to be similar to dynamic stall observed behind pitching plates. The detached structure would then interact with the tip vortices, reducing the downward velocity induced by the tip vortices acting upon the leading-edge vortex. At large time, depending on the aspect ratio and angles of attack, the wakes reach one of the three states: (*i*) a steady state, (*ii*) a periodic unsteady state, or (*iii*) an aperiodic unsteady state. We have observed that the tip effects in three-dimensional flows can stabilize the flow and also exhibit nonlinear interaction with the shedding vortices.

At last, we apply steady blowing to separated flows behind the low-aspect-ratio rectangular wings. The objective of the flow control is to enhance lift at post-stall angles of attack by changing the dynamics of the wake vortices. This controller strengthens the tip vortices by engulfing the trailing-edge vortex sheet to increase the downward thrust and the downward induced velocity onto the leading-edge vortices. The tip vortices that are traditionally considered as an aerodynamic nuisance, have been used favorably to increase lift in post-stall flows for the considered low-aspect-ratio wings.

Contents

List of Figures

List of Tables

Chapter 1

Introduction

1.1 Motivation and background

Traditionally most aerodynamic systems have been developed for steady operations. However, many biological systems have been observed to operate under *unsteady* conditions in low Reynolds number flows. For example, birds and insects use flapping motions to keep themselves aloft. Moreover, internal flows in cardiovascular systems are unsteady due to the periodic pumping of blood by the heart.

Analyzing such unsteady flows poses a great challenge to numerical simulations. In the majority of biological flows, the fluid evolves around or inside bodies of often complex geometries that are in motion and/or under deformation. Numerically speaking, spatial discretization (mesh generation) of these computational domains can become a problem by itself (Baker, 2005).

Regardless of using a structured or unstructured grid, a body-fitted discretization would have to be re-gridded at every time step if the body deforms or multiple bodies are in motion relative to each other. Since the generation of the mesh can become a large computational burden, it would be desirable to avoid re-gridding all together. One can also consider an overset method (Atta, 1981) that uses two sets of grids, say, a Cartesian grid for the outer flow field, and another

one that is fitted to the body. However, the need for re-gridding of the body-fitted mesh still exists for deforming bodies.

Here we explore methods that can be easily implemented into a widely available incompressible flow solver. In particular, we consider employing a simple Cartesian grid (Eularian) discretization over the entire domain including the immersed body and solving for the flow field using the well-known fractional step (projection) method to advance in time. Additionally, we let the body be discretized by a collection of surface points (Lagrangian), whose motion can either be prescribed or be based on some physics. At these Lagrangian points, regularized surface forces with appropriate magnitudes and directions are applied to enforce the no-slip boundary condition along the immersed surfaces.

With this approach, re-meshing is not required since only the location of the surface needs to be tracked. This method, the *immersed boundary method*, was originally introduced by Peskin (1972, 1977) to simulate the flows inside a heart. Based upon past immersed boundary methods (Peskin, 2002; Mittal & Iaccarino, 2005), here we present the *immersed boundary projection method* that is stable and does not require any *ad hoc* constitutive relations for simulations of flows around bodies with known surface velocities.

Equipped with the immersed boundary projection method, we are able to simulate various external flows around animals and internal biological flows. Of particular interest in this thesis are the three-dimensional flows around low-aspect-ratio wings in pure translation. Such flows are fundamental for understanding flows around flapping bio-flyers (Shyy *et al.*, 2008) as well as those over micro-air-vehicles (Mueller & DeLaurier, 2003). Here we focus on the unsteady nature of the separated flows and the corresponding forces generated by various low-aspect-ratio wings.

In addition, steady flow control is considered to alter the flow field around the low-aspect-ratio wing in a way that lift can be enhanced. The control study is exploratory in nature and is intended to investigate whether the formation and evolution of wake vortices can be modified by simple steady blowing. The

results are to motivate future studies on applying feedback control upon the three-dimensional flows to enhance lift in some optimal fashion.

The applications considered here do not exhibit the full capability of the method. We note that the current simulation method can compute flows around entire animals such as insects and jellyfish as well as small-scale underwater vehicles. Furthermore, one can simulate internal flows with an immersed object such as the red blood cells within blood vessels. Fluid-structure interactions can also be considered with this method. The flexibility of this simulation methodology has been one of the main reasons for the pursuing the immersed boundary method.

As this thesis is somewhat divided into the development of the numerical method and the analysis of the three-dimensional separated flows around the low-aspect-ratio wings, we have provided additional background information in each chapter to discuss further details on the subject in a more relevant manner.

1.2 Outline of this thesis

This thesis first introduces the immersed boundary projection method in Chapter 2. The derivation of this method is based upon the traditional fractional step/projection method used to solve for incompressible flows. Short discussions on the comparison of the current approach with previous methods are provided. Numerical examples are considered for the verification and validation of the method.

The later half of the thesis presents the applications of the immersed boundary projection method. In Chapter 3, we simulate low-Reynolds-number flows around low-aspect-ratio wings. This study highlights the unsteady nature of the separated flows behind the wings. Furthermore, we numerically implement steady flow control around low-aspect-ratio wings in Chapter 4. The objective is to enhance lift by changing the dynamics of the wake vortices in a way that voritcal forces can be used favorably. Steady blowing is found to achieve significant increase in lift by strengthening the tip vortices. The change in the wake structures is examined

and compared with the unactuated cases.

At last in Chapter 5, we offer some concluding remarks and suggestions for future directions of research in both the immersed boundary projection method and low-Reynolds-number flows.

1.3 Resulting publications

Based on the work described in this thesis, the following archival papers have been written:

- **Chapter 2**

  Taira, K. & Colonius, T. 2007 The immersed boundary method: a projection approach. *J. Comput. Phys.* **225**, 2118–2137.

- **Chapter 3**

  Taira, K. & Colonius, T. 2008 Three-dimensional separated flows around low-aspect-ratio flat plates. *J. Fluid Mech.* (submitted).

- **Chapter 4**

  Taira, K. & Colonius, T. 2008 On the effect of tip vortices in low-Reynolds-number post-stall flow control. (to be submitted).

- **Appendix B**

  Colonius, T. & Taira, K. 2008 A fast immersed boundary method using a nullspace approach and multi-domain far-field boundary conditions. *Comput. Methods Appl. Mech. Engrg.* **197**, 2131–2146.

Chapter 2

The Immersed Boundary Projection Method

2.1 Introduction

Immersed boundary methods have gained popularity for their ability to handle moving or deforming bodies with complex surface geometry (Peskin, 2002; Mittal & Iaccarino, 2005). Peskin (1972) first introduced the method by describing the flow field with an Eulerian discretization and representing the immersed surface with a set of Lagrangian points. The Eulerian grid is not required to conform to the body geometry as the no-slip boundary condition is enforced at the Lagrangian points by adding appropriate boundary forces. The boundary forces that exist as singular functions along the surface in the continuous equations are described by discrete delta functions that smear (regularize) the forcing effect over the neighboring Eulerian cells.

Peskin originally used the immersed boundary method to simulate blood flow inside a heart with flexible valves, where the forcing function was computed by Hooke's law (Peskin, 1972, 1977). This technique was later extended to rigid bodies by taking the spring constant be a large value (Beyer & LeVeque, 1992; Lai & Peskin, 2000). Goldstein *et al.* (1993) applied the concept of feedback

control to compute the force on the rigid immersed surface. The difference between the velocity solution and the boundary velocity is used in a proportional-integral controller. For the aforementioned techniques to model flow over rigid bodies, the choice of gain (stiffness) remains *ad hoc* and large gain results in stiff equations. Our intention is to remove all tuning parameters and formulate the immersed boundary method in a general framework for rigid bodies (as well as bodies with prescribed surface motion).

In our formulation, we treat the boundary forces in a manner analogous to the discretized pressure. For the incompressible Navier-Stokes equations, pressure may be viewed as a Lagrange multiplier required to satisfy the divergence-free constraint. Similarly, boundary forces can be regarded as Lagrange multipliers that satisfy the no-slip constraint (Glowinski *et al.*, 1998). By introducing regularization and interpolation operators and grouping the pressure and force unknowns together, the discretized incompressible Navier-Stokes equations can in fact be formulated with a structure algebraically identical to the traditional fractional step method. Although previous research has implemented immersed boundary techniques with the traditional fractional step algorithm, the entire immersed boundary method itself has not been regarded as a fractional step (projection) method, as reported here. We follow the algebraic approach of Perot (1993), where the fractional step method is written as a block-LU decomposition.

In the next section, we review the traditional fractional step method as it is the fundamental basis for our immersed boundary method. In Section 2.3, we introduce the immersed boundary projection method. This formulation is compared to previous methods in Section 2.4; namely the original immersed boundary method (Peskin, 1972), the direct forcing method (Mohd-Yusof, 1997), the immersed interface method (Lee & LeVeque, 2003), and the distributed Lagrange multiplier method (Glowinski *et al.*, 1998). In Section 2.5, numerical examples are considered to assess the temporal and spatial accuracy of the current method. Flows over stationary and moving cylinders are simulated and results are compared to previous experimental and numerical studies. Section 2.6 summarizes

the current formulation. Further details on the discretization of the immersed boundary projection method are placed in Appendix A.

2.2 Fractional step methods

We consider the incompressible Navier-Stokes equations

$$\frac{\partial \mathbf{u}}{\partial t} + \mathbf{u} \cdot \nabla \mathbf{u} = -\nabla p + \frac{1}{Re} \nabla^2 \mathbf{u}, \tag{2.1}$$

$$\nabla \cdot \mathbf{u} = 0, \tag{2.2}$$

where $\mathbf{u}$, p, and Re are the suitably non-dimensionalized velocity vector, pressure, and the Reynolds number, respectively. Following references (Chorin, 1968; Témam, 1969; Kim & Moin, 1985; Perot, 1993; Chang *et al.*, 2002), the equations are discretized with a staggered-mesh finite volume formulation using the implicit Crank-Nicolson integration for the viscous terms and the explicit second-order Adams-Bashforth scheme for the convective terms. This produces an algebraic system of equations,

$$\begin{bmatrix} A & G \\ D & 0 \end{bmatrix} \begin{pmatrix} q^{n+1} \\ p \end{pmatrix} = \begin{pmatrix} r^n \\ 0 \end{pmatrix} + \begin{pmatrix} bc_1 \\ bc_2 \end{pmatrix}, \tag{2.3}$$

where q^{n+1} and p are the discretized velocity flux and pressure vectors. The discrete velocity can be recovered by $u^{n+1} = R^{-1} q^{n+1}$, where R is a diagonal matrix that transforms the discrete velocity into the velocity flux. Sub-matrices G and D correspond to the discrete gradient and divergence operators, respectively. The operator resulting from the implicit velocity term is $A = \frac{1}{\Delta t} M - \frac{1}{2} L$, where M is the (diagonal) mass matrix and L is the discrete (vector) Laplacian. We construct the Laplacian to be symmetric, hence making A symmetric as well. The right-hand side of Eq. (2.3) consists of the explicit terms from the momentum equation, r^n, and inhomogeneous terms from the boundary condition, bc_1 and bc_2. Details on the discretization of Eqs. (2.1) and (2.2) can be found in Appendix A

and in the works of Perot (1993) and Chang *et al.* (2002). It is interesting to note that $G = -D^T$ for the staggered grid formulation.

The traditional fractional step method by Chorin (1968) and Témam (1969) was introduced to solve Eq. (2.3) in an efficient manner by using an approximation for A^{-1}. In the present analysis, we adopt the observation made by Perot (1993) that the fractional step method can be regarded as an LU decomposition of Eq. (2.3):

$$\begin{bmatrix} A & 0 \\ -G^T & G^T B^N G \end{bmatrix} \begin{bmatrix} I & B^N G \\ 0 & I \end{bmatrix} \begin{pmatrix} q^{n+1} \\ p \end{pmatrix} = \begin{pmatrix} r^n \\ 0 \end{pmatrix} + \begin{pmatrix} bc_1 \\ bc_2 \end{pmatrix} + \begin{pmatrix} -\frac{\Delta t^N}{2^N}(LM^{-1})^N Gp \\ 0 \end{pmatrix}, \quad (2.4)$$

where B^N is the N-th order Taylor series expansion of A^{-1}:

$$\begin{aligned} A^{-1} &\cong B^N \\ &= \Delta t M^{-1} + \frac{\Delta t^2}{2}(M^{-1}L)M^{-1} + \cdots + \frac{\Delta t^N}{2^{N-1}}(M^{-1}L)^{N-1}M^{-1} \\ &= \sum_{j=1}^{N} \frac{\Delta t^j}{2^{j-1}}(M^{-1}L)^{j-1}M^{-1}. \end{aligned} \quad (2.5)$$

The last term in Eq. (2.4) is the leading order error resulting from the truncation in B^N. Let us note that B^N is symmetric and can be made positive-definite with appropriate choices of Δt and N (Perot, 1993). In the current situation, there also exists a second-order temporal discretization error from the second-order Adam–Bashforth and Crank–Nicolson methods. As discussed in Perot (1993), the fractional step error can be absorbed by the discrete pressure if LM^{-1} and G are commutative (for example, in the case of periodic domains); otherwise there remains an N-th order error.

Equation (2.4) is more commonly written in three steps:

$$Aq^* = r^n + bc_1, \qquad \text{(Solve for intermediate velocity)} \tag{2.6}$$

$$G^T B^N G p = G^T q^* + bc_2, \qquad \text{(Solve the Poisson equation)} \tag{2.7}$$

$$q^{n+1} = q^* - B^N G p. \qquad \text{(Projection step)} \tag{2.8}$$

Since both A and $G^T B^N G$ are symmetric positive-definite matrices, the conjugate gradient method can be utilized to solve the above momentum and Poisson equations in an efficient manner. In general, for non-symmetric matrices, various other Krylov solvers can be employed.

Here the discrete pressure is denoted by p without any superscript for its time level, as we regard pressure as a Lagrange multiplier (Chang *et al.*, 2002). There has been extensive discussion on the exact time level of the discrete pressure variable for various treatments of pressure in fractional step methods (Strikwerda & Lee, 1999; Brown *et al.*, 2001). For the present method, p is a first-order accurate approximation of pressure in time, vis. $p^{n+1/2}$. Since the first-order accuracy of p does not affect the temporal accuracy of the velocity variable (Perot, 1993), we use p as a simple representation of the pressure variable. If a second-order accurate pressure is desired, Brown *et al.* (2001) should be referred to for further modifications to the fractional step method.

Although a detailed stability analysis is not offered in this paper, we demonstrate that the present method described in the next section can stably solve for the flow field for CFL numbers up to 1, as shown in Section 2.5. We mention that fractional step methods for incompressible flow can suffer numerical instability if Δt is decreased arbitrarily (Guermond & Quartapelle, 1998). The time step is limited by a lower bound of $\Delta t \geq c\Delta x^{l+1}$ if equal orders of interpolation are used for velocity and pressure, as in the present case (c is a constant and l is the interpolation order of velocity, here $l = 2$). While remedies are offered in Guermond & Quartapelle (1998) and Codina (2001), we have not utilized them here since a much larger Δt is usually selected based on the CFL constraint.

We note in passing that the form of Eq. (2.3) is known as the Karush-Kuhn-Tucker (KKT) system that appears in constrained optimization problems (Nocedal & Wright, 1999). This system minimizes a term similar to the kinetic energy:

$$\min_{q^{n+1}} \left[\frac{1}{2} (q^{n+1})^T A q^{n+1} - (q^{n+1})^T (r^n + b c_1) \right] \quad \text{subject to} \quad D q^{n+1} = 0 + b c_2. \tag{2.9}$$

It is interesting that the discrete pressure p does not play a direct role in time advancement, but acts as a set of Lagrange multipliers to minimize the system energy and satisfy the kinematic constraint of divergence-free velocity field.

2.3 The immersed boundary projection method

2.3.1 The discretized Navier-Stokes equations with boundary force

Since the discretized Navier-Stokes equations, Eq. (2.3), are observed to be a KKT system with pressure acting as a set of Lagrange multipliers to satisfy the continuity constraint, one can imagine appending additional algebraic constraints by increasing the number of Lagrange multipliers. Hence we incorporate the no-slip constraint from the immersed boundary method into the fractional step framework.

The immersed boundary method introduces a set of Lagrangian points, $\boldsymbol{\xi}_k$, that represent the surface, $\partial\mathcal{B}$, of an immersed object, $\mathcal{B}$, within a computational domain, $\mathcal{D}$, whose geometry need not conform to the underlying spatial grid. At the Lagrangian points, appropriate surface forces, $\mathbf{f}_k$, are applied to enforce the no-slip condition along $\partial\mathcal{B}$. Figure 2.1 illustrates the setup of the spatial discretization. Since the location of the Lagrangian boundary points does not necessarily coincide with the underlying spatial discretization, two operators are required: one that passes information from the boundary points to the neighboring staggered grid points and another one that conveys information in the opposite direction.

We consider the continuous version of the incompressible Navier-Stokes

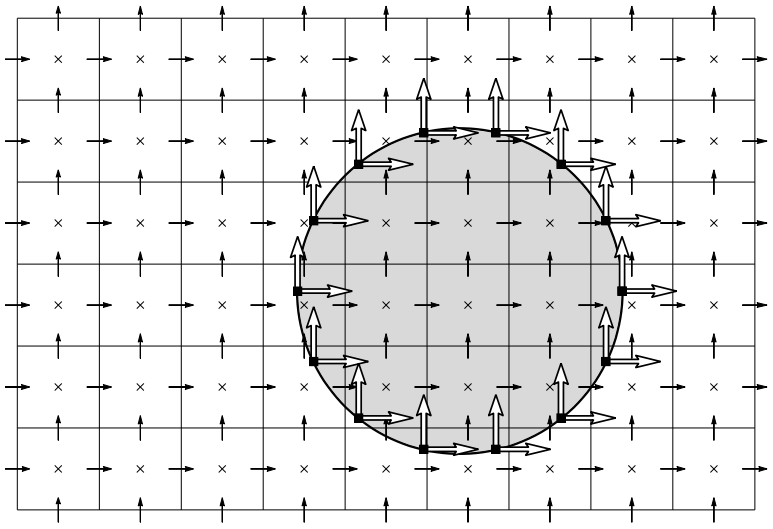

Figure 2.1: Staggered grid discretization of a two-dimensional computational domain $\mathcal{D}$ and immersed boundary formulation for a body $\mathcal{B}$ depicted by a shaded object. The horizontal and vertical arrows ($\rightarrow, \uparrow$) represent the discrete u_i and v_i velocities locations, respectively. Pressure p_j is positioned at the center of each cell ($\times$). Lagrangian points, $\boldsymbol{\xi}_k = (\xi_k, \eta_k)$, along $\partial\mathcal{B}$ are shown with filled squares ($\blacksquare$) where boundary forces $\mathbf{f}_k = (f_{x,k}, f_{y,k})$ are applied ($\Rightarrow, \Uparrow$).

equations and explain how the immersed boundary method can be discretized into a KKT system and solved with a fractional step/projection algorithm. The incompressible Navier-Stokes equations with a boundary force, $\mathbf{f}$, and the no-slip condition can be considered as the continuous analog of the immersed boundary method

$$\frac{\partial \mathbf{u}}{\partial t} + \mathbf{u} \cdot \nabla \mathbf{u} = -\nabla p + \frac{1}{Re}\nabla^2 \mathbf{u} + \int_s \mathbf{f}\left(\boldsymbol{\xi}(s,t)\right) \delta(\boldsymbol{\xi} - \mathbf{x}) ds, \tag{2.10}$$

$$\nabla \cdot \mathbf{u} = 0, \tag{2.11}$$

$$\mathbf{u}(\boldsymbol{\xi}(s,t)) = \int_{\mathbf{x}} \mathbf{u}(\mathbf{x}) \delta(\mathbf{x} - \boldsymbol{\xi}) d\mathbf{x} = \mathbf{u}_B(\boldsymbol{\xi}(s,t)), \tag{2.12}$$

where $\mathbf{x} \in \mathcal{D}$ and $\boldsymbol{\xi}(s,t) \in \partial\mathcal{B}$. The boundary $\partial\mathcal{B}$, parametrized by s, is allowed to move at a velocity $\mathbf{u}_B(\boldsymbol{\xi}(s,t))$. Convolutions with the Dirac delta function δ are used to allow the exchange of information from $\partial\mathcal{B}$ to $\mathcal{D}$ and *vice versa* in Eqs. (2.10) and (2.12), respectively.

The discretization of the above system results in

$$\begin{bmatrix} A & G & -H \\ D & 0 & 0 \\ E & 0 & 0 \end{bmatrix} \begin{pmatrix} q^{n+1} \\ p \\ f \end{pmatrix} = \begin{pmatrix} r^n \\ 0 \\ u_B^{n+1} \end{pmatrix} + \begin{pmatrix} bc_1 \\ bc_2 \\ 0 \end{pmatrix}, \tag{2.13}$$

where Hf corresponds to the last term in Eq. (2.10) with $f = (f_x, f_y)^T$. Similar to the discrete pressure, we do not place a superscript for time level on f to emphasize its role as a Lagrange multiplier. The no-slip condition, Eq. (2.12), is enforced using the constraint, $Eq^{n+1} = u_B^{n+1}$. Here A, G, and D are the implicit operator for the velocity flux, the discrete gradient operator, and the discrete divergence operator, respectively, and r^n, bc_1, and bc_2 are the explicit terms in the momentum equation, the boundary condition vector resulting from the Laplacian operator, and the boundary condition vector generated from the divergence operator, respectively. Note that these sub-matrices and vectors (A, G, D, r^n, bc_1, and bc_2) are identical to those that appear in the traditional fractional step method, Eq. (2.3).

The two additional sub-matrices H and E are introduced to regularize (smear) the singular boundary force over a few cells and interpolate velocity values defined on the staggered grid onto the Lagrangian points, respectively. We will refer to these sub-matrices as *regularization* (H) and *interpolation* (E) operators. The precise expressions of these operators are discussed below and details on the overall discretization are provided in Appendix A.

2.3.2 Interpolation and regularization operators

The operators H and E are constructed from the regularized discrete delta function. Among the variety of discrete delta functions available, we choose to use the one by Roma *et al.* (1999) which is specifically designed for use on staggered grids (where even/odd de-coupling does not occur). This function has the form:

$$d(r) = \begin{cases} \frac{1}{6\Delta r}\left[5 - 3\frac{|r|}{\Delta r} - \sqrt{-3\left(1 - \frac{|r|}{\Delta r}\right)^2 + 1}\right] & \text{for } 0.5\Delta r \leq |r| \leq 1.5\Delta r, \\ \frac{1}{3\Delta r}\left[1 + \sqrt{-3\left(\frac{r}{\Delta r}\right)^2 + 1}\right] & \text{for } |r| \leq 0.5\Delta r, \\ 0 & \text{otherwise,} \end{cases} \tag{2.14}$$

where Δr is the cell width of the staggered grid in the r-direction. This discrete delta function is supported over only three cells, which is an advantage for computational efficiency. We have not found significant differences in the results for the current formulation with alternative discrete delta functions. References by Peskin (2002) and Beyer & LeVeque (1992) may be consulted for a variety of delta functions.

As observed by Peskin (1972) and Beyer & LeVeque (1992), discrete delta functions can be used both for regularization and interpolation. The interpolation operator can be derived from discretizing the convolution of $\mathbf{u}$ and δ,

$$\mathbf{u}(\boldsymbol{\xi}) = \int_{\mathbf{x}} \mathbf{u}(\mathbf{x})\delta(\mathbf{x} - \boldsymbol{\xi})d\mathbf{x} \tag{2.15}$$

yielding

$$u_k = \Delta x \Delta y \sum_i u_i d(x_i - \xi_k) d(y_i - \eta_k) \tag{2.16}$$

for the two-dimensional case, where u_i is the discrete velocity vector defined on the staggered grid (x_i, y_i) and u_k is the discrete boundary velocity at the k-th Lagrangian point (ξ_k, η_k). For the three-dimensional case an extra factor of $\Delta z d(z_i - \zeta_k)$ is needed. Letting α denote the factor preceding the summation, the interpolation operator for Eq. (2.16) can be written as:

$$\hat{E}_{k,i} = \alpha d(x_i - \xi_k) d(y_i - \eta_k), \tag{2.17}$$

so that the no-slip condition is represented by

$$\hat{E}_{k,i} u_i^{n+1} = E_{k,i} q_i^{n+1} = u_B{}_k^{n+1}, \tag{2.18}$$

where $E \equiv \hat{E} R^{-1}$ to allow the use of the flux, $q^{n+1} = R u^{n+1}$, from the fractional-step formulation. The hat is used to represent the original operator and is removed once a transformation (e.g., R^{-1}) is applied.

Similarly, the regularization operator is a discrete version of the convolution operator in Eq. (2.10) that passes information from the Lagrangian points, $\boldsymbol{\xi}_k$, to the neighboring staggered grid points, $\mathbf{x}_i$. Defining H in a manner similar to E, we obtain

$$\begin{aligned} H_{i,k} &= \beta \hat{M}_i d(\xi_k - x_i) d(\eta_k - y_i) \\ &= \frac{\beta}{\alpha} \hat{M}_i \hat{E}_{k,i}^T, \end{aligned} \tag{2.19}$$

where β is the numerical integration factor proportional to ds. Note that a diagonal matrix $\hat{M}$ is included for consistency with the fractional step formulation. It should be observed that E and H are symmetric up to a constant if the diagonal matrices R^{-1} and $\hat{M}$ are absent.

Next, let us achieve symmetry between the (3,1) and (1,3) block entries in the presence of R^{-1} and $\hat{M}$ in Eq. (2.13). We absorb the offset in scaling into

the unknown boundary force by introducing a transformed forcing function $\tilde{f}$ that satisfies

$$Hf = -E^T \tilde{f}. \tag{2.20}$$

The original boundary force can be retrieved by $f = -\text{inv}(EH)EE^T\tilde{f}$. In the case of using a uniform Cartesian grid with $\Delta x = \Delta y$, the relation simplifies to $f = -\frac{1}{\Delta x^2}\frac{\alpha}{\beta}\tilde{f}$.

The discrete delta function of Eq. (2.14) currently requires the use of a uniform grid in the vicinity of $\partial\mathcal{B}$ to satisfy a set of properties (e.g., moment conditions) (Roma *et al.*, 1999). Since the range and domain of E and H are only limited to the neighborhood of $\partial\mathcal{B}$, non-uniform discretization can still be applied away from the body. Although it is not pursued here, it would be interesting to generate discrete delta functions that are suitable for a non-uniform spatial discretization around the immersed body.

Note that symmetry between E and H is not necessary for discretization, but it allows us to solve the overall system in an efficient manner. There are unexplored possibilities using different discrete delta functions for interpolation and regularization operators. Beyer & LeVeque (1992) consider such cases in a one-dimensional model problem.

2.3.3 The immersed boundary projection method

Now that we have formulated the sub-matrices G and D such that $D = -G^T$ and introduced a transformed force, $\tilde{f}$, the overall system of equations, Eq. (2.13), becomes

$$\begin{bmatrix} A & G & E^T \\ G^T & 0 & 0 \\ E & 0 & 0 \end{bmatrix} \begin{pmatrix} q^{n+1} \\ p \\ \tilde{f} \end{pmatrix} = \begin{pmatrix} r^n \\ 0 \\ u_B^{n+1} \end{pmatrix} + \begin{pmatrix} bc_1 \\ -bc_2 \\ 0 \end{pmatrix}. \tag{2.21}$$

As previously discussed, both the discrete pressure and boundary forcing functions are Lagrange multipliers and, algebraically speaking, it is no longer necessary to make a distinction between the two. Thus organizing the sub-matrices

and vectors in Eq. (2.21) in the following fashion:

$$Q \equiv [G,\ E^T], \quad \lambda \equiv \begin{pmatrix} p \\ \tilde{f} \end{pmatrix}, \quad r_1 \equiv r^n + bc_1, \quad r_2 \equiv \begin{pmatrix} -bc_2 \\ u_B^{n+1} \end{pmatrix}, \tag{2.22}$$

Eq. (2.21) can be simplified to a KKT system

$$\begin{bmatrix} A & Q \\ Q^T & 0 \end{bmatrix} \begin{pmatrix} q^{n+1} \\ \lambda \end{pmatrix} = \begin{pmatrix} r_1 \\ r_2 \end{pmatrix}, \tag{2.23}$$

which is now in a form identical to Eq. (2.3), providing motivation to apply the same fractional step technique in solving the overall system as in Section 2.2. Performing an LU decomposition of Eq. (2.23),

$$\begin{bmatrix} A & 0 \\ Q^T & -Q^T B^N Q \end{bmatrix} \begin{bmatrix} I & B^N Q \\ 0 & I \end{bmatrix} \begin{pmatrix} q^{n+1} \\ \lambda \end{pmatrix} = \begin{pmatrix} r_1 \\ r_2 \end{pmatrix} + \begin{pmatrix} -\frac{\Delta t^N}{2^N}(LM^{-1})^N Q\lambda \\ 0 \end{pmatrix}. \tag{2.24}$$

As in the original fractional step method, there is an N-th order splitting error. Note that this error cannot be absorbed by the Lagrange multiplier, λ, because LM^{-1} and Q do not commute (even for periodic domains). Hence, a third-order expansion for B^N is recommended, as discussed in Perot (1993) and Section 2.5.

Thus, the immersed boundary projection method consists of the same three steps as Eqs. (2.6) to (2.8) but with λ replacing p and Q replacing G:

$$Aq^* = r_1, \qquad \text{(Solve for intermediate velocity)} \tag{2.25}$$

$$Q^T B^N Q\lambda = Q^T q^* - r_2, \qquad \text{(Solve the modified Poisson equation)} \tag{2.26}$$

$$q^{n+1} = q^* - B^N Q\lambda. \qquad \text{(Projection step)} \tag{2.27}$$

The main differences between the present and the traditional fractional step methods are in the Poisson equation and the projection step. Here, the pressure and boundary force are determined implicitly from the modified Poisson equation. The projection step removes the non-divergence-free and slip components of the

velocity from the intermediate velocity field in one step. The numerical constraint of no-slip exists only at the Lagrangian points, hence making the dimensions of H and $\tilde{f}$ considerably smaller than those of G and p. Thus it is encouraging that there is no significant increase in size of $Q^T B^N Q$ in the modified Poisson equation from $G^T B^N G$ in the classical fractional step method.

We can still solve Eqs. (2.25) and (2.26) with the conjugate gradient method as both left-hand side operators are symmetric and positive-definite. Some care must be taken to make $Q^T B^N Q$ positive-definite and well-conditioned. First, as in the traditional fractional step method, one of the discrete pressure values must be pinned to a certain value to remove the zero eigenvalue.[1] Second, no repeating Lagrangian points are allowed to avoid $Q^T B^N Q$ from becoming singular[2]. Also, to achieve a reasonable condition number and to prevent penetration of streamlines caused by a lack of Lagrangian points, the distance between adjacent Lagrangian points, Δs, is set approximately to the Cartesian grid spacing.

In the case of moving immersed bodies, the location of the Lagrangian points must be updated at each time and so must E, i.e.,

$$E_{k,i} = E_{k,i}^{n+1} = E(\boldsymbol{\xi}_k(t^{n+1}), \mathbf{x}_i) \tag{2.28}$$

and similarly for H. These operators can be pre-computed at each time step by knowing the location of the Lagrangian points *a priori*. The current technique is not limited to rigid bodies and can model flexible moving bodies if we are provided with the location of $\partial\mathcal{B}$ at time level $n+1$. For deforming bodies, the volume of

[1] There are alternatives to pinning the solution of the modified Poisson equation. Bochev & Lehoucq (2005) discuss such techniques in detail for the Poisson equation with a Neumann boundary condition. Although the current staggered grid formulation does not require any *explicit* pressure boundary conditions, their analysis provides insight into the algebraic properties of the discretized Poisson equation.

[2] With two Lagrangian points at the same location, two of the column vectors of H (and correspondingly Q) become identical or linearly dependent. One can also observe that if the spacing between two Lagrangian points is small compared to the Eulerian grid spacing, the column vectors of H can become nearly linearly dependent.

the body must be isochoric to satisfy the incompressibility constraint. The current formulation treats the density of the body and the outer fluid to be equal to each other.

2.4 Comparison with other immersed boundary methods

Let us compare our current formulation with a few other immersed boundary methods, in particular the original immersed boundary method (Peskin, 1972), the direct forcing approach (Mohd-Yusof, 1997; Fadlun *et al.*, 2000), the immersed interface method (Lee & LeVeque, 2003), and the distributed Lagrange multiplier method (Glowinski *et al.*, 1998) to clarify the fundamental differences. Since we only select a few immersed boundary methods that are most similar to the current formulation, review articles by Peskin (2002) and Mittal & Iaccarino (2005) should be consulted for additional immersed boundary methods. The same notation introduced earlier is used in this section. Because the comparison of fundamental mechanisms for satisfying the no-slip condition along the immersed boundary is of interest here, we consider methods for simulating both rigid and elastic bodies. Some details such as the time integration schemes, the updating algorithms for the Lagrangian points, and the constitutive relations for the boundary forces are omitted for clarity of discussion. The discrete spatial operators and the temporal treatment of the discrete pressure variable may not be identical to our version but remain conceptually similar.

2.4.1 The original immersed boundary method

The original immersed boundary method (Peskin, 1972) is a modification to the traditional fractional step method, Eqs. (2.6–2.8), to simulate flow over a flexible body. An explicit boundary force term Hf^n computed with Hooke's law is added

to the right-hand side of the momentum equation.

$$Aq^* = r^n + bc_1 + Hf^n, \tag{2.29}$$

$$G^T B^N G p = G^T q^* + bc_2, \tag{2.30}$$

$$q^{n+1} = q^* - B^N G p. \tag{2.31}$$

At every time step, the location of the Lagrangian points on the elastic surface is updated. Although it is not considered here, a source/sink can be added to the pressure Poisson equation to apply a correction to the continuity equation (Kim *et al.*, 2001).

Let us discuss how the original immersed boundary method may conceptually be related to our method. Hooke's law can be written as: $\mathbf{f} = \kappa(\boldsymbol{\xi}^e - \boldsymbol{\xi})$, where κ is the spring constant and $\boldsymbol{\xi}^e$ is the equilibrium position for the boundary surface. If we are to differentiate and discretize this relation, we obtain:

$$\frac{f^{n+1} - f^n}{\Delta t} = \kappa \left(u_B^{n+1} - E q^{n+1} \right), \tag{2.32}$$

using the implicit Euler time discretization. Adding the boundary force to the momentum equation, we observe that the overall system has the form:

$$\begin{bmatrix} A & G & -H \\ D & 0 & 0 \\ E & 0 & \frac{1}{\kappa \Delta t} I \end{bmatrix} \begin{pmatrix} q^{n+1} \\ p \\ f^{n+1} \end{pmatrix} = \begin{pmatrix} r^n + bc_1 \\ bc_2 \\ u_B^{n+1} + \frac{1}{\kappa \Delta t} f^n \end{pmatrix}. \tag{2.33}$$

For rigid body simulations, $\kappa \gg 1$ is chosen to reduce the effect from the $(3,3)$ sub-matrix (Beyer & LeVeque, 1992; Lai & Peskin, 2000). In the limit of $\kappa \to \infty$, we recover our current formulation, Eq. (2.13). The above formulation, Eq. (2.33), has a structure identical to the artificial compressibility method (Chorin, 1967) that approximately satisfies the continuity equation with: $\frac{1}{a^2}\frac{\partial p}{\partial t} + \nabla \cdot \mathbf{u} = 0$, where a is an artificial speed of sound. This artificial parameter is typically set to a large value similarly to the spring constant, κ, in Eq. (2.33). Instead of Hooke's law,

a feedback controller ($\mathbf{f} = -\kappa_1 \int_0^t \mathbf{u}(\boldsymbol{\xi}, \tau) d\tau - \kappa_2 \mathbf{u}(\boldsymbol{\xi}, t)$) with large gains ($\kappa_1 \gg 1$ and $\kappa_2 \gg 1$) has also been used to compute the boundary force (Goldstein *et al.*, 1993), which results in an identical structure to Eq. (2.33).

However, large gains used in such constitutive relations add stiffness to the governing system, thus prohibiting the use of high CFL numbers. For instance, CFL numbers used in Lai & Peskin (2000) and Goldstein *et al.* (1993) are $\mathcal{O}(10^{-3})$ to $\mathcal{O}(10^{-1})$ for simulations of flow over a rigid circular cylinder. It is possible to use higher CFL numbers by lowering the gains at the expense of relaxing the no-slip condition. In contrast, the current projection method solves for the boundary force implicitly with no constitutive relations and behaves similarly to the traditional fractional step method in terms of temporal stability. Hence simulations can be performed with CFL numbers as high as 1, which is reported later in Section 2.5. In previous methods, it is not clear how the gains or the magnitude of the forcing function relate to how well the no-slip condition is satisfied[3]. On the other hand, our method satisfies the continuity equation and the no-slip condition exactly to machine precision or, if desired, to a prescribed tolerance.

2.4.2 The direct forcing method

The direct forcing method (Mohd-Yusof, 1997) approximates the boundary force for rigid bodies with an intermediate velocity field q^*. The force is not actually computed but implemented directly into the momentum equation by substituting the regularized no-slip condition near the immersed boundary. Conceptually

[3]Recently, there has been development on the stiffness issues in the original immersed boundary methods for elastic boundaries. Newren *et al.* (2007) and Mori & Peskin (2008) have been able to stably solve the overall equations with fluid-structure interactions through semi- and fully-implicit discretizations.

speaking, the momentum equation, Eq. (2.25), is modified to yield

$$\left(\tilde{M} - HE\right) Aq^* + \tfrac{1}{\Delta t} HEq^* = \left(\tilde{M} - HE\right)(r^n + bc_1) + \tfrac{1}{\Delta t} Hu_B^{n+1}, \tag{2.34}$$

$$G^T B^N G p = G^T q^* + bc_2, \tag{2.35}$$

$$q^{n+1} = q^* - B^N G p. \tag{2.36}$$

Here HE interpolates and then regularizes a vector, which acts as a filtering operator to extract the velocity field near $\partial\mathcal{B}$. A diagonal mass matrix $\tilde{M}$ is placed for scaling such that $\tilde{M} - HE \approx 0$ near $\partial\mathcal{B}$. Factors of $1/\Delta t$ are inserted in Eq. (2.34) to keep the order with respect to Δt consistent (note that $A = \mathcal{O}(1/\Delta t)$). Conceptually, the above equation becomes $Eq^* = u_B^{n+1}$ near the immersed boundary and reduces to $Aq^* = (r^n + bc_1)$ away from the body. The difference between the modified momentum equation, Eq. (2.34), and the momentum equation from the traditional fractional step method, Eq. (2.6), can be expressed as the boundary force for the direct forcing method:

$$f^{n+1} = \frac{u_B^{n+1} - Eq^*}{\Delta t} + EAq^* - E(r^n + bc_1). \tag{2.37}$$

Note that this method enforces the no-slip condition on q^* but not on q^{n+1}. A projection step is applied later to project the intermediate velocity, q^*, onto the solenoidal solution space. In order to satisfy the no-slip condition exactly, iterations over the entire fractional step algorithm is required for each time level. Although slip in q^{n+1} is reported to be small (Fadlun *et al.*, 2000), the magnitude of the error cannot be estimated in a deductive manner.

2.4.3 The immersed interface method

Next, we consider representing the immersed interface method (Lee & LeVeque, 2003) for elastic membranes in an algebraic form. In the immersed interface method, the boundary force is decomposed into tangential and normal components (f_τ and f_n, respectively). A regularized tangential component of the force, Hf_τ^n,

is included in the momentum equation as an explicit term and the explicit normal boundary force is implemented into the pressure Poisson equation in terms of a pressure jump condition across the interface. The overall method can be described as:

$$Aq^* = r^n + bc_1 + Hf_\tau^n, \tag{2.38}$$

$$G^T B^N G p = G^T q^* + bc_2 + G^T B^N b(f_n^n), \tag{2.39}$$

$$q^{n+1} = q^* - B^N(Gp - b(f_n^n)), \tag{2.40}$$

where $b = b(f_n^n([\![p]\!]))$ is a corrective term to calculate the pressure gradient $(Gp-b)$ taking the jump condition, $[\![p]\!]$, into consideration. Since the normal component of the boundary force is implemented directly into the pressure Poisson equation rather than in the momentum equation, a sharp velocity solution in the vicinity of the interface can be achieved resulting in second-order spatial convergence for some test problems. However, the construction of the correction term b requires explicit knowledge of the boundary force, and is not easily made implicit as desired in our formulation.

We note in passing that Linnick & Fasel (2005) recently developed a high-order immersed interface method that employs one-sided finite differences to obtain jump conditions for higher-order derivatives. Their results along with other numerical and experimental studies for flow over a stationary cylinder are compared to our results in Section 2.5.

2.4.4 The distributed Lagrange multiplier method

The most similar method to our formulation is the distributed Lagrange multiplier method by Glowinski *et al.* (1998) used in a variational principle (finite element) framework. Their work is closely related to ours as they introduce Lagrange multipliers (i.e., body force) on the immersed rigid body to satisfy the no-slip condition, essentially through projection. The main difference between our formulation and the distributed Lagrange multiplier method lies in how the

projection is applied to the velocity field.

Conceptually speaking, we consider the distributed Lagrange multiplier method as a different operator splitting applied to Eq. (2.13). Their overall system is solved with the Marchuk-Yanenko fractional step scheme (Yanenko, 1971; Marchuk, 1975) that decomposes the overall operations into three operators related to: (*i*) the divergence-free condition and pressure, (*ii*) the convective and diffusive operators, and (*iii*) the no-slip condition and boundary force. Because the projection operators that remove the non-divergence-free and no-slip conditions are applied separately at different sub-time levels, these two constraints cannot be simultaneously satisfied by the velocity field.

In our formulation, there is only one projection step that simultaneously removes both the non-divergence-free and slip component from the velocity field. We also note that our formulation achieves second-order accuracy in time by choosing a suitable approximation for A^{-1}.

2.4.5 Short summary on the comparisons

In the first three approaches, the presence of an immersed object is treated as a corrective term to account for the no-slip condition. The fundamental difference between the aforementioned methods and our formulation is the implicit treatment of both the pressure and boundary force as a single set of Lagrange multipliers in the modified Poisson equation. Once the pressure and the force are determined, the continuity equation and the no-slip condition are satisfied through a projection at the same time level in our formulation. The distributed Lagrange multiplier method is found to be the most similar method but differs in how the projections are applied. Our overall immersed boundary method is viewed as a projection method to allow further generalization and numerical investigation from an algebraic point of view.

2.5 Results

We numerically investigate the temporal and spatial convergence of the current method in one- and two-dimensional model problems; namely the Stokes' problem and flow inside two concentric cylinders, respectively. Also, flow over a circular cylinder is considered to validate the current method in steady-state and transient flow. A moving body example of an impulsively started circular cylinder is considered as well. Finally a three-dimensional example of flow over a sphere is presented.

Since the present method is a combination of the immersed boundary and the fractional step methods, we expect convergence analyses from both methods to carry over to the current formulation. The temporal accuracy of the immersed boundary projection method should follow the analysis from the fractional step algorithm as shown in Eq. (2.24). In all of the problems below, second-order finite volume discretization (except for H and E) is applied. For the problems of flow over a cylinder, a non-uniform grid is employed, making the scheme formally first-order accurate. However, we suppress the first-order spatial error by using a very smooth grid stretching, effectively keeping the overall error to second-order. In the vicinity of the body, the spatial grid is kept uniform with its finest resolution and $\Delta x_{\min} = \Delta y_{\min} \approx \Delta s$. Unless stated otherwise, $N = 3$ is chosen for approximating A^{-1}.

2.5.1 One-dimensional Stokes' problem

We first assess the accuracy of the current method using a one-dimensional Stokes' problem where an infinitely long flat plate is impulsively set into motion with $u_{\text{wall}} = 1$ in an initially quiescent viscous fluid with $\nu = 1$ (Figure 2.2). The initial condition for the simulation is set to the exact solution to the Stokes' problem after a finite time of $t_0 = 0.1$ has elapsed in order to avoid the temporal discontinuity due to the impulsive start from interfering with the convergence study. Simulations are performed in a periodic computational domain in both x- and y-directions with

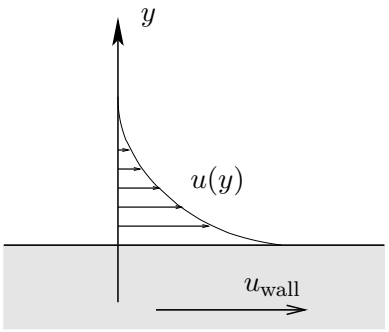

Figure 2.2: Setup for the one-dimensional Stokes' problem.

uniform grid discretization. The top and bottom boundaries are placed far enough to avoid periodicity from interfering with the velocity profile near the translating plate. Spatial and temporal convergence is analyzed in term of the L_∞ and L_2 norms of the horizontal velocity error, $e_j = u(y_j) - u_j$, over the domain $y_j \in [0, 1]$ (in non-dimensional length: $y_j/\sqrt{\nu t_0} \in [0, 3.162]$).

Figure 2.3(a) assesses the temporal L_∞ error for various sizes of non-dimensional time steps, $\nu\Delta t/\Delta y^2$. The error was computed by comparing the solution to a temporally refined reference solution at fixed grid resolution to isolate the spatial discretization error. We calculate the error at $t = 0.11$ with $\Delta y = 10^{-2}$. The three convergence curves on the plot result from the use of different orders of expansion N for B^N (or A^{-1}). Note that the splitting error from Eq. (2.24) is larger in magnitude than the underlying second-order error resulting from the time integration schemes. Hence this splitting error directly influences the temporal accuracy for the range of Δt considered. As discussed in Perot (1993), the splitting error cannot be absorbed by λ because LM^{-1} and Q are not commutative even for a periodic domain.

Next we perform simulations with a very fine time step ($\Delta t = 10^{-6}$) and compare the results to the exact solution at $t = 0.101$ for varying Δy. The velocity profile in the vicinity of the plate is influenced by the regularization of the Dirac delta function. This alters the velocity derivative at the immersed boundary causing the first-order accuracy of the L_∞ norm as shown in Figure

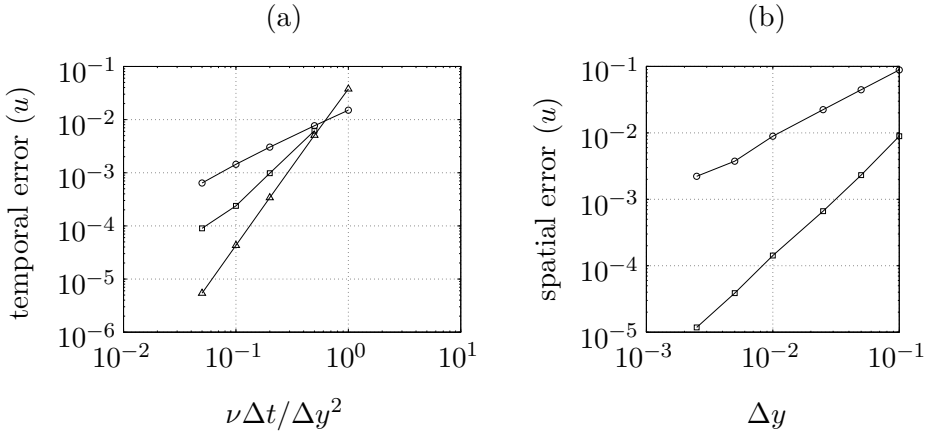

Figure 2.3: Error norms from the one-dimensional Stokes' problem. (a) Temporal L_∞ norm errors with different orders of expansion, N, for A^{-1}; $N = 1$: ◯, $N = 2$: □, and $N = 3$: △. (b) The L_∞: ◯ and L_2: □ spatial velocity error norms.

2.3(b). Fortunately, this smearing effect is dominant only in close proximity of the plate and the underlying second-order convergence is achieved in the L_2 sense.

2.5.2 Flow inside two concentric cylinders

For a two-dimensional test problem, we simulate flow between two concentric hollow cylinders with radii $r_1 = 1/2$ and $r_2 = 1$ as well as the flow inside the smaller cylinder as shown in Figure 2.4. The outer cylinder is held stationary while the inner cylinder is rotated with angular velocity Ω,

$$\Omega = \frac{u_\theta(r_1)}{r_1} = 1 + \tanh\left(\frac{t - 0.2}{0.05}\right), \tag{2.41}$$

moving the initially quiescent fluid at $t = 0$. We take a periodic computational domain of size $[-1.05, 1.05] \times [-1.05, 1.05]$ with uniform spatial resolution and compute the azimuthal velocity error, $e_j = u_\theta(r_j) - u_{\theta,j}$, over $r_j \in [0, r_2]$ (including flow inside the inner cylinder) reporting the L_∞ and L_2 norms.

We study the impact of the splitting error from Eq. (2.24) on the temporal

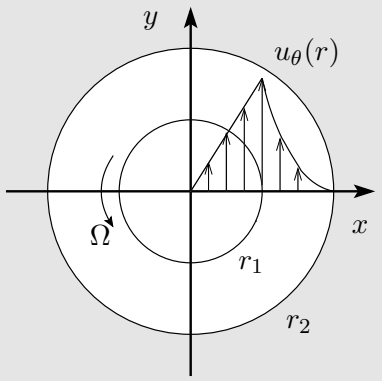

Figure 2.4: Setup for the problem of two concentric cylinders (inner cylinder rotates with angular velocity Ω).

convergence by comparing our results to a reference solution obtained with a very fine time step, $\Delta t = 5 \times 10^{-6}$, and spatial resolution, $\Delta x = \Delta y = 2.1 \times 10^{-2}$. The spatial resolution is kept constant and viscosity is set to $\nu = 1$. Figure 2.5(a) shows that the order of expansion N for A^{-1} again influences the behavior of convergence in a fashion similar to the one-dimensional case. As it can be seen from the $N = 3$ case, the second-order time integration error starts to affect the total error at the smallest shown time step. Based on both the one- and two-dimensional test problems, we recommend the use of third-order expansion N for practical problems. There also is an advantage in choosing $N = 3$ for achieving positive-definiteness of the modified Poisson equation with larger choice of Δt (Perot, 1993).

Next we consider the spatial accuracy of our method at steady-state by comparing our results to the exact solution. The viscosity is reduced to $\nu = 0.01$ in order to use a fine Δx while satisfying $\nu \Delta t / \Delta x^2 \lesssim 1$ to keep B^N positive-definite. Figure 2.5(b) shows the rate of decay for the spatial errors to be 1 and about 1.5 in the L_∞ and the L_2 sense. Although the first-order convergence is expected from the use of discrete delta functions, further investigation is required to explain why second-order accuracy from the underlying spatial discretization cannot be achieved in an L_2 measure.

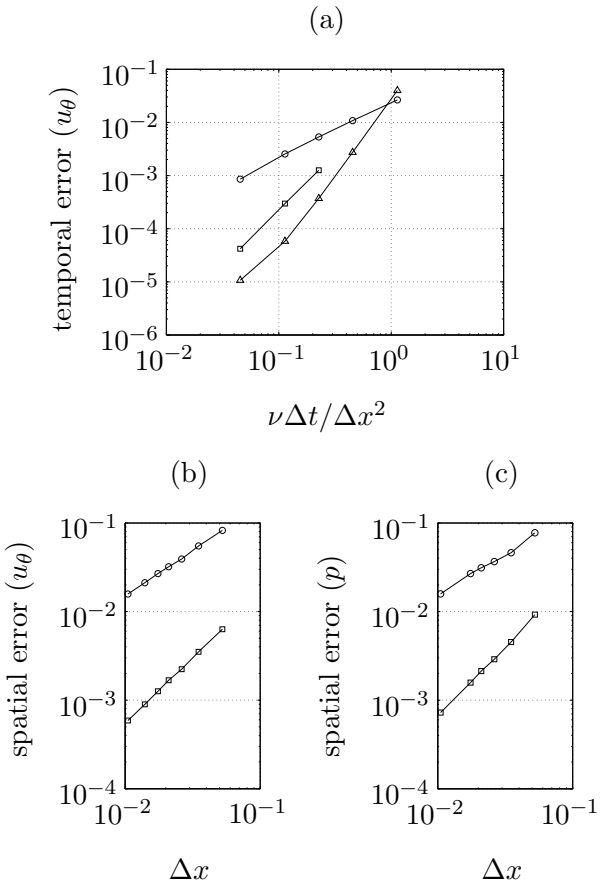

Figure 2.5: Error norms from the problem of two concentric cylinders. (a) Temporal L_∞ norm errors with different orders of expansion, N, for A^{-1}; $N = 1$: ◯, $N = 2$: □, and $N = 3$: △. (b) The L_∞: ◯ and L_2: □ spatial velocity error norms. (c) The L_∞: ◯ and L_2: □ spatial pressure error norms.

The spatial accuracy of the pressure is also studied by comparing the current solution to the exact solution at steady-state. Because the pressure based on the current scheme only solves up to a constant (since we pin the pressure to remove the zero eigenvalue), we compare the solutions by matching the pressure at $r = 0$ for all cases and compute the error norms along the x-axis from 0 to r_1. The infinity and L_2 error norms are plotted against the grid size in Figure 2.5(c) for the same problem considered in assessing the spatial accuracy of velocity. As expected, the spatial accuracy follows the same trend as the velocity shown in Figure 5(b). Due to the presence of the discrete Delta function along the immersed boundary, the pressure distribution is affected limiting the spatial accuracy to orders of one and about 1.5 for the infinity and L_2 norms, respectively.

2.5.3 Flow over a stationary cylinder

We consider flow over a circular cylinder as another test problem because the dimensions of the recirculation zone and the force on the cylinder at various Reynolds numbers are readily available from previous experimental and numerical studies. For the numerical studies, we list results from the immersed boundary method of Lai & Peskin (2000) and the immersed interface method of Linnick & Fasel (2005) among others when the data are available. Our two-dimensional simulations are performed by introducing a cylinder of diameter $d = 1$ in a large computational domain $\mathcal{D}$ with initially uniform flow, $u = u_\infty = 1$. Reynolds numbers of $Re = u_\infty d/\nu = 20,\ 40,$ and 200 are chosen for validating the current method at steady-state and periodic vortex shedding conditions (ν is the kinematic viscosity).

The computational domain is discretized non-uniformly in both x- and y-directions, while the grid spacing is kept uniform with its finest size ($\Delta x_{\min}$) in the vicinity of the cylinder. Table 2.1 summarizes the parameters used in the simulations, where n_x and n_y are the number of cells in the x- and y-directions and n_B is the number of Lagrangian points on the surface of the cylinder with $\Delta s \approx \Delta x_{\min} = \Delta y_{\min}$. Computations are performed with different sizes of $\mathcal{D}$

	$n_x \times n_y$	$\mathcal{D}$	$\Delta x_{\min}$	Δt	$\mathrm{CFL}_{\max}$	n_B
Case A	150×150	$[-30,30]\times[-30,30]$	0.04	0.005	0.22*	78
Case B	300×300	$[-30,30]\times[-30,30]$	0.02	0.005	0.46*	157
Case C	300×300	$[-15,45]\times[-30,30]$	0.0333	0.0125	0.81†	94
Case D	300×300	$[-10,10]\times[-30,30]$	0.0333	0.0125	0.75†	94

Table 2.1: Parameters for spatial and temporal discretization used in the simulations. The maximum CFL numbers are reported from $Re = 40$ (*) and $Re = 200$ (†) cases.

to ensure that the boundary conditions along $\partial\mathcal{D}$ do not influence our solution. Left (inflow) and lateral boundary conditions along $\partial\mathcal{D}$ are set to uniform flow of $(u, v) = (u_\infty, 0)$ and are placed far away from the cylinder. At the outlet, the convective boundary condition ($\partial\mathbf{u}/\partial t + u_\infty \partial\mathbf{u}/\partial x = \mathbf{0}$) is applied to allow vorticity to exit the domain freely. Various spatial and temporal resolutions are chosen to ensure that reliable solutions are obtained. We record the maximum CFL number ($\mathrm{CFL}_{\max} = u_{\max}\Delta t/\Delta x_{\min}$) in Table 2.1 from cases of $Re = 40$ and $Re = 200$. Note that the current method yields a stable solution even with $\mathrm{CFL}_{\max} = 0.81$.

For comparison, we compute the force on the body applied by the flow in terms of the drag and lift coefficients: $C_D \equiv F_x/\frac{1}{2}\rho u_\infty^2 d$ and $C_L \equiv F_y/\frac{1}{2}\rho u_\infty^2 d$, respectively, where $\rho u_\infty^2 d = 1$. The force on the cylinder, $\mathbf{F}$, can be obtained simply by

$$\begin{aligned}\mathbf{F}(t) = \begin{pmatrix} F_x(t) \\ F_y(t) \end{pmatrix} &= -\int_{\mathbf{x}}\int_s \mathbf{f}(\boldsymbol{\xi}(s,t))\delta(\boldsymbol{\xi}(s,t)-\mathbf{x})ds d\mathbf{x} \\ &\approx -\sum_i H_{i,k} f_k \Delta x \Delta y\end{aligned} \tag{2.42}$$

using the regularization operator and the boundary forcing function. Summation over i is implied to take place separately for each direction of the force vector.

First, simulations are performed for $Re = 20$ and 40 to validate the steady-state

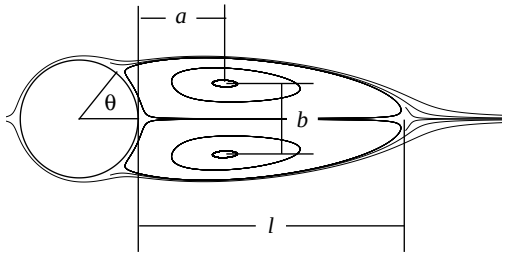

Figure 2.6: Definition of the characteristic dimensions of the wake structure.

characteristics. The resulting wake dimensions and drag coefficients are compared to values reported in the literature. The size of the wake is characterized by l, a, b, and θ (appropriately non-dimensionalized by the diameter) defined in Figure 2.6 following the notation used in Coutanceau & Bouard (1977a). The parameters, l, a, and b represent the length of the recirculation zone, distance from the cylinder to the center of the wake vortex, and the gap between the centers of the wake vortices, respectively. The separation angle is denoted by θ measured from the x-axis. The steady-state vorticity contours and streamlines from Case B are shown in Figure 2.7 for $Re = 20$ and 40. The flow profiles are in close agreement with those reported in the literature. The wake properties from Cases A and B are compared against previous experimental and numerical studies in Table 2.2 and are also found to be in accord.

Next, we consider flow over a cylinder at a Reynolds number of 200 to reproduce periodic vortex shedding. A short time after simulations are initiated from uniform flow, a perturbation in a form of an asymmetric body force is added to trigger the shedding instability. Numerical results replicate the periodic shedding of vortices to form the Kármán vortex street as shown in the vorticity contour of Figure 2.8. The resulting lift and drag coefficients and the Strouhal number, $St \equiv f_s d/u_\infty$, where f_s is the shedding frequency, are compared to previous studies in Table 2.3. Results obtained from Cases B, C, and D are found to be in good agreement with

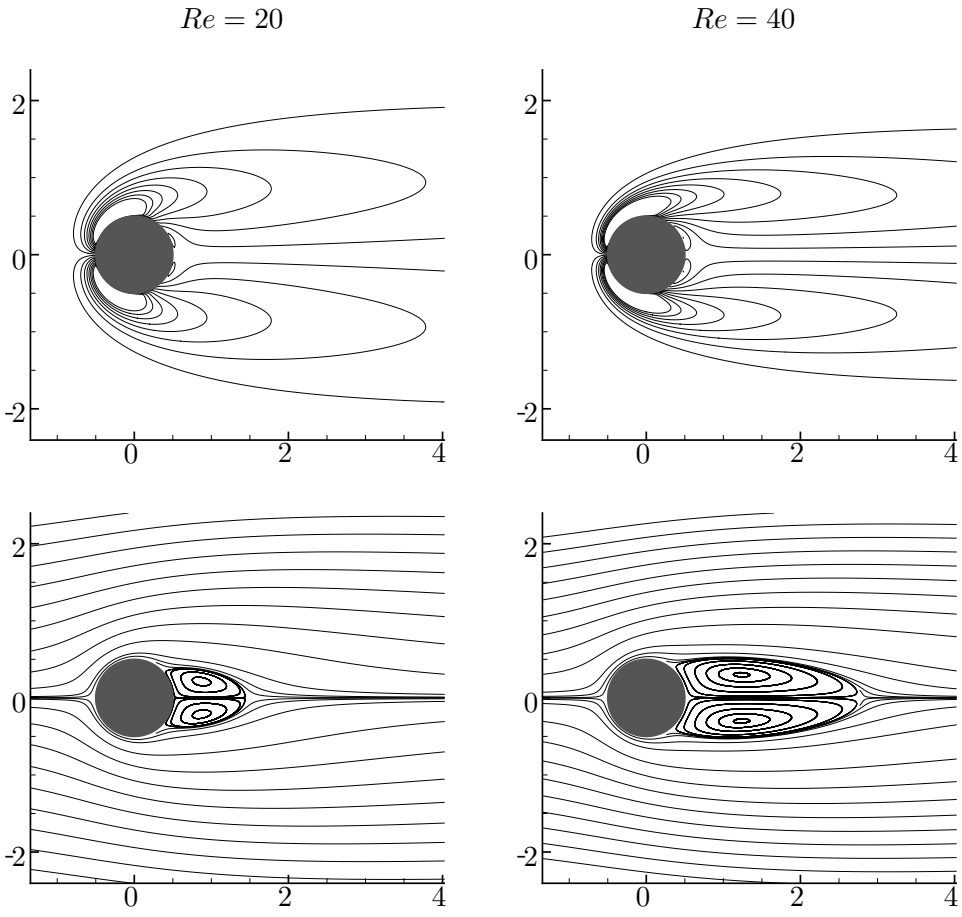

Figure 2.7: Vorticity contours (top) for steady-state flow over a cylinder, where contour levels are set from -3 to 3 in increments of 0.4, and corresponding streamlines (bottom). For left and right plots, $Re = 20$ **and** 40**, respectively.**

		l/d	a/d	b/d	θ	C_D
$Re = 20$	Coutanceau & Bouard (1977a)*	0.93	0.33	0.46	45.0°	-
	Tritton (1959)*	-	-	-	-	2.09
	Dennis & Chang (1970)	0.94	-	-	43.7°	2.05
	Linnick & Fasel (2005)	0.93	0.36	0.43	43.5°	2.06
	Present (Case A)	0.97	0.39	0.43	44.1°	2.07
	Present (Case B)	0.94	0.37	0.43	43.3°	2.06
$Re = 40$	Coutanceau & Bouard (1977a)*	2.13	0.76	0.59	53.8°	-
	Tritton (1959)*	-	-	-	-	1.59
	Dennis & Chang (1970)	2.35	-	-	53.8°	1.52
	Linnick & Fasel (2005)	2.28	0.72	0.60	53.6°	1.54
	Present (Case A)	2.33	0.75	0.60	54.1°	1.55
	Present (Case B)	2.30	0.73	0.60	53.7°	1.54

Table 2.2: Comparison of experimental and numerical studies of steady state wake dimensions and drag coefficient from flow over a cylinder for $Re = 20$ and 40. Experimental studies are listed with (*).

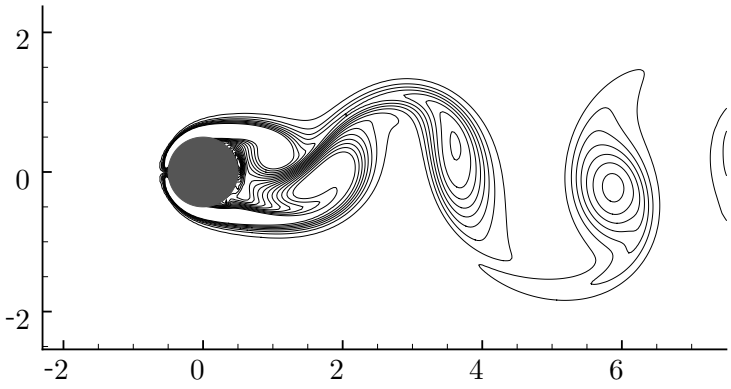

Figure 2.8: Snapshot of the vorticity field with contour levels from -3 to 3 in increments of 0.4 for $Re = 200$.

previous findings.

Results from Case D compared to Cases B and C suggest that the placement of the outflow boundary is not too critical. As a pair of positive and negative vortices convect downstream, their effect on the cylinder become less important since their far-field induced velocity would appear to cancel. On the other hand, we have observed pronounced interference from the lateral boundary conditions when the height of the computational domain is shortened.

2.5.4 Flow around a moving cylinder

As our last test problem, we simulate flow around a circular cylinder in impulsive translation to validate the present method for moving bodies. The simulation is performed by moving the Lagrangian body points at each time step. As these points shift their positions in time, the regularization and interpolation operators are updated according to Eq. (2.28). We initially position the cylinder with unit diameter ($d = 1$) at the origin and impulsively set it into motion to the left with a constant velocity of $u_0 = -1$. Results are presented for Reynolds numbers of $Re = |u_0|d/\nu = 40$ and 200.

		St	C_D	C_L
$Re = 200$	Belov *et al.* (1995)	0.193	1.19±0.042	±0.64
	Liu *et al.* (1998)	0.192	1.31±0.049	±0.69
	Lai & Peskin (2000)	0.190	-	-
	Roshko (1954)*	0.19	-	-
	Linnick & Fasel (2005)	0.197	1.34±0.044	±0.69
	Present (Case B)	0.196	1.35±0.048	±0.68
	Present (Case C)	0.195	1.34±0.047	±0.68
	Present (Case D)	0.197	1.36±0.043	±0.69

Table 2.3: Comparison of Strouhal number and coefficients of drag and lift for flow over cylinder from experimental and numerical studies at $Re = 200$. Experimental studies are listed with (*).

The computational domain $\mathcal{D}$ is taken to be $[-16.5, 13.5] \times [-15, 15]$ with no-slip boundary condition applied along $\partial\mathcal{D}$. Non-uniform grid is used with uniform grid in the near field having a resolution of $\Delta x_{\min} = 0.02$ resulting in a grid size of 425×250. A constant time step of $\Delta t = \Delta x_{\min}/2$ is chosen such that the maximum CFL numbers are limited to 0.98 and 0.81, respectively for $Re = 40$ and 200 during the simulation from a non-dimensional time of $t^* \equiv |u_0|t/d = 0$ to 3.5. Quiescent flow is used for the initial condition.

We present snapshots of the flow field at non-dimensional time of $t^* = 1$, 2.5, and 3.5 in Figure 2.9. Left and right figures illustrate the vorticity field for $Re = 40$ and 200, respectively. The flow fields are in agreement with those in Coutanceau & Bouard (1977*b*) and Koumoutsakos & Leonard (1995) for $Re = 40$. For $Re = 200$, the flow exhibits a generation of stronger vortex pair in the wake of the cylinder. In the two cases, the solutions are resolved well even near the boundary and the difference in the effect of viscous diffusion is nicely captured.

The drag coefficients for the two cases are also computed by Eq. (B.1) during the simulation and are plotted in Figure 2.10. Computational results based on

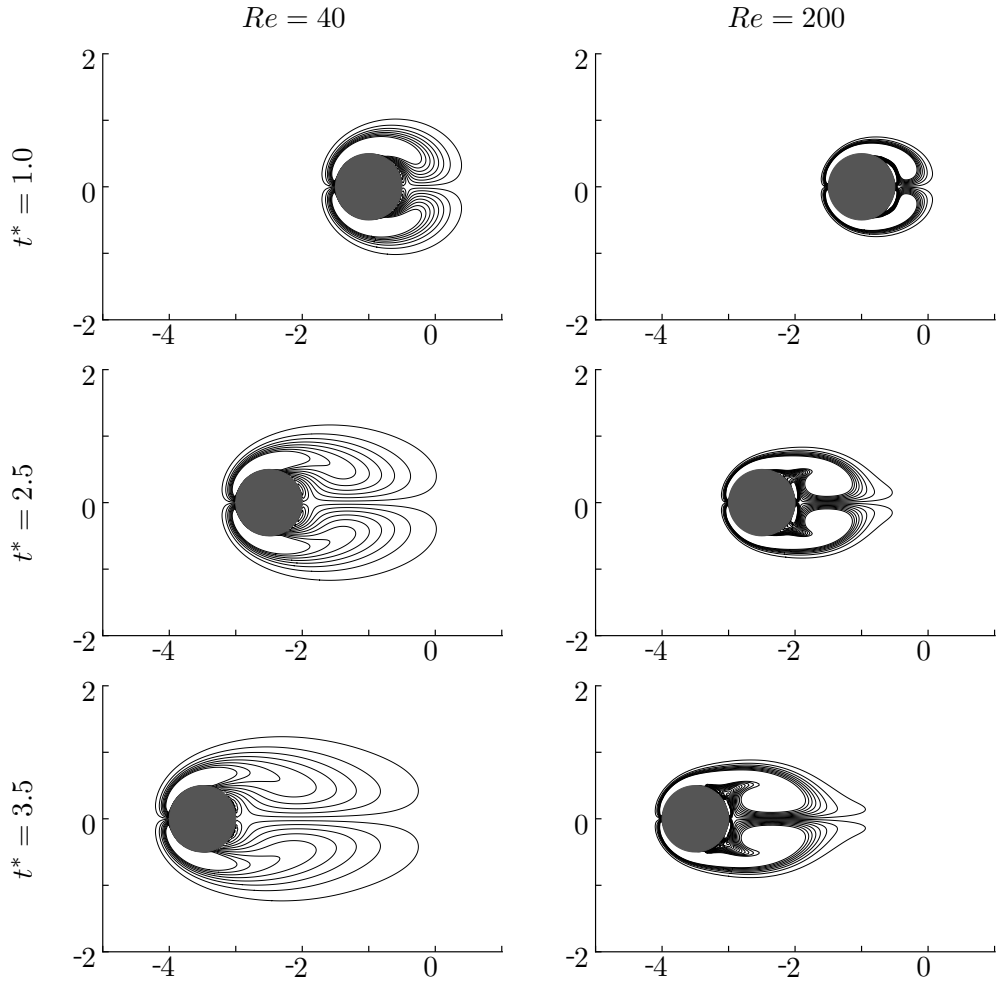

Figure 2.9: Snapshots of the vorticity field around an impulsively moving circular cylinder for $Re = 40$ and 200 at non-dimensional time of $t^* = 1$, 2.5, and 3.5. Contour levels from -3 to 3 in increments of 0.4 are chosen.

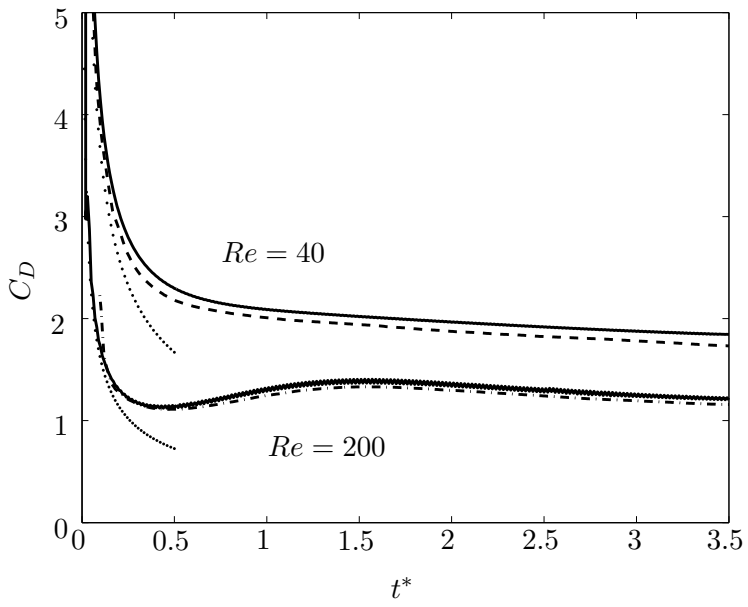

Figure 2.10: History of the drag coefficient of the body for $Re = 40$ and 200 (——) compared with numerical solutions from Koumoutsakos & Leonard (1995) ($Re = 40$, - - - -) and Cottet *et al.* (2000) ($Re = 200$, — - —) and analytical solution by Bar-Lev & Yang (1997) (·····) valid for early time.

vortex methods from Koumoutsakos & Leonard (1995) and Cottet *et al.* (2000) along with the analytical series solution by Bar-Lev & Yang (1997) valid for early time are superposed on the current results. The current scheme reveals the singular behavior of the drag at the start up time ($\mathcal{O}(1/\sqrt{t^*})$) experienced by the cylinder due to the impulsive motion (Bar-Lev & Yang, 1997). Our drag coefficients are about 4 to 5% larger than those from the vortex method. Additional simulations were performed with smaller grid spacings and larger computational domains. However, there were no noticable changes in our solutions to account for the difference.

We also measure the length of the recirculation zone, previously defined as l/d in Figure 2.6, in the frame of reference of the cylinder $(u - u_0, v)$ for validation over time. In Figure 2.11, these lengths are compared with the reported curves from a numerical study of Collins & Dennis (1973) and experimental findings of

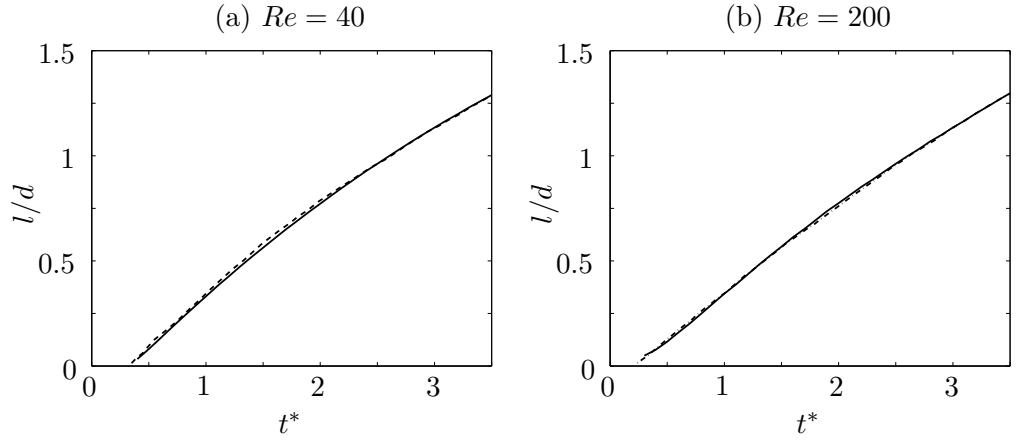

Figure 2.11: Length of the recirculation zone, l/d, in the frame of reference of the moving cylinder as a function time, t^*, for (a) $Re = 40$ and (b) $Re = 200$ compared with previous studies. Present results: ——; experimental measurements of Coutanceau & Bouard (1977*b*) ($Re = 40$, - - - -); and numerical study of Collins & Dennis (1973) ($Re = 200$, —-—).

Coutanceau & Bouard (1977*b*) and are found to be in excellent agreement shown by the overlaps for both Reynolds numbers.

2.5.5 Flow over a sphere

The current method has been extended to three dimensions as well. We present some validation performed for flow around a sphere at steady state.

A sphere of unit diameter is placed at the origin on the computational domain of $[-3, 5] \times [-4, 4] \times [-4, 4]$ discretized with a non-uniform grid. Grid sizes of $90 \times 90 \times 90$ and $125 \times 75 \times 75$ are chosen for computations for $Re = 100$ and 200, respectively. The minimum grid resolution and the time step are set to $\Delta x = \Delta y = 0.04$ and $\Delta t = 0.01$. A good agreement on the wake dimensions and the drag coefficient between the present results and those from Johnson & Patel (1999) are shown in Table 2.4. Notations follow those from the circular cylinder example depicted in Figure 2.6. A steady-state snapshot of the vorticity field around a sphere at $Re = 200$ is shown in Figure 2.12 and are found to be in accord with

		l/d	a/d	b/d	θ	C_D
$Re = 100$	Present	0.91	0.28	0.59	50.4°	1.14
	Johnson & Patel (1999)	0.88	0.25	0.60	53°	1.10
$Re = 200$	Present	1.38	0.37	0.69	61.2°	0.82
	Johnson & Patel (1999)	1.46	0.39	0.74	63°	0.80

Table 2.4: Steady-state wake dimensions and drag coefficient from flow over a sphere at $Re = 100$ and 200.

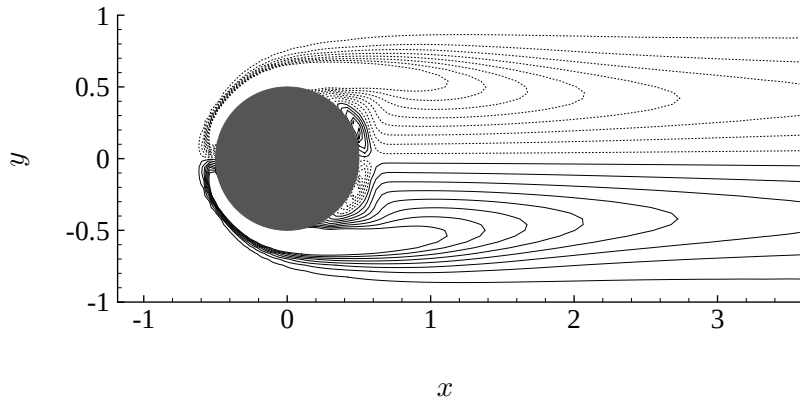

Figure 2.12: Steady-state vorticity field around a sphere at $Re = 200$. Contour' levels are set from -3 to 3 in increments of 0.4. Negative contour levels are shown with dashed lines.

Johnson & Patel (1999).

Three-dimensional validation of unsteady flows are offered later in Section 3.2.2 for flows over an impulsively translating low-aspect-ratio flat-plate wing at $Re = 100$.

2.6 Summary

We presented a new formulation of the immersed boundary method that is algebraically identical to the traditional fractional step algorithm. The current

method introduces regularization and interpolation operators and regards both the pressure and boundary force as Lagrange multipliers required to satisfy the kinematic constraints of divergence-free and no-slip. The no-slip condition along the immersed surface is satisfied by a projection in a manner analogous to the removal of non-divergence-free component of the velocity field in the classical projection methods. The overall method is constructed to preserve symmetry and positive-definiteness to efficiently solve for the flow field. The boundary force is determined implicitly without any constitutive relations for the rigid body formulation. This in turn allowed us to use a CFL number as high as 1 in our simulations. Deforming bodies whose motion is known *a priori* can also be treated. The current scheme is numerically found to be third-order temporally accurate for most practical sizes of time steps and second-order accurate in time for small time steps. The spatial accuracy is observed to be better than first-order in the L_2 norm for one- and two-dimensional problems. Results from simulations of two-dimensional flows over both stationary and moving cylinders as well as three-dimensional flows over spheres showed excellent agreement with previous experimental and numerical studies. While it was not discussed in this chapter, a technique to speed up this immersed boundary method by an order of magnitude is offered in Appendix B.

Chapter 3

Separated Flows around Low-Aspect-Ratio Wings

3.1 Introduction

The Reynolds number at which micro-air-vehicles operate have reached $\mathcal{O}(10^4)$ and will continue to decrease in the coming years (Pines & Bohorquez, 2006). Due to the operational and weight requirements, these aircraft have unique designs with low-aspect-ratio wings, when compared to those of conventional aircraft. Moreover, these vehicles fly at low speed and often high angles of attack while experiencing large perturbations such as wind gusts. Yet there are only few studies of low-Reynolds-number aerodynamics around low-aspect-ratio wings under translation.

As micro-air-vehicles become smaller in size, they share some characteristics with flying and swimming animals such as birds, insects, and fishes. These animals have low-aspect-ratio wings or fins that are operating at Reynolds numbers of order 10^2 to 10^5, often at post-stall angles of attack. However, separated flows have been used to the advantage of the animals for enhanced performance. For example, it has been observed that hovering insects can achieve added lift from the unsteady separated flows around the flapping wings. The leading-edge vortices are found to be stably attached throughout each stroke and provide additional

spanwise circulation resulting in enhanced lift. Such forces applied by the unsteady vortex formation in two-dimensional flows were investigated both experimentally by Dickinson & Götz (1993) and numerically by Wang (2000*a*,*b*, 2004) and Bos *et al.* (2008). Furthermore, the full three-dimensional studies drawing attention to spanwise flows and tip effects around the flapping wings were undertaken experimentally by Ellington *et al.* (1996), Birch & Dickinson (2001), Usherwood & Ellington (2002), Birch *et al.* (2004), and Poelma *et al.* (2006). Analogous numerical studies were performed by Liu *et al.* (1998) and Sun (2005).

Similar investigations have been carried out to analyze the efficient locomotion of swimming animals. In particular, von Ellenrieder *et al.* (2003), Buchholz & Smits (2006), and Parker *et al.* (2007) have visualized the wake vortices behind flapping low-aspect-ratio hydrofoils to understand the qualitative dynamics. Numerical simulations of the three-dimensional flows over flapping foils were also performed by Blondeaux *et al.* (2005) and Dong *et al.* (2006) at Reynolds numbers similar to the present study. Moreover, Drucker & Lauder (1999) have experimentally visualized the flows around pectoral fins and Zhu *et al.* (2002) have performed simulations around an entire fish to identify the wake structures.

For purely translating low-aspect-ratio wings, Torres & Mueller (2004) have experimentally measured the aerodynamic characteristics of low-aspect-ratio wings at Reynolds numbers around 10^5. Aerodynamic performance (lift, drag, pitching moment, etc) of various planforms was considered over angles of attack (α) of 0° to 40° and aspect ratios (AR) of 0.5 to 2 and was observed to be quite different from that of low-aspect-ratio wings in high-Reynolds-number flows. They concluded that the most important parameter that influences the aerodynamic characteristics is the aspect ratio. Transient studies have also been conducted by Freymuth *et al.* (1987) by using smoke to visualize the start-up flows around low-aspect-ratio airfoils. A qualitative insight into the three-dimensional formation of wake vortices was presented. The experiments by Ringuette *et al.* (2007) extensively studied the wake vortices behind low-aspect-ratio plates but only at $\alpha = 90^\circ$.

On the numerical side, two-dimensional simulations around translating wings

were performed by Hamdani & Sun (2000). Also, studies by Mittal & Tezduyar (1995) and Cosyn & Vierendeels (2006) considered the three-dimensional flows around translating low-aspect-ratio planforms but focused mostly on those at low angles of attack. For wings at post-stall angles of attack, unsteady separated flows and vortex dynamics behind low-aspect-ratio wings in pure translation are still not well-documented.

To extend the previous studies, we use numerical simulations to examine the aerodynamics of impulsively started low-aspect-ratio flat-plate wings under pure translation at Reynolds numbers of 300 and 500. These Reynolds numbers are high enough to induce separation and unsteadiness in the wake but low enough for the three-dimensional flow field to remain laminar. The regime also includes, for a range of angles of attack, the critical Reynolds numbers at which the flow first becomes unstable to small disturbances. In the following section, we present the numerical method and its validation. In Section 3.3, results from separated flows around the airfoils are presented. We call attention to the transient nature of the flow field and its influence on the aerodynamic forces. The stability of the wake is also investigated at large time. Dynamics of the wake vortices and the corresponding lift and drag are considered over a range of angles of attack and various planform geometries.

3.2 Simulation methodology

3.2.1 Simulation setup

Three-dimensional incompressible flow over a low-aspect-ratio flat-plate wing is simulated with the immersed boundary projection method described in Chapter 2 and Taira & Colonius (2007). The computational domain is set to a typical size of $[-4, 6.1] \times [-5, 5] \times [-5, 5]$ in the streamwise (x), vertical (y), and spanwise (z) directions with a grid size ranging from $125 \times 55 \times 80$ to $150 \times 66 \times 156$ with the smallest resolution of $\Delta x = 0.03$. In all cases, the spatial variables are non-

dimensionalized by the chord (c) of the plate. Grid stretching is applied in all directions with finer resolution near the plate to capture the wake structure as illustrated in Figure 3.1. Extensive studies have been performed in two and three dimensions to ensure that the present choice of grid resolution and domain size does not influence the flow field in a significant manner (previously reported in Taira *et al.* (2007)).

Boundary conditions along all sides of the computational boundary, $\partial\mathcal{D}$, are set to uniform flow $(U_\infty, 0, 0)$ except for the outlet boundary where a convective boundary condition ($\frac{\partial \mathbf{u}}{\partial t} + U_\infty \frac{\partial \mathbf{u}}{\partial x} = 0$) is specified. Inside the computational domain, a flat plate is positioned with its center at the origin. This flat plate is instantaneously materialized at $t = 0^+$ in an initially uniform flow to model an impulsively started translating plate. Computations are advanced in time with a time step such that the Courant number based on the free-stream velocity obeys $U_\infty \Delta t/\Delta x \leq 0.5$. Both the initial transient and the large-time behavior of the flow are considered. The time variable is reported in terms of the nondimensional convective time unit (i.e. , $U_\infty t/c$).

In Chapters 3 and 4, the Reynolds number is defined as $Re \equiv U_\infty c/\nu$, where ν denotes the kinematic viscosity of the fluid. Forces on the flat plate (F_x, F_y, F_z) are described in terms of the non-dimensionalized lift, drag, and side forces defined by $C_L = F_y/(\frac{1}{2}\rho U_\infty^2 A)$, $C_D = F_x/(\frac{1}{2}\rho U_\infty^2 A)$, and $C_S = F_z/(\frac{1}{2}\rho U_\infty^2 A)$, respectively, where ρ is the density of the fluid and A is the area of the flat plate. In the case of two-dimensional flows, the force per unit span is normalized by the chord.

3.2.2 Validation

We compare results from the three-dimensional simulations and measurements from an oil tow-tank experiment[1] of flows over a rectangular plate of $AR = 2$ at $Re = 100$. The experiment is performed in a tank (2.4m $\times$ 1.2m $\times$ 1m) filled with mineral oil, in which a rectangular flat plate is translated. The flat plate

[1]The experiment was conducted by Dr. William B. Dickson (Bioengineering, California Institute of Technology). His generosity in sharing the data is gratefully acknowledged.

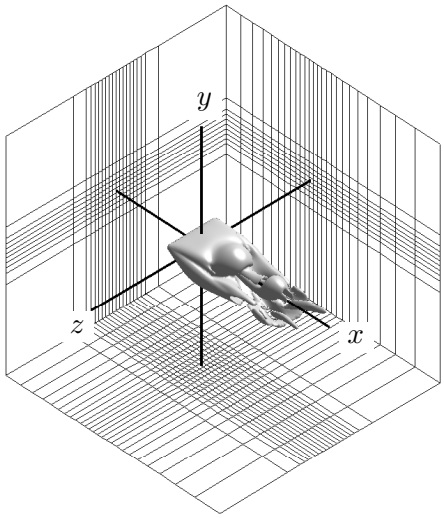

Figure 3.1: A typical computational domain showing the top-port side of the wake around a rectangular flat plate of $AR = 2$. The spatial discretization of this computational domain is shown for every 5 cells for the x- and y-directions and every 4 cells for the z-direction.

is of dimension 82mm × 164mm × 3mm and is rigidly mounted to a six-axis force sensor at one wing tip to limit lift due to backlash in the gearbox. This setup is attached to a translation sled equipped with a servo motor providing control of the translational velocity (Dickson & Dickinson, 2004). A constant translation velocity is maintained by the plate after a swift acceleration from rest. During the experiments, the flow field is captured with stereo digital particle image velocimetry (DPIV).

Shortly after the initial transient, the flow achieves a steady state at this low Reynolds number. Due to the spatial setup of the oil tank, the maximum travel distance of the plate is limited to 13 chord lengths to avoid the interference of wall effects. In Figure 3.2, snapshots of the spanwise vorticity (ω_z) contour are shown for the simulation and experiment for the plate at $\alpha = 30°$. Following the impulsive start, the leading-edge and tailing-edge vortices are formed ($t = 1.5$). The three-dimensional structure of the forming leading-edge vortex is illustrated with the isosurface $\omega_z = -4$ in Figure 3.3. Later in time, the trailing-edge vortex (starting

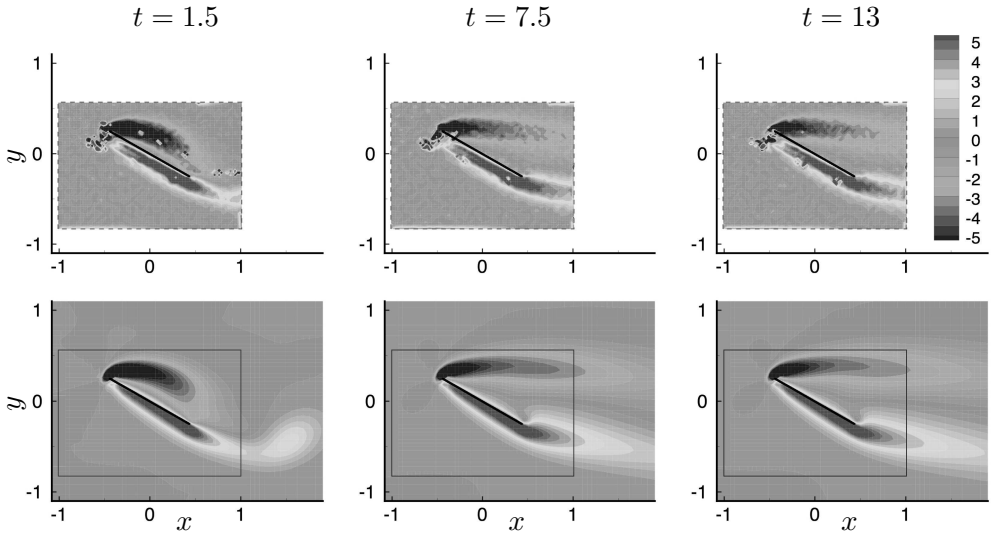

Figure 3.2: Snapshots of spanwise vorticity field at mid-span around a plate of $AR = 2$ at $\alpha = 30°$ from the experiment (top) and the simulation (bottom). Free stream is directed from left to right and the position of the plate is illustrated with the black solid line (for the experiment, the position is approximate due to the deflection of the plate). The boxed regions in the simulated results represent the fields of view for the DPIV measurements.

vortex) detaches and the leading-edge vortex lifts upward. At this low Reynolds number, the vorticity profile is very diffusive and the vorticity generated at the leading and tailing edges forms a smeared steady distribution at later times. This flow profile is reached by $t = 7.5$ and is indistinguishable from the last snapshot taken from the experiment at $t = 13$. As it can be seen from Figures 3.2 and 3.3, the simulated flow field is in great agreement with the DPIV measurements. Three-dimensional flow past a plate of $AR = 2$ is found to reach a stable steady state due to the stabilizing effects from the tip vortices and viscosity. We note in passing that the analogous two-dimensional flow at $Re = 100$ exhibits periodic shedding of the leading- and trailing-edge vortices.

For the purpose of validating our simulation, we also compare lift and drag forces at $t = 13$ from both the simulation and experimental measurements. It is found from the simulation that, past $t = 13$, forces decay to the steady value in

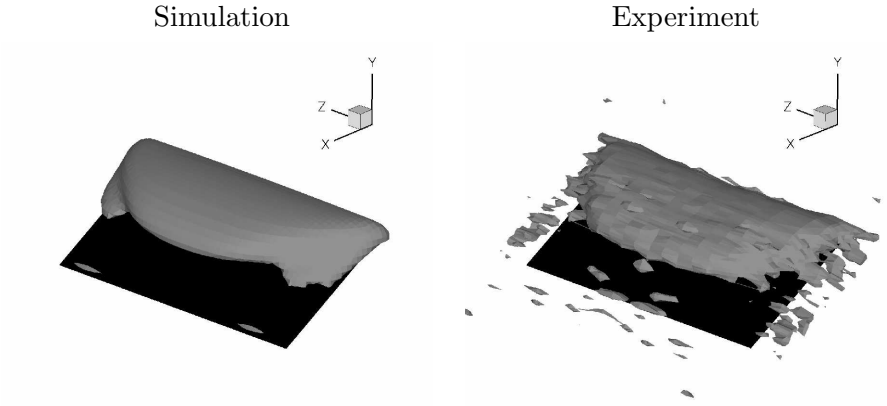

Figure 3.3: Isosurface for the spanwise vorticity of $\omega_z = -4$ at $t = 1.5$ illustrating the LEV formation viewing from the rear of the plate ($AR = 2$, $Re = 100$).

a very slow manner. Figure 3.4 compares measured lift and drag coefficients with the simulations based on two different grid sizes for $\alpha \in [0°, 90°]$. Lift coefficients from experiments and simulations are in agreement over the full range of α. Drag coefficients show slight discrepancy between the experiment and the numerical computation, due to the thickness of the flat plate. In experiments, the thickness of the plate is $0.037c$, while in the simulations, we attempt to model an infinitely thin plate with regularized body forces dependent on the grid spacing. However, the flow features are insensitive to our selection of grid spacing at the current Reynolds numbers of interest. We also note that the measured forces on the plate may be influenced by the presence of the sting on one of the wing tips.

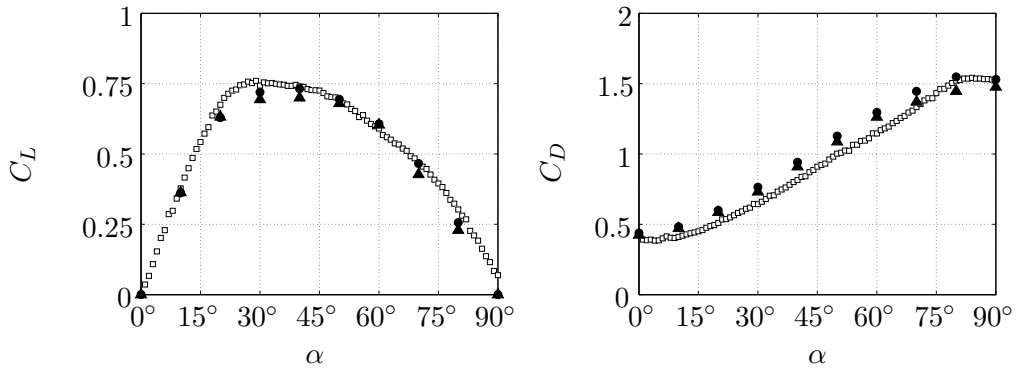

Figure 3.4: Lift and drag coefficients for a rectangular plate of $AR = 2$ at $Re = 100$. Data from the oil tow tank experiments are shown with □ and results from numerical simulations are presented with • and ▲ for grid sizes of $125 \times 55 \times 80$ and $150 \times 66 \times 96$, respectively.

3.3 Separated flows around low-aspect-ratio flat plates

3.3.1 Dynamics of wake vortices behind rectangular planforms

We first consider the formation and evolution of wake vortices behind rectangular flat plates of $AR = 1$, 2, and 4 at $Re = 300$. Snapshots in Figure 3.5 show the corresponding flow fields at a high angle of attack of $\alpha = 30°$. The wake vortices are visualized with two different iso-surfaces. First, constant vorticity surface ($\|\boldsymbol{\omega}\|_2 = 3$) is shown in light gray to capture the vortex sheets. Second, the second invariant of the velocity gradient tensor ($\nabla \mathbf{u}$), known as the Q-criterion or Q-value, is used to highlight the vortex cores depicted by the dark gray surfaces ($Q = 3$). Positive Q-values give prominence to regions of high swirl in comparison to shear to represent coherent vortices (Hunt *et al.*, 1988). In incompressible flows, the Q-value is provided by $Q \equiv \frac{1}{2}(\|\boldsymbol{\Omega}\|^2 - \|\mathbf{S}\|^2)$, where $\boldsymbol{\Omega} \equiv \frac{1}{2}[\nabla \mathbf{u} - (\nabla \mathbf{u})^T]$ and $\mathbf{S} \equiv \frac{1}{2}[\nabla \mathbf{u} + (\nabla \mathbf{u})^T]$.

Plates are impulsively translated in an initially quiescent flow, generating strong vortex sheets on the top and bottom surface of the plates at $t = 0^+$. Thereafter, the flow separates from the leading edge and tips, which act as strong sources of vorticity. Vorticity is then fed into the flow as vortex sheets that roll up into the leading-edge, trailing-edge, and tip vortices. As the leading-edge vortex forms and the trailing-edge vortex advects downstream, the plate experiences a large increase in lift. This enhanced lift is an added effect on top of the lift achieved at large time (Dickinson & Götz, 1993). Note that the initial topology of the wake structures are the same for all finite AR considered here and the phenomena resemble dynamic stall observed behind high-aspect-ratio wings undergoing a swift pitch-up (Carr, 1988).

As features from the initial transient lose their effect on the plate through advection and diffusion, the wake behind the plate becomes strongly dependent on the aspect ratio. At $\alpha = 30°$, the $AR = 1$ case slowly reaches a steady state with a pair of strong counter-rotating tip vortices that cover the entire span of the plate. The vortex sheet created from the leading edge is kept attached to the plate due to the downward induced velocity from the tip vortices.

For a plate of $AR = 2$, the vortex sheet emanating from the leading edge rolls into a leading-edge vortex that accumulates spanwise vorticity over time. The tip vortices are not strong enough to keep the leading-edge vortex attached. Around $t \approx 8$, two consecutive leading-edge vortices start to pinch off from the plate. As the detachment takes place, the disconnected vortices start to interact with the tip vortices. This interaction results in the loss of the columnar structures initially maintained by the tip vortices and reduces the downward induced velocity onto the vortical structure residing above the top surface of the plate. Hence, once the initial leading-edge vortices are separated, consecutive formation of the leading-edge vortices (hairpin vortices) by the roll-up of the leading-edge vortex sheet occurs farther and at a higher position. Additionally, weakening of the tip vortices allows the trailing-edge vortex sheet to morph into hairpin vortices that shed. The nonlinear interaction of the wake vortices results in an unsteady aperiodic flow at

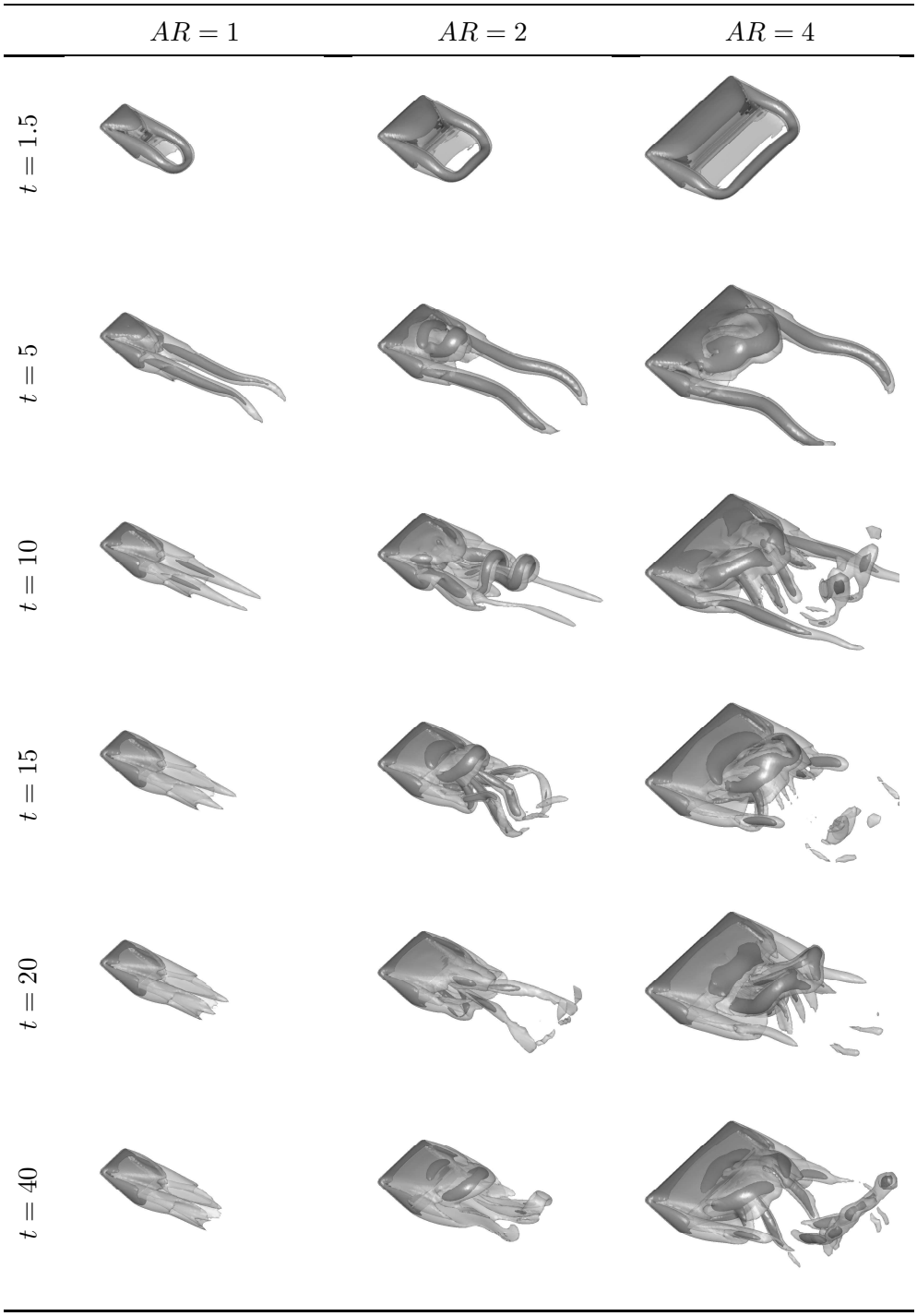

Figure 3.5: Top-port views of the wake vortices behind rectangular plates of $AR = 1$, 2, and 4 at $\alpha = 30^\circ$ and $Re = 300$. Shown are the iso-surface of $\|\boldsymbol{\omega}\|_2 = 3$ in light gray with vortex cores highlighted by the iso-surface of $Q = 3$ in dark gray.

large time. While it is not apparant from Figure 3.5, there is slight asymmetry in the spanwise direction that contributes to the aperiodic nature of the shedding. Discussion on this asymmetry is offered later in Section 3.3.5.

For the largest finite aspect-ratio plate considered ($AR = 4$), the weaker influence of the tip vortices across the span results in more strongly pronounced periodic shedding of the leading- and trailing-edge vortices. The shedding frequency (non-dimensionalized as the Strouhal number with the frontal projection of the chord) for $AR = 4$ is found to be $St \equiv fc\sin\alpha/U_\infty = 0.12$. In contrast, the two-dimensional shedding frequency for the same Reynolds number and angle of attack is $St = 0.16$.

Around $AR = 3$, the vortical structures from the leading and trailing edges start appearing to separate into two cells across the span. The cellular pattern referred to as stall cells becomes more apparent for $AR = 4$ where a pair of hairpin vortices are generated from the leading edge and another pair is created from the trailing edge resulting in a release of four hairpin vortices per shedding cycle. Such flow features were also reported on the top surface of the airfoils with oil film and tuft visualizations by Winkelmann & Barlow (1980) and Yon & Katz (1998), respectively, at $Re = \mathcal{O}(10^5)$. While we do not notice features of the stall cells directly on the top surface, we find qualitative agreement for the number of cells observed some short distance into the wake.

Despite the interactions between the leading-edge and tip vortices, these vortices remain distinct without merging for all three-dimensional cases. Due to the existence of the right-angled corners on the rectangular plates, the vortex sheets thin out near these regions and the sheets roll up into individual core structures of leading-edge and tip vortices. The separation of the vortical structures indicates a lack of convective vorticity flux in the spanwise direction (i.e., from the mid-span to the tips). Such transport has been suggested to stabilize the leading-edge vortex for flapping wings (Birch & Dickinson, 2001; Birch *et al.*, 2004). For the translating rectangular wings, there is no mechanism to relieve the vorticity being fed into the leading-edge vortex other than diffusion and shedding of the vortical structures.

The effects of removing sharp corners by using different planform geometries are discussed later in Section 3.3.6.

3.3.2 Flows at higher Reynolds number

Flows behind rectangular plates at $Re = 500$ are also simulated and are found to be similar to the ones presented here for $Re = 300$. With the larger Reynolds number, the wake vortices are less diffused but the topology of the vortical structure are qualitatively similar, which was also noted by Dong *et al.* (2006) for flows around flapping foils for $Re = 100$ to 1000.

The geometries of the wake vortices in low-Reynolds-number flow ($Re = \mathcal{O}(100)$) at early times following the impulsive start also resemble those in flows of much higher Reynolds numbers, due to the fact that the viscous time scale ($t_{\text{vis}} \sim c^2/\nu$) is much larger than the time scale associated with convection or acceleration ($t_{\text{conv}} \sim c/U_\infty$ or $t_{\text{acc}} \sim c^{1/2}/a^{1/2}$, respectively).

Impulsive flow over a plate of $AR = 2$ at $Re = 500$ and $\alpha = 40°$ is simulated and is compared to the smoke visualizations of vortices under a constant acceleration from quiescent flow in a starting wind tunnel (Freymuth *et al.*, 1987) as shown in Figure 3.6. Reynolds number for this experiment is defined with the constant acceleration, the chord, and the kinematic viscosity as $Re_a = a^{1/2}c^{3/2}/\nu = 5200$ following the non-dimensionalization by Freymuth *et al*.

As acceleration of immersed boundaries contributes to the generation of vorticity[2] (Hornung, 1989), the formation of vortices behind a plate under impulsive translation and constant acceleration cannot be directly compared. However, the formation of start-up vortices should be qualitatively similar at early times before viscous effect significantly influences the flow and the induced velocity of each wake vortex becomes large. The formation of the start-up vortices is illustrated by the snapshots in Figure 3.6 with smoke visualization and the

[2]The source of vorticity from a rigid non-rotating planar surface is $\mathbf{J}_{\text{surf}} \cdot \hat{\mathbf{n}} = -\hat{\mathbf{n}} \times \left[\frac{d\mathbf{u}_{\text{surf}}}{dt} + (\nabla p)_{\text{surf}}\right]$, where $\hat{\mathbf{n}}$ is the unit normal vector and the tensor $\mathbf{J}$ is related to the vorticity field through $\frac{\partial \boldsymbol{\omega}}{\partial t} + \mathbf{u} \cdot \nabla \boldsymbol{\omega} = -\nabla \cdot \mathbf{J}$.

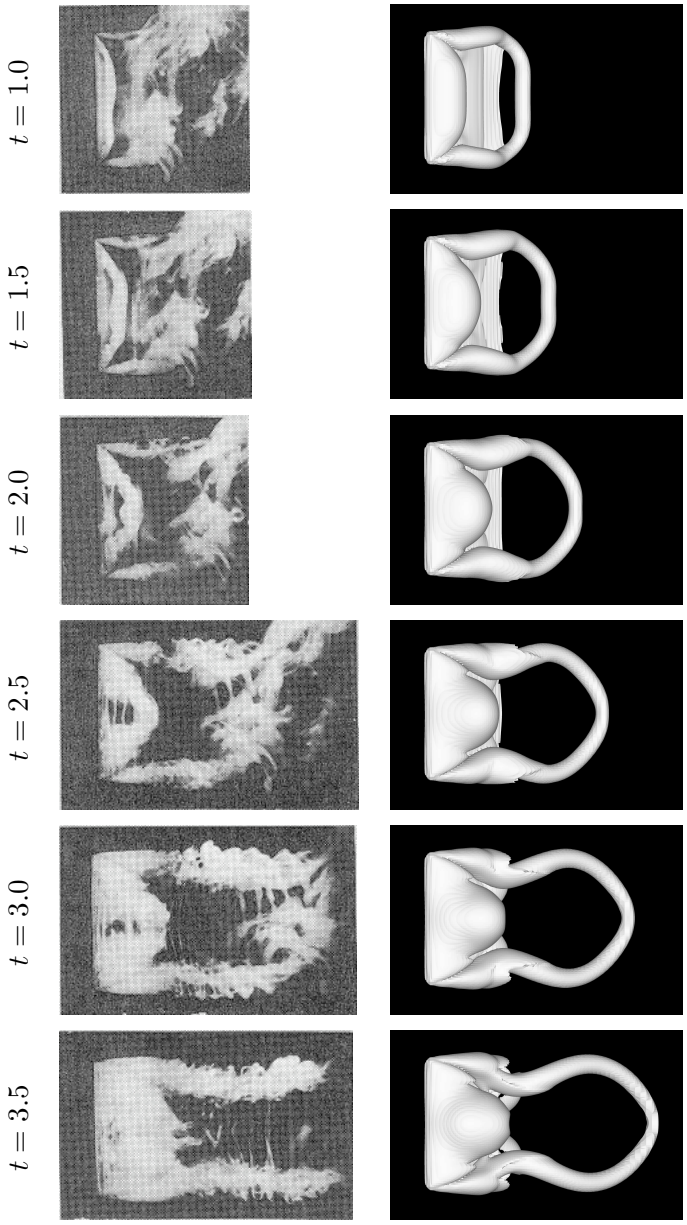

Figure 3.6: Top views of the wake vortices behind a rectangular wing of $AR = 2$ at $\alpha = 40^\circ$ from smoke visualizations (left) at $\boldsymbol{Re}_a = 5200$ and present results (right) at $\boldsymbol{Re} = 500$ with iso-contour of $\|\boldsymbol{\omega}\|_2 = 5$. Smoke visualizations are from Freymuth *et al.* (1987); reprinted by permission of the American Institute of Aeronautics and Astronautics.

vorticity norm iso-surface.

For the case of constant acceleration, a characteristic velocity of $u_a = a^{1/2}c^{1/2}$ is used to non-dimensionalize the temporal variable. Accordingly, the flow fields are compared at the non-dimensional times of tU_∞/c and $ta^{1/2}/c^{1/2}$ for the simulations and the experiments, respectively. In Figure 3.6, it can be seen that the formation and evolution of leading-edge and tip vortices are in good agreement between the experiment and the numerical solution, despite the difference in the Reynolds number and the velocity profile to which the plate is subjected. The exact location of the trailing-edge vortex from the smoke visualization is difficult to pinpoint but is found to be in accord by its faint trail of smoke at earlier times. The simulation is able to capture even the thin layer of vortex sheet emanating from the leading edge, which would correspond to the region directly downstream of the leading edge that is not visualized by the smoke. Dominant flow features at early times in high-Reynolds-number flows are captured even with the present low-Reynolds-number flow simulations.

3.3.3 Force exerted on the plate

Unsteady forces on accelerating airfoils at low Reynolds numbers have been considered for two-dimensional flows by Dickinson & Götz (1993) and Pullin & Wang (2004). In this section, we consider the forces exerted upon the plate with the three-dimensional wake vortices both immediately after the impulsive start and also at large times.

Representative lift and drag on rectangular plates from the present simulations are presented in Figure 3.7 for $Re = 300$. Here results for angles of attack of $\alpha \in [0^\circ, 60^\circ]$ and aspect ratios of 2 and 4 as well as the two-dimensional cases are shown for $t \in [0, 70]$. At $t = 0^+$, the impulsive start imposes infinite acceleration on the airfoil in the streamwise direction and results in infinite initial drag (not shown for graphical clarity). Subsequently, lift starts to increase as accumulation of spanwise vorticity instigates the formation of the leading-edge vortex. This increase in lift continues to about $t \approx 1.7$ to reach its maximum. The time to

reach maximum lift is observed to be fairly constant in the case of finite aspect ratio wings over most of the angles of attack considered here at low Reynolds numbers. The universality of this number is discussed in detail later.

After the initial start-up, lift is reduced by as much as half of the maximum value at large time, as shown in Figure 3.7. Depending on whether the wake at large time becomes steady or unsteady, the corresponding force coefficients reach constant or fluctuating values.

It should be noted that the three-dimensional flows of consideration are vastly different from the two-dimensional case, where one observes periodic shedding of the leading- and trailing-edge vortices creating the von Kármán vortex street. Due to the absence of the tip vortices, the two-dimensional flow exerts a strikingly larger fluctuation in force per unit span as shown in Figure 3.7.

The effect of aspect ratio on the forces is considered by comparing the maximum lift during the transient and the time-averaged forces at large time. These values for wings of $AR = 1$, 2, and 4, as well as the two-dimensional case, are presented in Figure 3.8 accompanied by their inviscid limits. Stronger influence of downwash from the tip vortices results in reduced lift for lower aspect-ratio plates. For the limiting case of two-dimensional flow, the maximum lift is much higher due to the absence of tip effects (Figure 3.8(a)). It is interesting to note that the maximum lift achieved soon after the impulsive start is comparable or higher than the three-dimensional inviscid limit for low-aspect-ratio straight wings in incompressible flow (Helmbold, 1942):

$$C_L = \frac{2\pi\alpha}{\sqrt{1 + (2/AR)^2} + 2/AR}. \tag{3.1}$$

This limit is derived from the lifting surface theory for elliptic wings and is shown to be in remarkable agreement with wings of $AR < 4$. Lift for rectangular wings of $0.5 \leq AR \leq 6$ is accurately predicted with this equation as shown in Anderson (1999).

We observe agreement between the time-averaged low-Reynolds-number lift at large time and the above inviscid model at low angles of attack ($\alpha \lesssim 10^\circ$), where

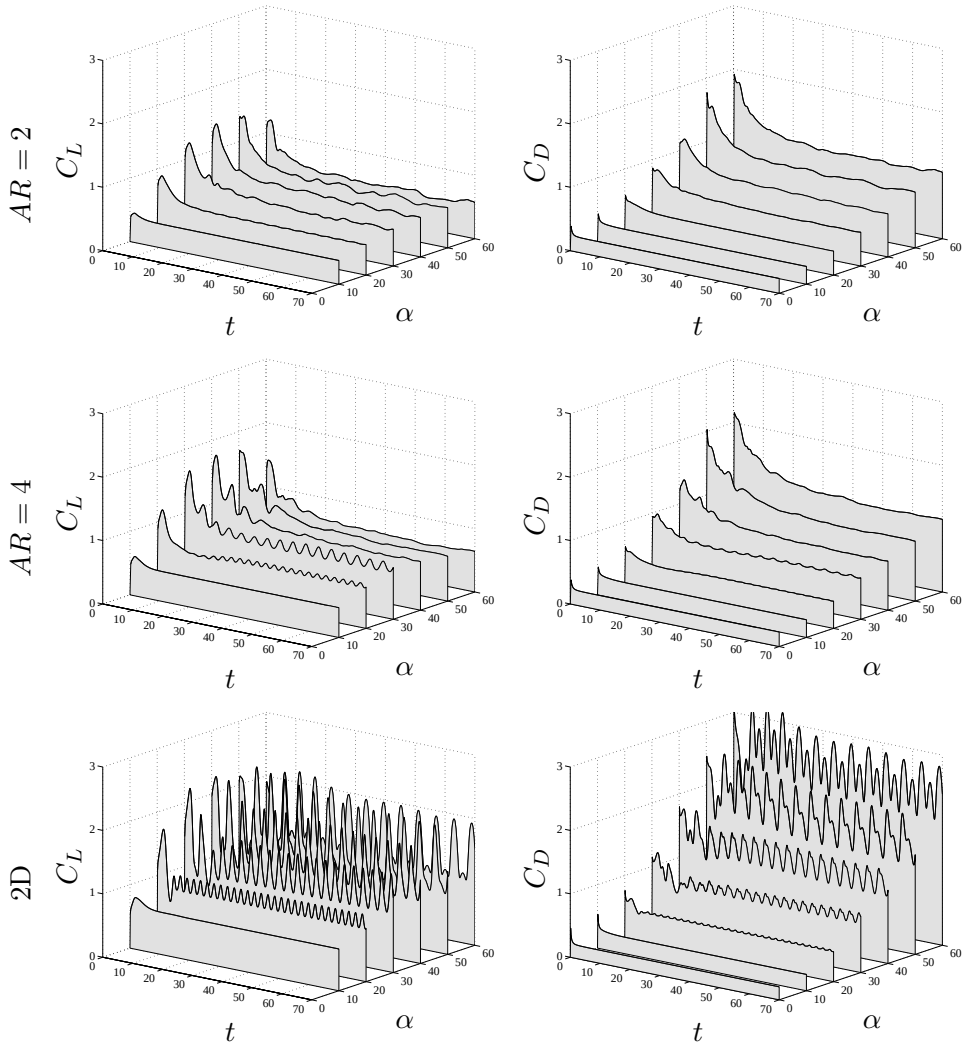

Figure 3.7: Force history on rectangular flat plates of different AR for a range of angles of attack at $Re = 300$. Lift and drag coefficients are shown on the left and right, respectively.

the flows are still attached (Figure 3.8(b)). The small difference can be attributed to viscous effects. However, once the flow separates from the plate at higher α, the inviscid approximation is no longer able to model the lift behavior. The high value of $\alpha_{C_L\,\max}$ (angle of maximum lift) was also reported for low-aspect-ratio wings at $Re \cong 10^5$ by Torres & Mueller (2004). We mention that the difference between the maximum (max C_L) and the average (avg C_L) lifts is the lift enhancement generated by the initial leading-edge vortex.

The average drag values at large time (avg C_D) for pre-stall angles of attack increase with decreasing aspect ratio due to the classical induced drag effect (Figure 3.8(c)). However for higher angles of attack, drag coefficients are significantly smaller for finite-aspect-ratio wings in contrast to their two-dimensional analog. It is interesting to note that both average lift and drag coefficients become larger past $\alpha = 20^\circ$ for $AR = 2$ wings than those of $AR = 1$, most likely due to the difference in the behavior of the wake at large time (discussed later in Section 3.3.5).

Shown also in Figure 3.8(d) are the average lift-to-drag ratios at large time, avg (C_L/C_D), which are larger for higher aspect-ratio wings. The ratios peak at higher angles of attack for low aspect-ratio plates. While the two-dimensional avg (C_L/C_D) reaches its maximum around $\alpha = 10^\circ$, that of $AR = 1$ is achieved near $\alpha = 20^\circ$. This may suggest favorable operating conditions at higher angles of attack for the low-aspect-ratio wings. For high angles of attack ($\alpha > 40^\circ$), the lift-to-drag ratio for different aspect ratios coalesce to the same value.

Next, we call attention to the time at which the maximum lift is achieved. We denote this time by t^* and present its value on Figure 3.9 for $Re = 300$ and 500. It is found that, for the considered aspect ratios and angles of attack, t^* is fairly constant with a value between 1.25 and 2.25 because the profiles of the leading-edge vortices are similar among all cases. As the accumulation of spanwise vorticity generated by the leading edge contributes to the growth of the leading-edge vortex, there is reminiscence to the formation number used to describe the time at which vortex rings can no longer grow larger in strength (Gharib *et al.*, 1998). Since the formation number is found to be a universal quantity for a variety

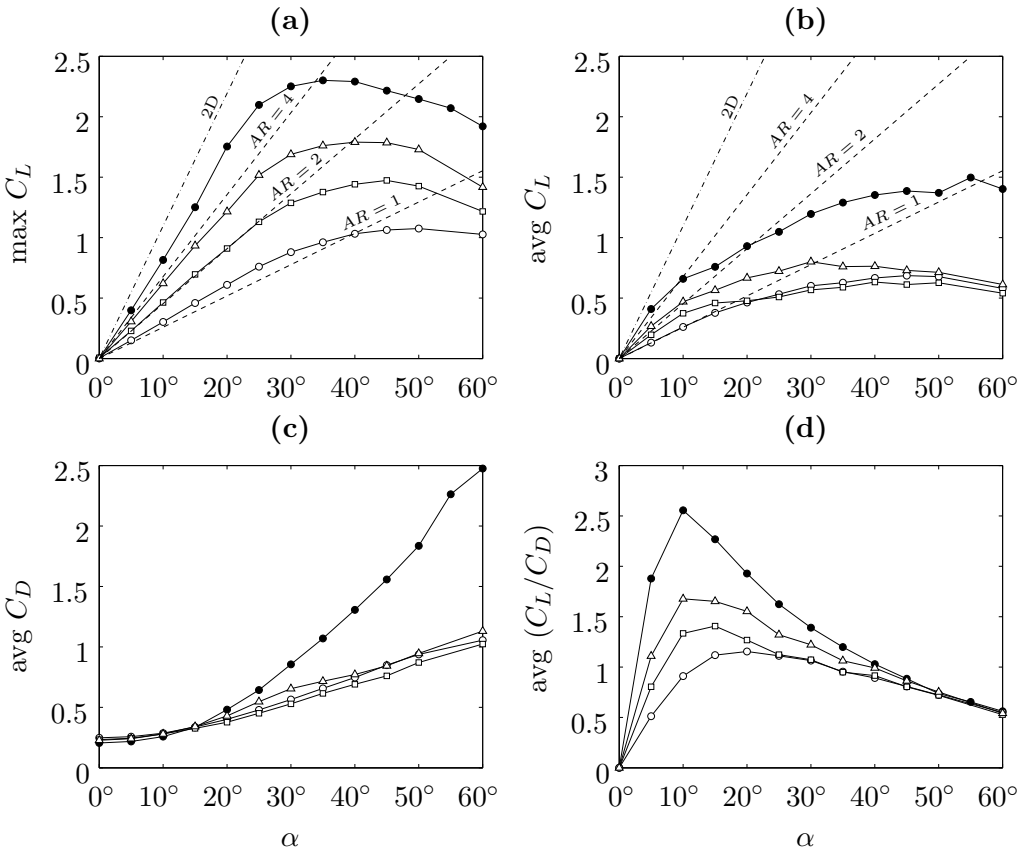

Figure 3.8: Characteristic coefficients for rectangular plates at $Re = 300$: (a) maximum lift; (b) time-averaged lift coefficient at large time; (c) time-averaged drag coefficient at large time; and (d) time-averaged lift-to-drag ratio at large time for $AR = 1$ (∘), $AR = 2$ (□), $AR = 4$ (△), and 2D (•). Overlaid are the two- (—·—) and three-dimensional (----) inviscid lift limits.

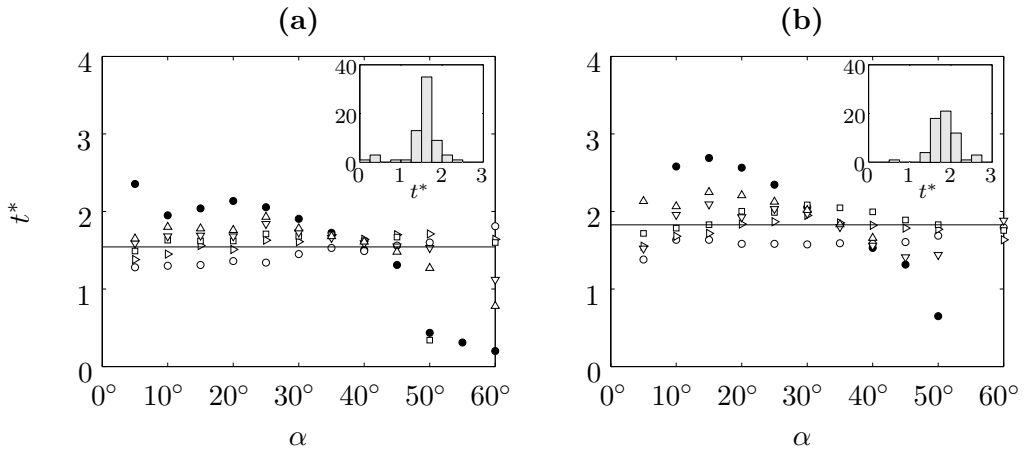

Figure 3.9: Time at which lift achieves the maximum, t^*, after an impulsive start for different angles of attack at (a) $Re = 300$ and (b) $Re = 500$. Symbols denote cases for $AR = 1$ ($\circ$), $AR = 1.5$ ($\triangleright$), $AR = 2$ ($\square$), $AR = 3$ ($\triangledown$), $AR = 4$ ($\triangle$), and 2D ($\bullet$). The mean averages are shown with solid lines. The inset figures are the corresponding histograms.

of flows (e.g., Jeon & Gharib, 2004; Milano & Gharib, 2005), it is not surprising that t^* is also fairly constant for the three-dimensional cases considered here. In the case of two-dimensional flow, we observe a wider range of t^* between 1.3 and 2.4 for $\alpha < 45°$. At higher α, a second local maximum starts to emerge for the two-dimensional flow lowering t^* significantly. Nonetheless, a collection of t^* from all numerical simulations at $Re = 300$ and 500 in Figure 3.9 reveals that the majority of the maxima occur near $t \approx 1.7$ after an impulsive start.

The side force (F_z) remained zero for all cases that reached steady or periodic unsteady flows. However, for aperiodic flow cases observed at high angles of attack, the wake became asymmetric about the mid-span and exerted side forces upon the plate. This unsteady side forces were an order of magnitude smaller than the dominant lift and drag forces experienced by the plate. For all cases considered in this paper (later summarized in Figure 3.12), it was observed that side forces have small magnitudes of $|C_S| = |F_z/(\frac{1}{2}\rho U_\infty^2 A)| < 0.02$. The genesis of these side forces is discussed in the next section.

3.3.4 Correlation between the wake vortices and lift

The objective in this section is to consider metrics that would help visualize vortices that contribute to lift (vortical force) on the plate. We focus on the correlation between the lift history and the wake vortices behind the plate. At early time, following the impulsive start, we observed a remarkable increase in lift due to the formation of the leading-edge vortex immediately above the top surface of the plate. Such universal structures were observed for plates of various aspect ratios and angles of attack exhibiting strong correlation between the vortical topology and large lift. Here we study the wake at large time to see if similar vortices can be found contributing to lift increase in unsteady flows. As an example, the wake behind a plate of $AR = 2$ at $\alpha = 30^\circ$ and $Re = 300$ is considered. Similar observations are made on the correlations between the wake vortices and lift for flows around other aspect-ratio plates.

One of the most frequently used approaches for identifying the dominant flow structures, is the proper orthogonal decomposition (POD). Energetic modes of the flow structures can be computed from the correlation of the flow field over time and space using the method of snapshots by Sirovich (1987). Here a scalar-valued POD is performed upon the Q-value field, with the mean removed. Instead of computing the POD modes of the velocity or vorticity field, we select the scalar Q, as it captures flow structure with significant effect from rotation in comparison to that of shear (i.e., vortex sheet). The most energetic mode of the Q-value that captures 19% of $\|Q\|_2^2$ is illustrated in Figure 3.10(a). In order to attain 90% of the energy of $\|Q\|_2^2$, 20 modes would be required. Since the wake is unsteady with vortices being shed, the first POD mode does capture the alternating nature of the shedding vortices as shown by the light and dark gray contours.

While the POD mode can represent the flow field, this measure does not reflect the forces exerted on the plate. Since the majority of lift is contributed by the difference between the pressure on the top and bottom surfaces, let us consider relating the pressure fluctuation on the top surface with the wake vortices. We do not take the pressure from the bottom surface into account because its fluctuation

caused by the unsteady wake is much less than that of the top surface. Hence we introduce weights and the top surface pressure, p_{t}, for the correlation matrix in the following fashion:

$$\begin{bmatrix} Q(t_1) & p_{\mathrm{t}}(t_1) \\ Q(t_2) & p_{\mathrm{t}}(t_2) \\ \vdots & \vdots \\ Q(t_m) & p_{\mathrm{t}}(t_m) \end{bmatrix} \begin{bmatrix} 0 & 0 \\ 0 & 1 \end{bmatrix} \begin{bmatrix} Q(t_1) & Q(t_2) & \cdots & Q(t_m) \\ p_{\mathrm{t}}(t_1) & p_{\mathrm{t}}(t_2) & \cdots & p_{\mathrm{t}}(t_m) \end{bmatrix}, \tag{3.2}$$

where m is the number of snapshots and the mean values at large time are understood to be subtracted.

Performing a POD of the above matrix, we find that the first mode weighs 58% of the energy defined by the expression (3.2). The Q-value corresponding to the first weighted POD mode is shown in Figure 3.10(b). These pressure weighted modes are able to capture 90% of the energy with only 6 modes in contrast to the 20 modes required by the un-weighted POD discussed earlier. This suggests that most of the forces are generated by the large-scale structures. It should be observed that this metric is able to highlight the influence of the tip vortices on the pressure on the top surface. This is illustrated by the light gray iso-surface structure indicated by the arrow (structure directly behind the tip is underneath the darker gray isocontour). Thus, we argue that this vortical structure in light gray contributes to the increase in lift from the roll-up of the leading edge vortex and the downward velocity induced by the tip vortices.

We can also highlight the influence of wake vortices by considering a lift-weighted Q-value. The idea here is to simply correlate the lift history with the position of the wake vortices at large time to define a metric $\hat{Q}(\mathbf{x})$:

$$\hat{Q}(\mathbf{x}) = \frac{1}{t_2 - t_1} \int_{t_1}^{t_2} \frac{C_L(t) - \operatorname{avg} C_L(t)}{\max\limits_t C_L(t) - \min\limits_t C_L(t)} Q(\mathbf{x}, t) dt, \tag{3.3}$$

where t_1 and t_2 are selected appropriately to capture the large-time behavior of the flow. This weighted Q-value is shifted by subtracting the average lift over

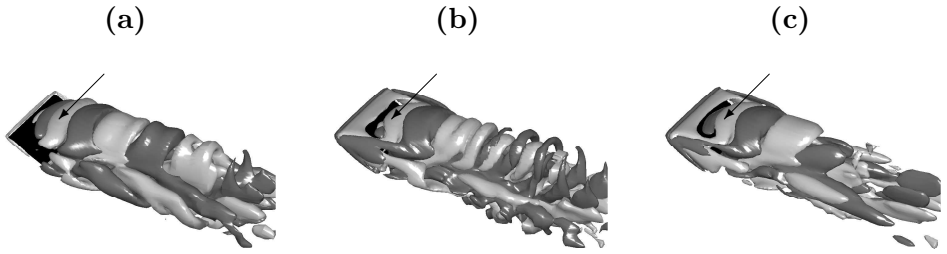

Figure 3.10: Top-port views of (a) the most energetic POD mode of the Q-value, $\tilde{Q}_1$, (b) the most energetic POD mode of the Q-value weighted with the surface pressure, $\tilde{Q}_{p1}$, and (c) the lift weighted Q-value, $\hat{Q}$, behind a rectangular plate of $AR = 2$ for $Re = 300$ at $\alpha = 30°$. The iso-surface levels are set to (a) $\tilde{Q}_1 = \pm 5 \times 10^{-4}$, (b) $\tilde{Q}_{p1} = \pm 9 \times 10^{-2}$, and (c) $\hat{Q} = \pm 2 \times 10^{-2}$. Arrows indicate vortical structures responsible for lift increase identified by $\hat{Q}$ in (c).

large time such that positive and negative values of $\hat{Q}$ correspond to Q-values that correlate with the increase and decrease in lift, respectively. We can only consider unsteady flow at large time with $\hat{Q}$ since steady flow profiles sets $\hat{Q}$ to zero.

This lift-weighted Q-value is shown in Figure 3.10(c). As previously mentioned, the vortical structure from the roll-up of leading-edge vortex sheet is correlated with lift enhancement (as indicated by the arrow). Additionally, the existence of tip-vortices directly behind the plate is found to be associated with the increase in lift. Very similar results are obtained with a drag-weighted Q-value, because drag is highly correlated with lift. This simple quantity is quite similar to the most energetic lift-weighted POD mode near the plate, which makes $\hat{Q}$ attractive in identifying the vortical structure responsible for providing lift increase due to its ease of calculation compared to the POD.

3.3.5 Large-time behavior and stability of the wake

Here we consider the behavior of the wake behind rectangular plates at large time. After the initial transient generated by the impulsive start settles down, the wake reaches one of the three states: (*i*) a stable steady state, (*ii*) a periodic

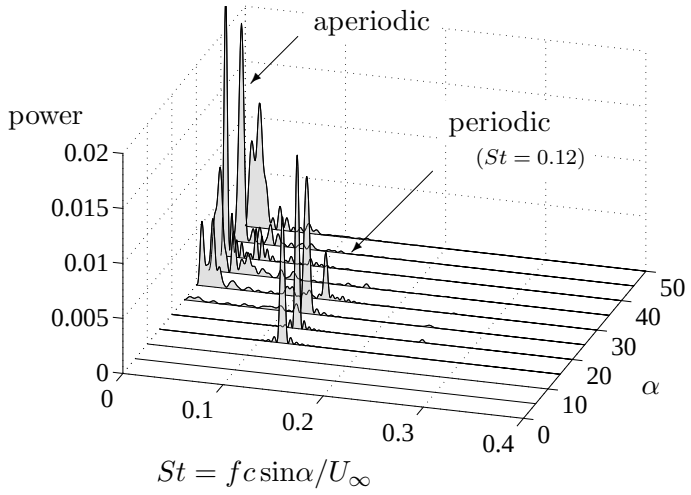

Figure 3.11: Power spectra of the lift trace for a rectangular plate of $AR = 3$ in flows of $Re = 500$ at various angles of attack.

unsteady state, or (*iii*) an aperiodic unsteady state. Examples from each one of these states were presented in Section 3.3.1. In this section, we consider a wide range of parameters ($\alpha \in [0°, 60°]$, $AR = \{1, 1.5, 2, 3, 4\}$, and $Re = \{300, 500\}$), as well as the two-dimensional flows, to survey the stability of the wake at large time. The lift histories, such as the ones in Figure 3.7, are analyzed with Fourier transform to detect any dominant shedding frequencies as shown in Figure 3.11 for an example of $Re = 500$ and $AR = 3$. Depending on the angle of attack, the shedding can occur with a dominant shedding frequency (periodic) or with no clearly recognizable frequency (aperiodic). The dominant frequency in the case of Figure 3.11 is found to be $St = fc\sin\alpha/U_\infty \approx 0.12$ for all spectra of the periodic shedding cases. The corresponding Strouhal number for the two-dimensional flow at $Re = 500$ is slightly higher at $St = 0.14$–0.16.

The wake stability is summarized for in Figure 3.12, which maps α against AR. These two parameters were found to be the two most important parameters in determining the stability of the wake at large time. Suggested boundaries between different flow regimes are drawn based on the data points collected from numerical experiments. The shaded regions correspond to flow conditions that would arrive

at a steady state. Such flow can be either attached at small α or fully separated at moderately high α. The steady state is achieved over a wider limit with lower aspect ratios, since the tip vortices are able to provide a downward induced velocity across a larger extent to prevent the wake vortices from shedding.

As we consider higher angles of attack, the flow exhibits periodically shedding hairpin vortices generated by the leading and/or the trailing edges. This flow profile is observed for the white region left of the dashed line in Figure 3.12. The change in the dynamics between the shaded (sub-critical) and unshaded (super-critical) regions can be can be viewed as an extension of the two-dimensional stability boundary since the instability is generated by the leading- and trailing-edge vortex sheets. We claim that the change in the dynamics is attributed to a Hopf-bifurcation, as shown by Ahuja *et al.* (2007) for the two-dimensional case (in which case, the wake consists solely of leading- and trailing-edge vortices). For lower aspect ratios, the vortex sheet emanating from the trailing edge forms and sheds hairpin vortices repeatedly. The narrow region with $AR \lesssim 2$ in Figure 3.12 corresponds to such flow states. The same region with higher aspect ratio of $AR \gtrsim 2$ shows shedding of both the leading- and trailing-edge vortices alternately in a periodic fashion (for instance the case of $Re = 300$, $AR = 4$, and $\alpha = 30^\circ$ in Figure 3.11 as the peak for the power spectrum at $St = 0.12$ becomes no longer observable for $\alpha > 30^\circ$. In Figure 3.12, this aperiodic unsteady state corresponds to the region right of the dashed line.

The aperiodic flows are found to be asymmetric in the spanwise direction with respect to the mid-span plane. As the wake becomes asymmetric, the wake vortices apply side forces onto the wing and the flow field. The combination of the asymmetry and the nonlinear interaction amongst the leading-edge, trailing-edge, and tip vortices give rise to the aperiodic nature of the flow. An example of an asymmetric wake is shown for a rectangular plate of $AR = 2$ at $\alpha = 40^\circ$ and $Re = 500$ (the wake for the same case at earlier time is shown in Section 3.3.2). The side force for this case has a magnitude of $|C_S| < 0.01$ with a frequency content (no dominant shedding frequency) similar to those low frequency contents

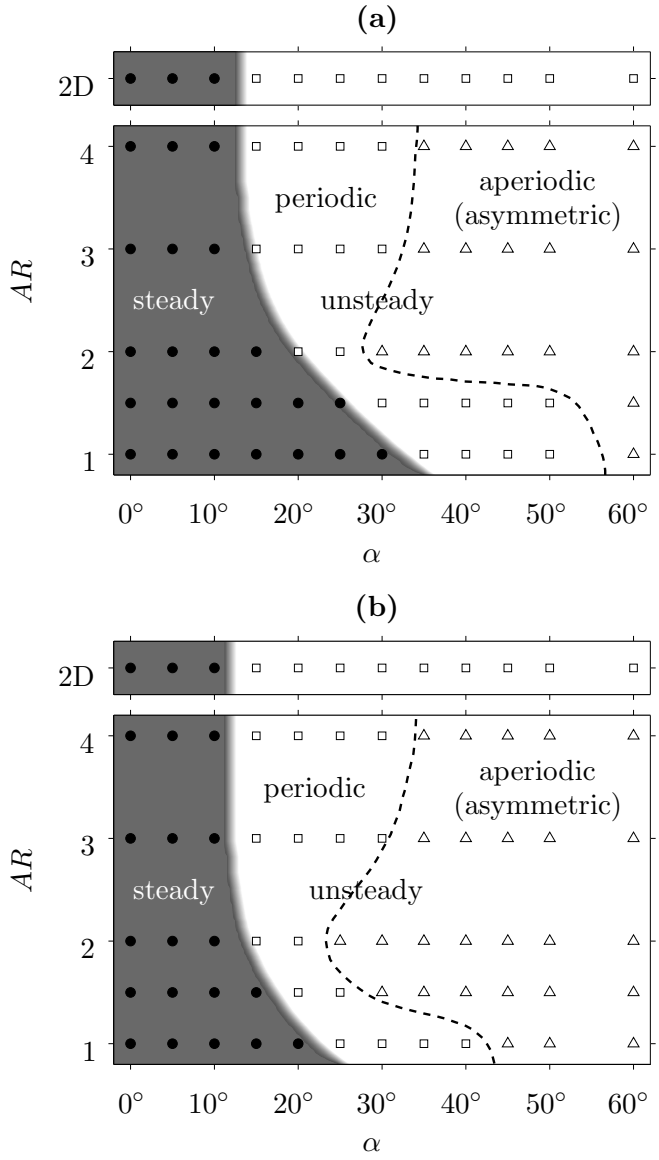

Figure 3.12: Stability of the wake for a range of α and AR at (a) $Re = 300$ and (b) $Re = 500$. Symbols of •, □, and △ denote steady, unsteady periodic, and unsteady aperiodic wakes at large time. The shaded area and the dashed line approximately represent the region of stability and the transition from periodic to aperiodic shedding, respectively. Shown at the top are the two-dimensional (2D) findings.

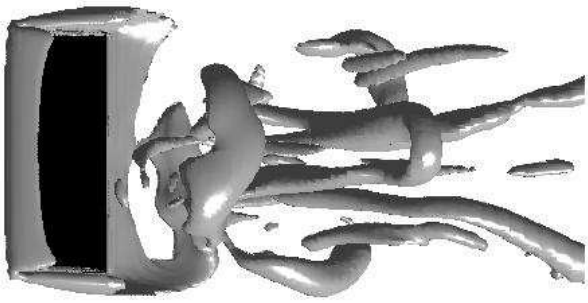

Figure 3.13: Top view of the asymmetric wake at large time behind a rectangular plate of $AR = 2$ at $\alpha = 40^\circ$ and $Re = 500$. Vortices are highlighted with iso-contours of $Q = 2.5$. The flow is directed from left to right and the wing is shown in black.

on Figure 3.11. Asymmetry is not observed for steady or periodic unsteady flows.

For much larger aspect ratios than those considered here, the wake most likely develops into either a stable steady state or a periodic shedding profile. However, the actual three-dimensional flow with infinite span would probably not be purely two-dimensional, as seen for three-dimensional flows around an circular cylinder of infinite span (Braza *et al.*, 2001). With perturbation in the spanwise direction, the vortical structure forms cellular patterns (stall cells), similar to those observed in the $AR = 4$ case (Figure 3.5) and those previously reported by Winkelmann & Barlow (1980) and Yon & Katz (1998).

The stability of the wake is also influenced by the Reynolds number. In Figure 3.12, we notice that for $Re = 500$, the steady flow profile is achieved for a smaller range of angles of attack and aspect ratios compared to the $Re = 300$ case. Similar trend holds for the periodic shedding case. With increasing Reynolds number, it is expected that the wake exhibit strong interaction between the leading-edge and tip vortices resulting in aperiodic/asymmetric flows for a wider combination of angles of attack and aspect ratios.

For much higher Reynolds numbers, there may be additional instability

mechanisms that are not observed in the present study. In such cases, it may be possible to observe changes in the shape of the stability boundary between the periodic and aperiodic shedding regimes. Additional studies are necessary to determine if the stability maps (Figure 3.12) display different features at higher Reynolds number.

We have classified the wake stability based on the spectra of the lift history. This is performed to remove ambiguity in the exact location of where a probe should be positioned in case of the use of wake measurements and their corresponding spectra. Here we compare the spectra from lift history and wake measurements of v and p. Probes for the wake measurements are positioned behind the plate at points $A = (2, 0, 0)$ and $B = (2, 0, b/2)$, where $b/2$ is the half-span of the wing ($c = 1$) centered at the origin (see Figure 3.1 for setup). Point A is located at the midspan and point B is placed directly behind the wing tip.

In order to highlight the differences in the flow behavior, we present three different shedding cases. Namely, they are (I) a periodic case with $Re = 300$, $AR = 1.5$, and $\alpha = 50°$; (II) an aperiodic case with $Re = 300$, $AR = 2$, and $\alpha = 30°$; and (III) another aperiodic case with $Re = 500$, $AR = 2$, and $\alpha = 40°$. Cases (I) and (II) are selected as they are near the stability boundary between the periodic and aperiodic cases. The other aperiodic case (III) is chosen to be away from such boundary.

Figures 3.14 to 3.16 exhibit the wake measurements and their corresponding spectra for cases (I) to (III). The periodic case (I) in Figure 3.14 exhibits a clear dominant shedding frequency in both the lift history and wake measurements. When we consider an aperiodic case near the boundary, case (II), we observe that the lift spectra no longer shows a single dominant shedding frequency. However, this shedding frequency is still observed in the v and p spectra at point B. Hence, depending on the location of the probe (i.e., near the tip vortex), one can observe a periodic flow pattern. This indicates that the nonlinear vortex interaction does indeed result in overall aperiodic flow pattern, and correspondingly an aperiodic lift history. For case (III), which is away from the stability boundary, the distinct

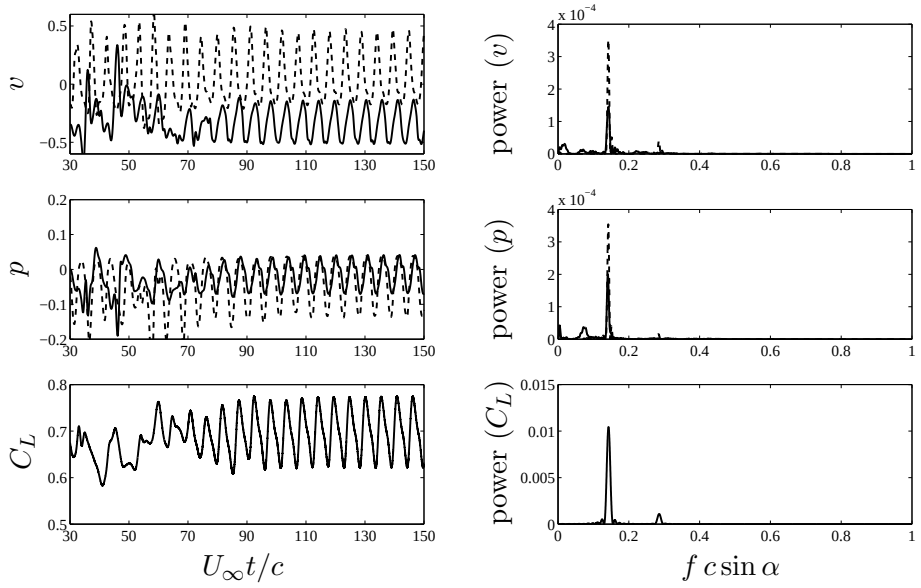

Figure 3.14: Wake measurements (left) and their power spectra (right) for a *periodic* **shedding case (I) of** $Re = 300$**,** $AR = 1.5$**, and** $\alpha = 50°$**. Probes are located at** $A = (2, 0, 0)$ **and** $B = (2, 0, 0.75)$ **corresponding to the solid and dashed lines, respectively. Also, presented is the lift history and its power spectrum.**

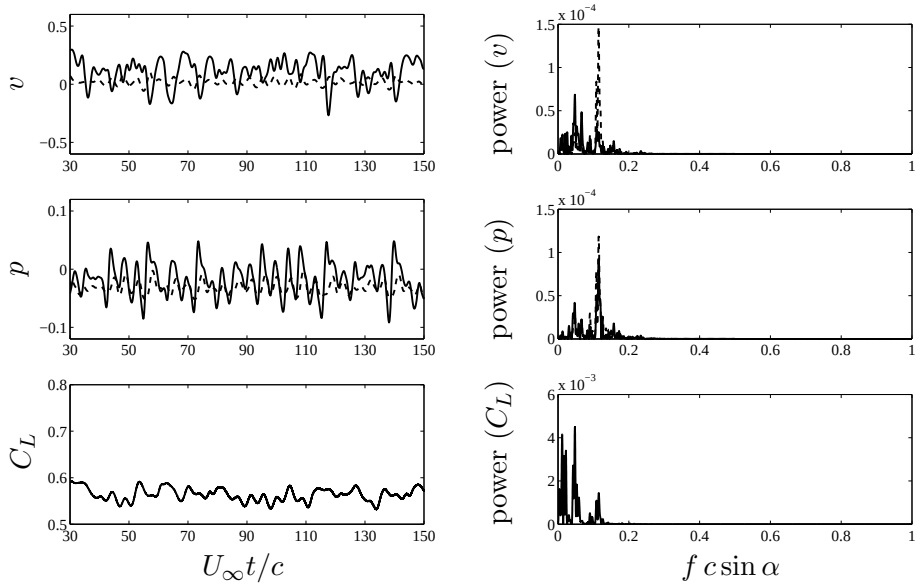

Figure 3.15: Wake measurements (left) and their power spectra (right) for an *aperiodic* **shedding case (II) of** $Re = 300$**,** $AR = 2$**, and** $\alpha = 30°$**. Probes are located at** $A = (2, 0, 0)$ **and** $B = (2, 0, 1)$ **corresponding to the solid and dashed lines, respectively. Also, presented is the lift history and its power spectrum.**

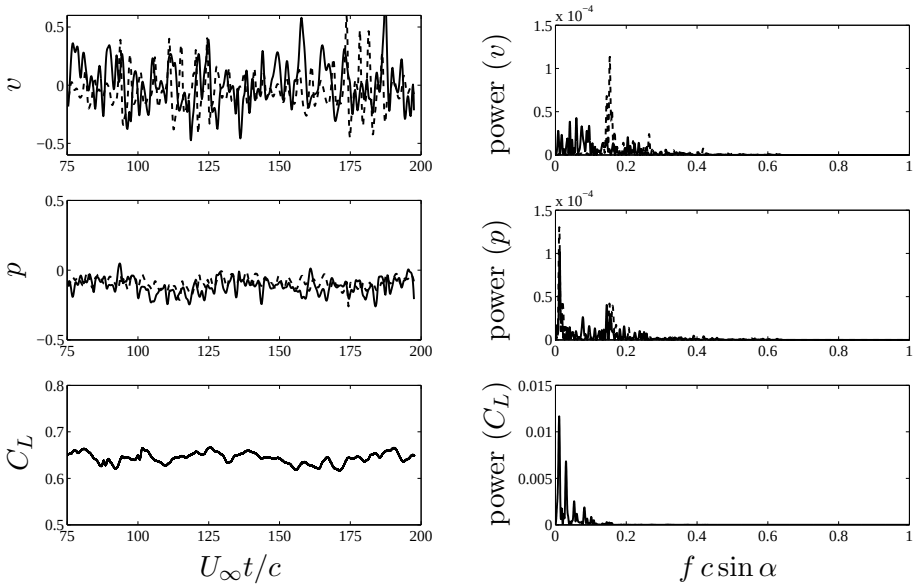

Figure 3.16: Wake measurements (left) and their power spectra (right) for an *aperiodic* shedding case (III) of $Re = 500$, $AR = 2$, and $\alpha = 40°$. Probes are located at $A = (2, 0, 0)$ and $B = (2, 0, 1)$ corresponding to the solid and dashed lines, respectively. Also, presented is the lift history and its power spectrum.

shedding frequency observed in the periodic case is only observed in v at point B. Compared to case (II), the spectra for case (III) is spread over a wider range of frequency suggesting a stronger nonlinear interaction of the wake vortices[3]. Again as shown in Figure 3.11, we note that there is a clear transition from the periodic to aperiodic (asymmetric) regime as indicated by the flow measurements and the power spectra we presented.

3.3.6 Non-rectangular planforms

Stable attachment of the leading-edge vortices on flapping wings has been observed to provide enhanced lift for prolonged duration (Birch *et al.*, 2004; Poelma *et al.*, 2006). Shedding of these vortices are prevented by releasing the spanwise vorticity

[3]For case (III), there may be a low frequency behavior as indicated by the p and C_L histories. However, simulation was not ran long enough to distinguish whether there is a distinct associated frequency.

through convective transport from the root to the tip of the wings induced by wing rotation. Hence, a continuously connected vortical structure formed by the leading-edge and tip vortices are observed for flapping or revolving wings.

For rectangular plates in pure translation, we have shown earlier that the initial leading-edge vortex detaches in a similar fashion to dynamic stall. The leading-edge and tip vortices remain as separate vortical structures and do not provide a mechanism for the spanwise vorticity to be released other than shedding. In order to prevent or delay the shedding of the leading-edge vortex, we consider the use of curved or angled leading edges to induce flows along the leading edge. Flows around elliptic, semicircular, and delta-shaped planforms are simulated at $\alpha = 30^\circ$ and $Re = 300$ in comparison to the flow around a rectangular plate of $AR = 2$ presented earlier. The geometries of the elliptic, semicircular, and delta-shaped planforms are chosen with $AR = 2$, $4/\pi$, and 2, respectively, whose mean chord lengths are used to non-dimensionalize all spatial variables. For the delta wing, the sweep angle is set to 45°.

Wake structures behind the non-rectangular planforms are shown in Figure 3.17 after the impulsive start with the corresponding forces in Figure 3.18. For the elliptic and semicircular cases, there are no discontinuities in the vortex sheet that emanates from the leading edge to the tips, unlike the sharp separation of the vortical structures around the corners on the rectangular planforms. The curved leading edge encourages spanwise transport of vorticity into the tip vortices. Hence to some extent the shedding of the leading-edge vortical structure is delayed. While the leading-edge hairpin vortex first detaches around $t \approx 8$ for the rectangular planform, such separation is observed at a later time ($t \approx 15$) for the elliptic and semicircular plates. This gentle detachment allows the forces to decay smoothly instead of generating fluctuations, as seen for the rectangular planform around $t \approx 8$ due to the detachment of two consecutive leading-edge vortices. At later time, both the flows behind the elliptic and semicircular wings exhibit periodic shedding, which is different from the rectangular case.

A steady state is achieved by the flow around the delta-shaped planform. There

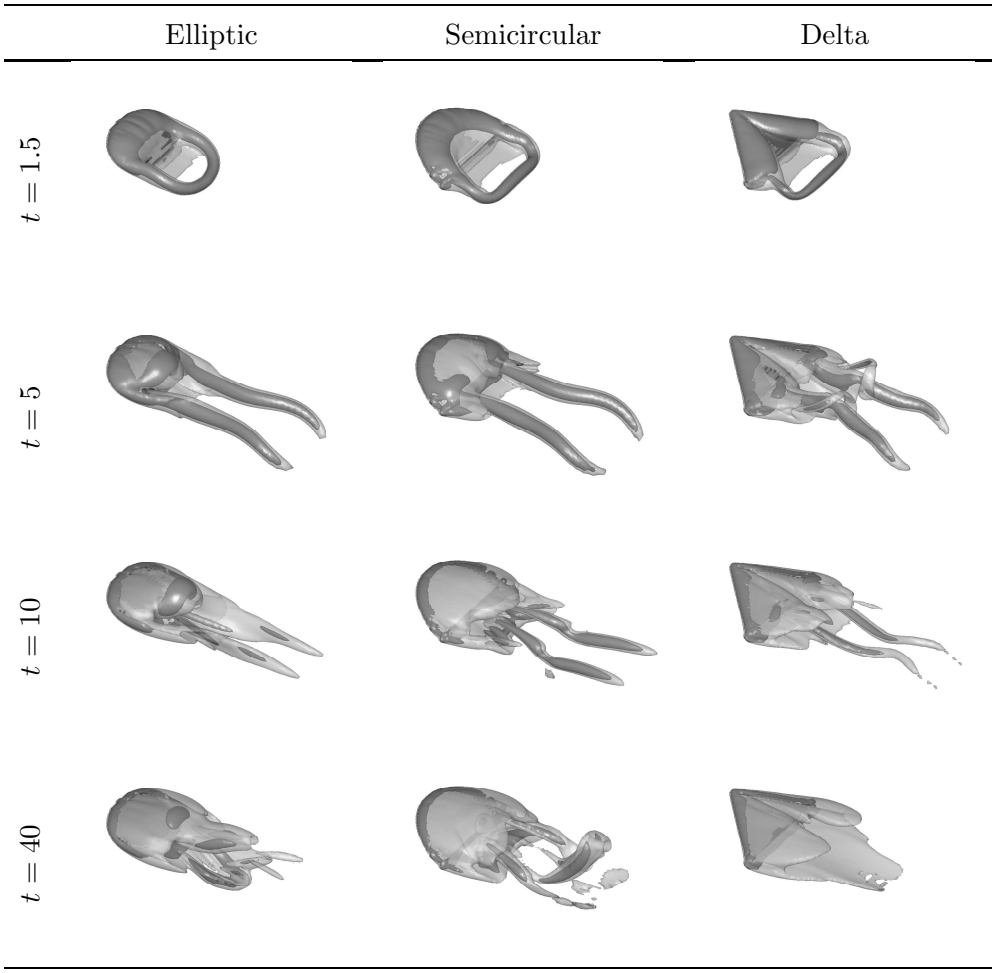

Figure 3.17: Top-port views of the wake vortices behind different planform geometries at $\alpha = 30^\circ$ and $Re = 300$ with the iso-surface of $\|\boldsymbol{\omega}\|_2 = 3$ in light gray with vortex cores highlighted by the iso-surface of $Q = 3$ in dark gray.

is a clear distinction of the left and right vortex sheets from the nose of the plate, but the roll-up of the vortex sheets forms a stable wake structure which in turn attains steady lift and drag. The absence of wing tips for this planform allows the vortex sheets from the leading edge to roll up and convect downstream in a very stable manner (see Figure 3.17). For $Re = 300$, the size of initial leading-edge vortices is larger compared to ones from higher Reynolds number flow (Gursul *et al.*, 2005). One can observe transient behavior of the wake until $t \approx 15$. Beyond this point in time, there is some unsteady shedding of small vortical structures behind the rolled up vortices. However, the wake and the forces do not change much past $t \approx 15$ approaching the steady state.

We observe a relative increase in transport of the spanwise vorticity around non-rectangular planforms in comparison to the rectangular planform as illustrated by iso-surface of $|\mathbf{u} \cdot \nabla \omega_z|$ in Figure 3.19. It should be noticed that there is an absence of transport of ω_z near the leading edge for the rectangular wing in contrast to the semicircular and delta-shaped planforms. The force histories presented in Figure 3.18 show that the time of maximum lift is somewhat delayed to $t^* \approx 2$ for the elliptic and semicircular wings, in comparison to $t^* \approx 1.7$ for the rectangular plate of $AR = 2$. Nonetheless, the plates experience a drop in lift due to the separation of the leading-edge vortices later in time. This detachment is caused by the insufficient spanwise transport to sustain a stable attachment of the leading-edge vortex.

While the vortical flows are different for various planform geometries, the lift and drag exerted on the wings do not show significant variations in Figure 3.18. This is most likely due to the viscous nature of the flows at this low Reynolds number. In addition, the similar aspect ratios considered here may be responsible for the similar values in forces. We do also observe differences in the behavior and stability of the wakes. The stability diagram presented in Figure 3.12 for the rectagular plate would not carry over to the cases of non-rectangular planforms due the difference in the influence of the tip vortices.

For flapping wing aerodynamics, the wing kinematics restricts the wing stroke

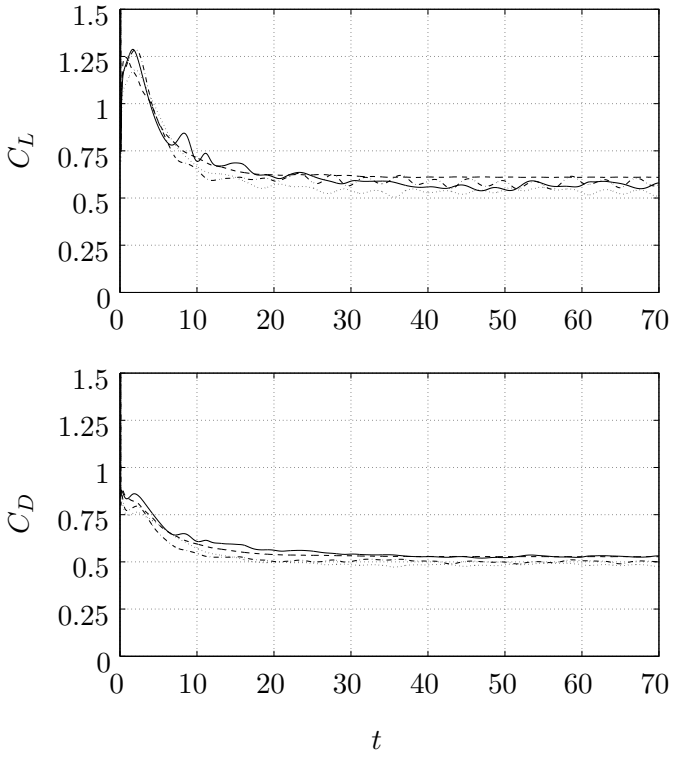

Figure 3.18: Time trace of lift and drag coefficients for rectangular (——), elliptic (·····), semicircular (—·—), and delta-shaped (- - - -) planforms at $\boldsymbol{Re} = 300$ and $\alpha = 30°$.

Rectangular	Semicircular	Delta
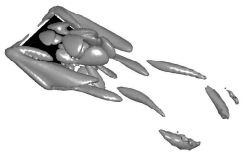	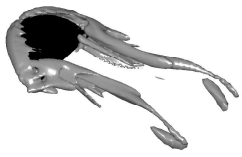	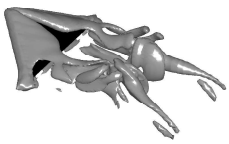

Figure 3.19: Top-port views of the convective transport of spanwise vorticity shown by the iso-surface of $|\mathbf{u} \cdot \nabla \omega_z| = 3$ at $t = 5$.

and periodicity. In such cases, the travel distance even at the wing tip is much smaller and is about πARc. Even a small increase in aerodynamic performance or stable flow features can be of benefit. Although the added effect of rotation or spanwise flows are not taken into account in this study, the wing planform can be of importance as we have discussed in the non-rectangular cases, at least without regard to structural constraints or maneuverability. For purely translating flights, the initially formed leading-edge vortex does not stay attached for most planform geometries as reported around rotating wings. As discussed in previous studies, it is suspected that rotation is one of the main mechanisms for the stable attachment.

3.4 Summary

We presented results from numerical simulations of three-dimensional separated flows around low-aspect-ratio flat-plate wings at low Reynolds numbers using an immersed boundary method. Both the initial transient and long time behavior of the flow was studied by simulating an impulsively started plate in pure translation. The unsteady nature of the separated flow and vortex dynamics was highlighted.

A number of simulations were performed for $Re = 300$ and 500 with various aspect ratios, angles of attack, and planform geometries. The aspect ratio and angle of attack were found to have a large influence on the stability of the wake profile and the force experienced by the body. At early times, topologies of the wake vortices were found to be the same across different aspect ratios and angles of attack. Behind low-aspect-ratio rectangular plates, leading-edge vortices were found to form and eventually separate as hairpin vortices following the initial impulsive translation. This phenomenon was found to be similar to dynamic stall observed behind pitching plates. The detached structure would then interact with the tip vortices, reducing the downward velocity induced by the tip vortices acting upon the leading-edge vortex. At large time, depending on the aspect ratio and angles of attack, the wakes reached one of the three states: (*i*) a steady state, (*ii*) a periodic unsteady state, or (*iii*) an aperiodic unsteady state. The aperiodic

unsteady state is found to be asymmetric in the spanwise direction and is caused by the strong interaction between the leading-edge, trailing-edge, and tip vortices.

Lift achieved the maximum value soon after the impulsive start and decreased afterward to approximately half of the maximum value at large time. It was observed that for most of the cases maximum lift in time was achieved at a non-dimensional time around $t^* \approx 1.7$ regardless of the aspect ratio, angle of attack, and planform geometry. We remarked on the reminiscence to the formation number and its possible universality of this non-dimensional time.

Proper orthogonal decomposition and lift-weighted Q-values were considered to highlight the vortical structures that apply vortical forces to provide added lift. It was observed that the residence of the leading-edge and tip vortices have strong correlation with the increase in lift.

Elliptic, semicircular, and delta wings were also considered. By providing curvature along the leading edge, convective transport of vorticity from the mid-span to the tip somewhat delayed the separation of the leading-edge vortex. However the curvature for these planforms could not induce sufficient transport of spanwise vorticity to prevent the shedding of the leading-edge vortices. The wakes behind non-rectangular wings were observed to be different from the cases of rectangular planforms in terms of the shedding pattern (stability) and the influence of the tip vortices. However, the overall trend for the lift and drag histories were found to be similar to those of the rectangular case.

Three-dimensional separated flows behind low-aspect-ratio plates were found to be vastly different from the analogous two-dimensional flows. We have observed that the tip effects in three-dimensional flows can stabilize the flow and also exhibit nonlinear interaction of the shedding vortices. Even when the aspect ratio is increased to 4, the flow along the mid-span does not approach the two-dimensional von Kármán vortex shedding since spanwise cellular structures (stall cells) emerge. Asymmetric wakes about the mid-span were also observed for aperiodic flows around rectangular wings at high angles of attack. Furthermore, the tip vortices and their interaction with the other wake vortices were significantly influenced by

the planform geometry.

Chapter 4

Flow Control around Low-Aspect-Ratio Wings

4.1 Introduction

In an effort to develop micro air vehicles (Mueller, 2001; Mueller & DeLaurier, 2003; Pines & Bohorquez, 2006), a number of studies have been carried out to understand and characterize the low-Reynolds-number aerodynamics around low-aspect-ratio wings (Freymuth *et al.*, 1987; Pelletier & Mueller, 2000; Sunada *et al.*, 2002; Torres & Mueller, 2004; Cosyn & Vierendeels, 2006). The experiments by Torres & Mueller (2004) have characterized the aerodynamic performance of various low-aspect-ratio wings at Reynolds numbers (Re) of $\mathcal{O}(10^5)$. Such flows are found to be vastly different from those at high Reynolds numbers around high-aspect-ratio wings due to the viscous effects and three-dimensionality. A comprehensive list of experimental and numerical studies of the aerodynamics for micro air vehicles are compiled in Mueller (2001). More recently, Taira & Colonius (2008) (also presented in Chapter 3) have studied the three-dimensional separated flows behind low-aspect-ratio wings at post-stall angles of attack at $Re = \mathcal{O}(100)$ with emphasis on the vortex dynamics. It was observed that the tip-vortices have significant influence on the wake structures and the corresponding forces exerted

on the wings.

In addition to the unique wing designs and the flight Reynolds number, micro air vehicles operate under large wing gusts. Hence, flow control becomes a key requirement on the vehicle to provide stable performance. Past investigations by Seifert *et al.* (1996) and Greenblatt *et al.* (2001) have employed periodic excitation to delay airfoil stall. Here we conduct an exploratory numerical study with steady blowing applied to low-Reynolds-number flows around low-aspect-ratio wings. Steady forcing is considered here to reduce the parameter space (namely the actuation frequency). Similar studies to the current investigation are the circulation control (Englar, 2000) that enhances lift by increasing the spanwise circulation. Moreover, Lee *et al.* (1989), Duraisamy & Baeder (2006), and Holloway & Richardson (2007) have also used steady blowing to attenuate the maximum velocity induced by the tip vortices for safety concerns in air traffic control (Spalart, 1998).

At post-stall angles of attack, wings experience reduced lift from the separated flows. However, specific arrangements of the wake vortices are known to provide enhanced aerodynamic performance. For example, insects are known to benefit from the wake vortices to increase lift during the flapping flights. The stable attachment of the leading-edge vortices provides added spanwise circulation, yielding large increase in lift (Dickinson & Götz, 1993; Ellington *et al.*, 1996; Birch & Dickinson, 2001; Birch *et al.*, 2004; Poelma *et al.*, 2006). Inspired by how animals favorably use vortical forces to increase lift, we investigate the application of steady blowing to alter the dynamics of the wake vortices behind low-aspect-ratio wings to achieve lift enhancement (direct wake modification (Choi *et al.*, 2008)). Our objective here is not to reattach the flow or suppress the unstable modes in the wake.

In the next section, we present the actuator model used to study the effect of actuation on the three-dimensional flows around the low-aspect-ratio rectangular flat-plate wings. The applications of steady blowing are considered to increase the lift exerted on the plate. Various actuator positions and locations are examined

and two setups are identified for lift enhancement by utilizing the tip effects. One of the effective control setups is further examined for a wide range of aspect ratios and angles of attacks and is found to increase lift in all cases.

4.2 Controlled flow

As we have seen in Section 3.3.3, the lift experienced by the rectangular wing at early time following the impulsive start is significantly larger than the lift at large time. Our objective in this section is to apply steady flow control to the separated flow such that the lift at large time is increased as high as the lift attained during the unactuated transient flow. The current approach focuses on enhancing lift by changing the dynamics of wake vortices and not by suppressing the unstable wake modes or reattaching the flow.

4.2.1 Actuator model

In the following simulations, we introduce a body force to model steady blowing. This time-invariant force is applied to the flow field as a uniform strip along the span expressed as

$$\mathbf{f}_{\text{act}} = \hat{\mathbf{f}}_{\text{act}}\,\delta(x-x_0)\,\delta(y-y_0)\,\Gamma\left(-z+\frac{b}{2}\right)\,\Gamma\left(z+\frac{b}{2}\right) \tag{4.1}$$

and is added to the right-hand side of the momentum equation, Eq. (2.1). For the current model, addition of mass to the system is not taken into account. Here $\hat{\mathbf{f}}_{\text{act}}$ prescribes the strength and the direction of the actuator. The location of the actuator is specified with (x_0, y_0) in the spanwise plane and b denotes the span of the plate. The function $\Gamma(\,)$ corresponds to the Heaviside step function representing a strip in the spanwise direction. In the computations, the singular delta function, $\delta(\,)$, is replaced by a discrete delta function, $\tilde{\delta}(\,)$, proposed by Roma *et al.* (1999) that regularizes the singularity across 3 cells in both the x- and y-directions. This delta function is also used in the immersed boundary projection

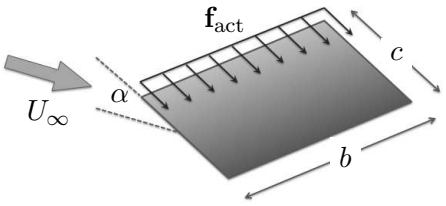

Figure 4.1: A flow control setup shown for an example of actuation along the leading edge in the downstream direction.

method to represent the immersed boundary, Eq. (2.14).

The discrete delta function is selected to use the smallest possible width for the actuator, which is limited by the resolution of the simulation. Hence, the modeled slot width is set to $\sigma = \Delta x = 0.04c$, the effective width of the discrete delta function. Compared to the typical slot widths of $\sigma/c \approx 0.01$ used in flow control (Lee *et al.*, 1989; Duraisamy & Baeder, 2006; Holloway & Richardson, 2007), the current slot width in our simulations is slightly larger. Nonetheless the present forcing function is used to explore control techniques at this low Reynolds number.

The actuator is not placed exactly on the surface of the plate to avoid the numerical interference of the boundary force used in the immersed boundary method. The controller is positioned $3\Delta x$ from the plate on the suction side. Forcing directions of upstream, sideways (outward from the midspan to the tip), and downstream are considered. A representative flow control setup is provided in Figure 4.1.

4.2.2 Strength of actuation

The strength of the actuation is reported in the present study with the non-dimensional momentum coefficient:

$$C_\mu \equiv \frac{\rho U_{\text{act}}^2 b \sigma_{\text{act}}}{\frac{1}{2}\rho U_\infty^2 b c} = 2\left(\frac{U_{\text{act}}}{U_\infty}\right)^2 \left(\frac{\sigma_{\text{act}}}{c}\right), \tag{4.2}$$

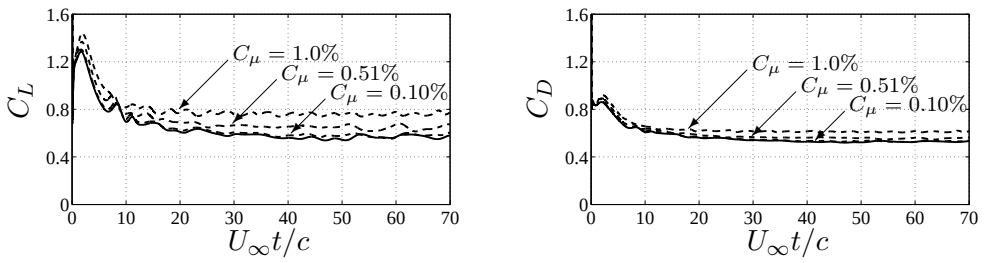

Figure 4.2: Forces on the plate with leading-edge actuation for $C_\mu = 0.10\%$, 0.51%, and 1.0%. Solid and dash lines correspond to unactuated and actuated cases, respectively.

where U_{act} is the actuator velocity. To characterize the actuator model, we simulate this steady blowing with a prescribed $\hat{\mathbf{f}}_{\text{act}}$ in an initially quiescent free space. Once steady state is achieved, the velocity at the center of forcing is selected as the characteristic velocity U_{act}. For example, $|\hat{\mathbf{f}}_{\text{act}}| = 0.1$ corresponds to $U_{\text{act}}/U_\infty = 0.356$ and $C_\mu = 1.0\%$.

Next, we consider the strength of actuation required to alter the flow field in a noticeable manner. In order to alter the dynamics of the wake vortices in a low-Reynolds-number flow, rather large values of C_μ are selected to overcome the viscous effect (and due to the large slot width limited by the grid resolution). Standard values of the momentum coefficient in past studies have ranged from $C_\mu = 0.01\%$ to 10% for applications of steady blowing on wings (Lee *et al.*, 1989; Duraisamy & Baeder, 2006; Holloway & Richardson, 2007). To illustrate the change in the forces exerted upon the plate, we apply flow control around a rectangular plate of $AR = 2$ at $\alpha = 30^\circ$ and $Re = 300$. This example is chosen as the wing is at very high post-stall angle of attack generating strong interaction of the wake vortices and asymmetry about the midspace in the unactuated case (Taira & Colonius, 2008). Actuation along the leading edge in the downstream direction with $C_\mu = 0.10\%$, 0.51%, and 1.0% are considered.

Figure 4.2 exhibits the changes in the lift and drag forces resulting from the leading-edge actuation with varying C_μ. With an actuation effort of $C_\mu = 0.10\%$, there are no pronounced changes in the forces. As the momentum coefficient

is increased to 0.51%, lift starts to show increase from the unactuated case. It is interesting to note that the drag history is less affected by the actuation in comparison to the lift increase. With $C_\mu = 1.0\%$, a significant increase in lift of 33.8% is observed at large time in a time-averaged sense. Steady blowing here is modeled through a body force with a magnitude in the lift direction of $\int |\mathbf{f}_{\text{act}}| dV \sin 30^\circ / \frac{1}{2}\rho U_\infty^2 bc = 0.1$ (17.6% of unactuated lift), which tells us that the rest of the increase must be attributed by the vortical forces. In what follows we consider the use of $C_\mu = 1.0\%$ to explore actuation locations and directions for the same example problem. Once a favorable setup for flow control is identified, other conditions are examined later in this paper.

4.2.3 Location and direction of actuation

Below we consider the application of steady blowing along the leading edge, midchord, and trailing edge in the upstream, sideways, and downstream directions (all parallel to the surface of the plate) with $C_\mu = 1.0\%$. Sideways actuation is directed outward from the midspan to the tips of the wing. The lift and drag histories from the controlled flows are presented in Figure 4.3.

The top two subfigures in Figure 4.3 show the force histories for the cases of leading-edge actuation. Lift is increased with downstream blowing, as the separated flow structures become closer to the surface of the plate. The corresponding low-pressure vortex cores sit directly above the top surface enhancing lift by 34% as mentioned in the previous section. The downstream blowing also repositions the wake vortices downward past the trailing edge increasing the effective frontal area. This in turn causes the drag to increase by 16%, a smaller amount compared to lift.

With flow control in the upstream direction, the leading-edge vortices are pushed into the freestream from the top surface, resulting in the loss of the low-pressure region near the surface and, accordingly, a decrease in lift. Outward forcing was applied in hope of releasing the vorticity generated by the leading

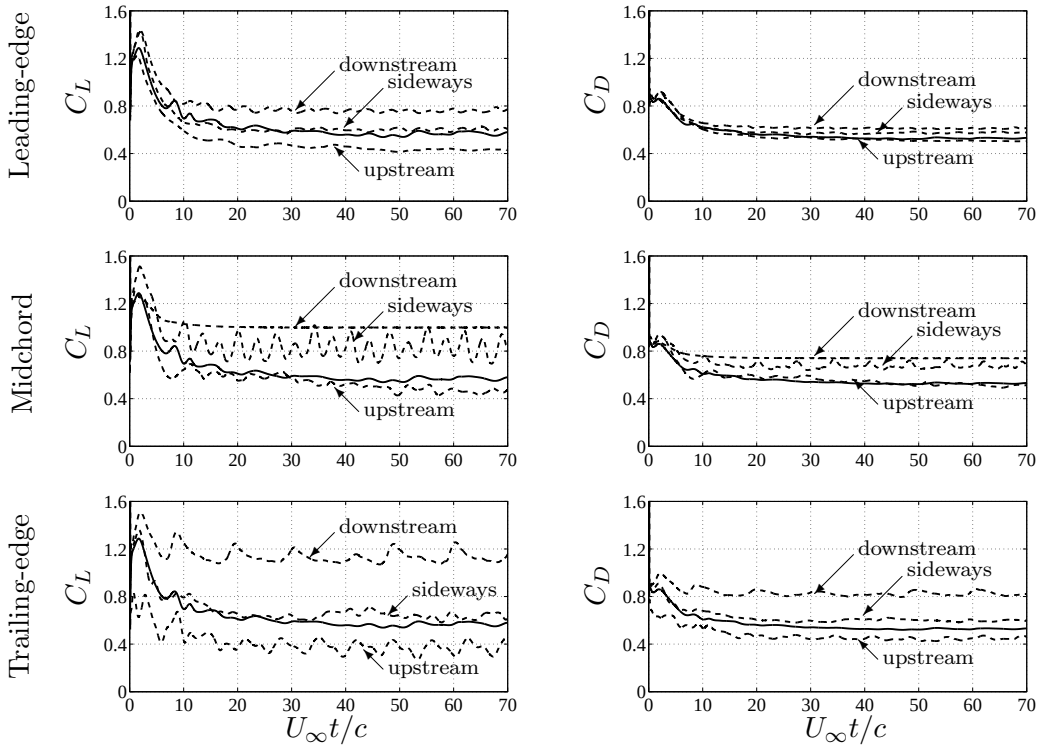

Figure 4.3: Lift and drag histories for cases of leading-edge, midchord, and trailing-edge actuation with $C_\mu = 1.0\%$ applied to the separated flow around a rectangular plate of $AR = 2$ at $\alpha = 30^\circ$ and $Re = 300$. Solid and dash lines correspond to unactuated and actuated cases, respectively.

edge by inducing spanwise flow from the midspan to the tips[1]. However, the right-angled corners on the wing separate the vortex sheets emanating from the leading edge and tip, and triggered the roll up of individual structures (i.e., the leading-edge and tip vortices). Hence the leading-edge vortex and the tip vortices remained disconnected at all times without merging or connecting, in spite of sideways blowing[2]. The overall wake structure was more spread in the spanwise direction than the unactuated flow but did not have much influence on the lift or drag exerted on the plate.

The middle two subfigures in Figure 4.3 illustrate the effect of midchord actuation onto the lift and drag histories. The noticeable change from the control comes from the downward forcing where the flow achieves a steady state and a 76% increase in lift by creating an elongated wake structure (shown in the next section). The vorticity produced by the plate is stably released to the freestream from the leading-edge vortex sheet and the tip vortices at this low Reynolds number. Although this actuator setup is attractive, it would be unlikely to yield a steady flow at higher Reynolds numbers since maintaining such stable wake structure is highly dependent on viscous diffusion. We note that the drag is also affected as the wake structure is moved downward with downstream blowing.

Another change in the dynamics of the wake is exhibited by the sideways blowing along the midchord. This control arrangement repositions the tip vortices away from the plate and allows the leading- and trailing-edge vortices to roll up and shed in a periodic manner. Such behavior of the flow results in a large fluctuation of lift on the wing.

The wake is found to be most sensitive to momentum injection at the trailing edge out of the locations considered in Figure 4.3. The lift shows significant

[1]Spanwise blowing has been shown by Campbell (1976) to generate large increse in lift at high angles of attack for swept wings with $C_\mu = 4\%$ to 31%.

[2]One can remove the influence of the corners by considering non-rectangular planforms, such as the semicircular wings. Flow control on flows around semicircular wings are under way and also have been investigated experimentally by Prof. David Williams' group at Illinois Institute of Technology for $Re = \mathcal{O}(10^4 - 10^6)$.

increase and decrease with the application of downstream and upstream forcing, respectively. The time-averaged lift is increased by a remarkable 100% for downstream blowing. Such noticeable changes in forces are not realized for the sideways blowing at the trailing edge.

The reason for the strong influence of the actuation upon the forces is the direct modification of the trailing-edge vortex. Upstream and downstream blowing, respectively, encourages and discourages the interaction between the leading- and trailing-edge vortices. Below we will further examine how the downstream actuation at the trailing edge modifies the vortex dynamics in the vicinity of the wing and contributes to lift enhancement.

Briefly summarizing the findings here, we have observed that steady blowing can change the dynamics of the wake vortices to increase or decrease lift and drag. From the three locations considered, the trailing edge is observed to affect the force on the wing in the most substantial manner. At all three actuator positions, steady blowing in the downstream direction enhanced lift whereas the upstream direction reduced lift. The most effective actuator for the considered example is found to be at the trailing edge in the downstream direction, achieving double in lift at large time from the change in the dynamics of the wake vortices.

4.2.4 Wake modification with actuation

Let us visualize the flow field around the rectangular plate of $AR = 2$ at $\alpha = 30^\circ$ and $Re = 300$ for the two most effective cases of actuation from the above discussion, namely the downstream blowing at the midchord and at the trailing edge. Similar to the flow visualization employed in Figure 3.5, representative snapshots of the wake vortices at large time ($U_\infty t/c = 70$) with and without actuation are illustrated in Figure 4.4 with the isosurfaces of $\|\boldsymbol{\omega}\|_2 = 2$ and $Q = 1$. Also presented are the time-averaged pressure fields and the streamlines along the midspan.

The unactuated flow exhibits complex interaction amongst the leading-edge, trailing-edge, and tip vortices with the dominant flow structures mostly consisting

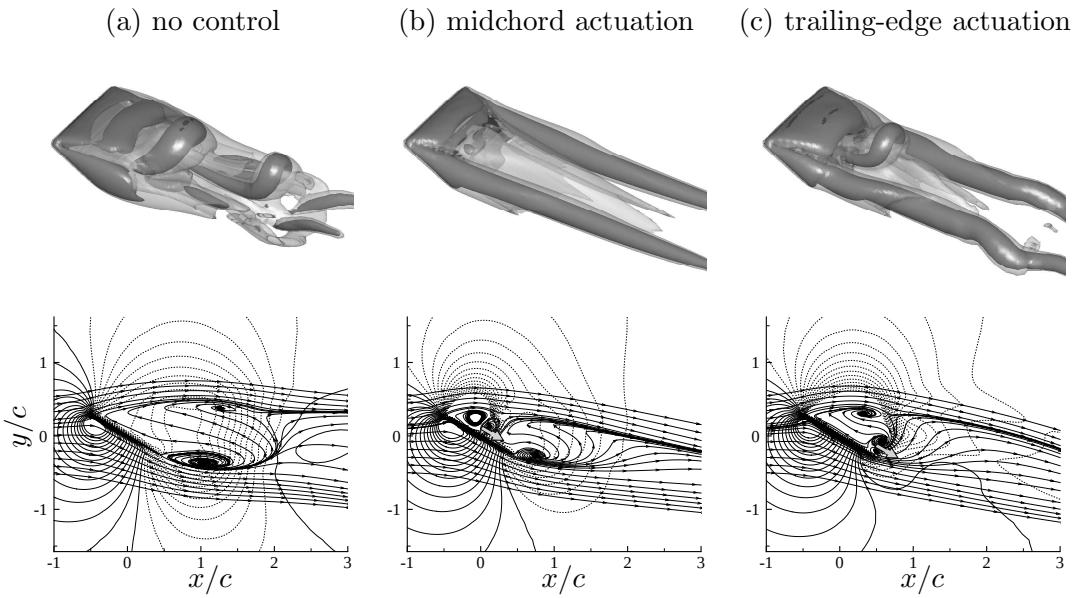

Figure 4.4: (Top) Snapshots of the large-time wake around a rectangular wing of $AR = 2$ at $\alpha = 30^\circ$ and $Re = 300$. (Bottom) Corresponding time-averaged pressure distribution and streamlines along the midspan. Pressure contour levels are set from -0.3 to 0.3 in increments of 0.04 with the negative pressure shown by the dashed lines. Arrows indicate the location of actuation.

of the leading- and trailing-edge vortices. For the two controlled cases, we observe that the most dominant flow features are the long columnar tip vortices formed by engulfing the vortex sheet from the trailing edge. The downstream blowing along the midchord allows for the flow around the wing to achieve a steady state as shown with its elongated wake vortices in Figure 4.4(b). The tip vortices exhibit clear columnar structures inducing downward-induced velocity onto the wake stabilizing the leading-edge vortex sheet. The vorticity within this sheet is diffused into the free stream in a steadfast manner at this Reynolds number. In the case of downstream blowing at the trailing edge, the strengthened tip vortices apply stronger downward-induced velocity on the leading-edge vortices and let them roll up in close neighborhood of the top surface of the plate as shown in Figure 4.4(c). Hence the low-pressure cores from the roll-up provide lift enhancement.

In both cases the separation bubble with control visualized along the midspan have become smaller in a time-averaged sense compared to the unactuated case. Additionally, the streamlines are deflected further downward with blowing, directly implying that lift on the wing is increased based on the momentum balance. Note that the roll-up motion at the trailing edge from the unactuated case is now attenuated with steady blowing. The removal of such roll-up seems to be the key factor in modifying the dynamics of the wake. On the other hand, the roll-up of the leading-edge vortex sheet occurs farther away from the wing making the flow less sensitive to the actuation at the leading edge.

To illustrate the lift enhancement mechanism, we present Figure 4.5 for the trailing-edge blowing but this figure also captures the flow physics for the case of midchord blowing. With downstream blowing, the trailing-edge vortex sheet is pushed further downward avoiding direct interaction with the vortical structure emanating from leading edge. As the trailing-edge vortex sheet advects downstream, it is rolled into the tip vortices which in turn strengthens the tip vortices. The increase in streamwise circulation results in stronger downward thrust of the fluid. Additionally, the stronger downward velocity induced by the tip vortices presses the leading-edge vortex and the corresponding low-pressure core

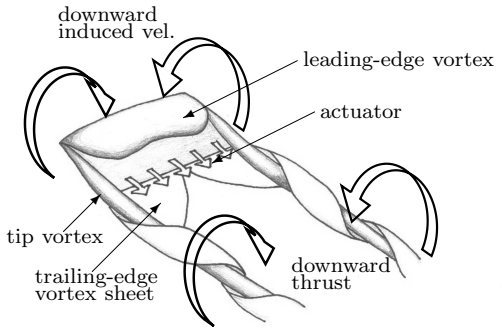

Figure 4.5: An illustration of tip vortices engulfing the trailing-edge vortex sheet with trailing-edge actuation.

region onto the top surface of the wing, enhancing lift. Hence, we suggest that the tip vortices can be used as effectively as the leading-edge vortices in applying vortical forces upon a body. While most of the past discussions in circulation control (Englar, 2000) and flapping-wing aerodynamics (Birch *et al.*, 2004) have focused on the spanwise circulation to explain the lift enhancements, streamwise circulation (tip vortices) can also contribute to lift with the current control setup. Traditionally, the tip effects are thought of as a nuisance due to the loss of the low-pressure region near the tips for attached flows at small angles of attack. However, we emphasize here that the tip vortices and their corresponding vortical forces can be used favorably to enhance lift in separated flows behind low-aspect-ratio wings.

4.2.5 Downstream blowing at the trailing edge

As we observed that steady downstream blowing applied at the trailing edge is very effective in increasing lift, applications of such actuation are further examined for a wide range of flow conditions at $Re = 300$. Momentum coefficients of $C_\mu = 0.51\%$ and 1.0% are applied to rectangular wings of $AR = 1$, 2, and 4 over a range of angles of attack. Various aspect ratios are considered for assessing the performance of the current controller and the increase in the strength of the tip vortices.

The time-averaged lift and lift-to-drag ratio at large time are summarized in Figure 4.6. We observe increase in lift and lift-to-drag ratio over a range of

angle of attack for both values of C_μ. Shown on the left are the time-averaged lift coefficients with actuation as well as the time-averaged and maximum lift coefficients without actuation. What is denoted as the maximum lift is achieved immediately following the impulsive start for the uncontrolled cases around $U_\infty t/c \approx 1.5$ (Figure 3.5). The difference between the average and maximum lift for the uncontrolled flow is attributed to the lift enhancement provided by the leading-edge vortex. Enhanced lift from steady blowing is now close to or larger than the maximum lift achieved immediately after the impulsive, start as well as the inviscid limit of lift for low-aspect-ratio airfoils derived by Helmbold (1942).

Let us examine the performance of the actuator for the wing of $AR = 1$. In Figure 4.6 we observe that the time-averaged lift with control is increased past the maximum lift achieved by the uncontrolled transient flow for almost all cases considered. Again, this increase is not from the addition of the numerical body force used to represent steady blowing. The direct contributions to lift from such modeled blowing are $0.1 \sin\alpha$ and $0.2 \sin\alpha$ for $C_\mu = 0.51\%$ and 1.0%, respectively, and do not account for the full increase realized here. The lift increase seen here results mostly from the modification of the wake vortices.

With flow control around a wing of $AR = 2$, the time-averaged lift is further increased especially around $\alpha \approx 20^\circ$. For higher α, the interaction of the wake vortices reduce the level of increase but still achieves an overall enhancement for both forcing magnitudes. A similar trend holds for the case of $AR = 4$ with peak performance around $\alpha \approx 20^\circ$, again. There are two effects contributing to the enhancement of lift, the downward thrust generated by the pair of tip vortices and the low-pressure region provided by the close roll-up of the leading-edge vortex. Here, for the higher-aspect-ratio wings, the two effects enhance lift more significantly than the case of $AR = 1$. In the case of $AR = 1$, the tip vortices cover the entire span without leaving much room for the leading-edge vortex to stay near the top surface. The lift-to-drag ratio does not show a large enhancement for $AR = 1$ when compared to the higher-aspect-ratio wings. To increase the lift-to-drag ratio, it seems important to have both the downward thrust from the tip

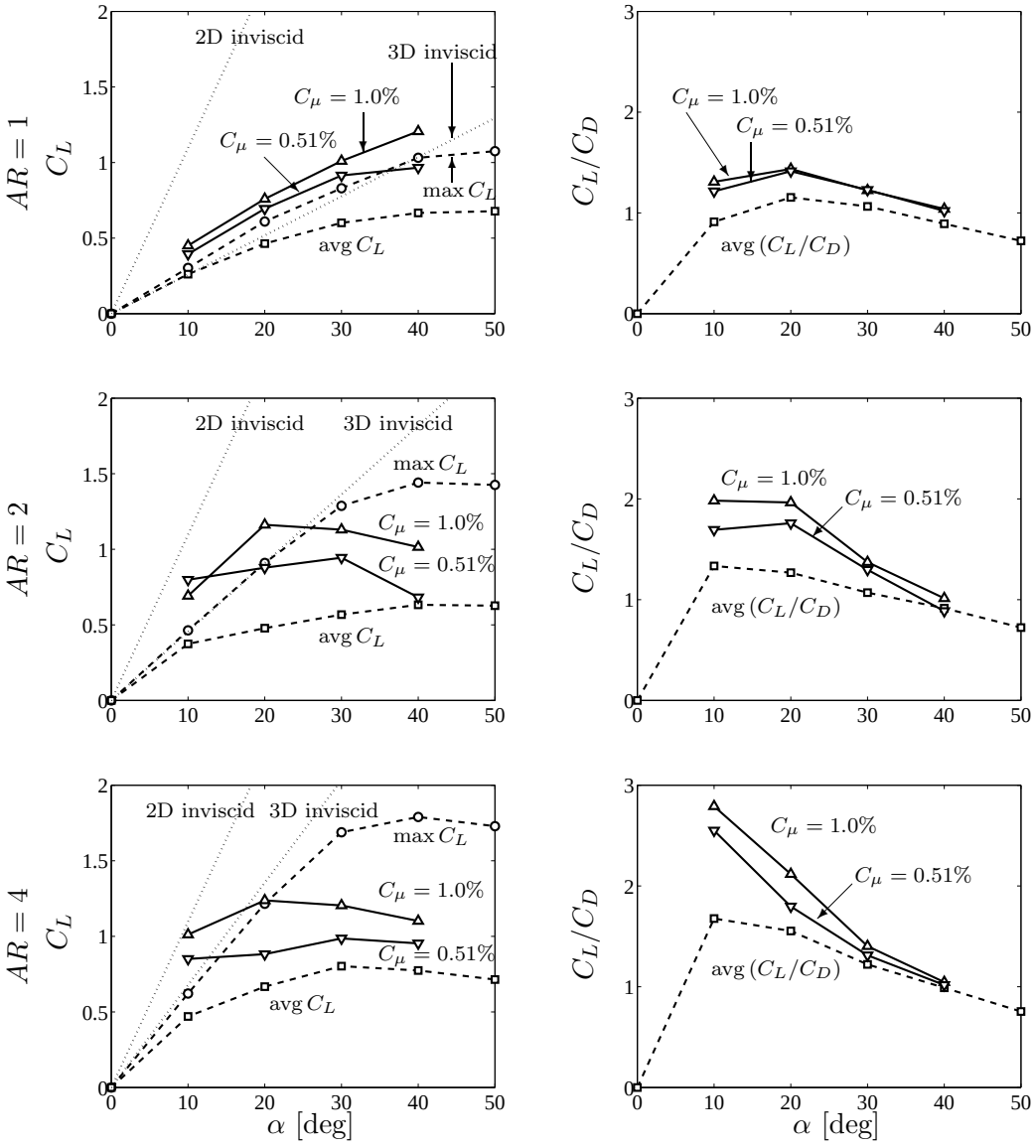

Figure 4.6: Time-averaged lift coefficients and lift-to-drag ratios for wings of $AR = 1$, 2, and 4 for cases without actuation (□) and with actuation for $C_\mu = 0.51\%$ (▽) and 1.0% (△). Shown also are the maximum lift for unactuated case (○) and the inviscid limits (·····).

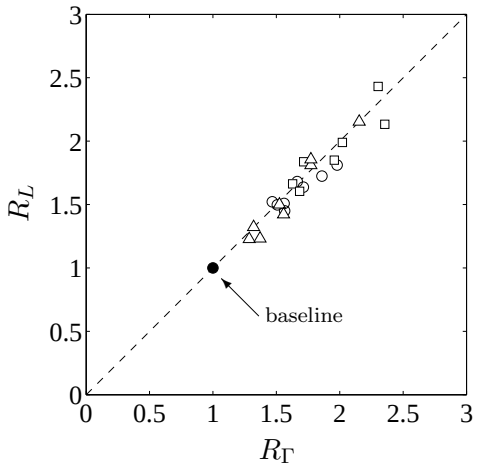

Figure 4.7: Normalized lift over normalized circulation of the tip vortex from control ($AR = 1$: $\square$, $AR = 2$: $\circ$, and $AR = 4$: $\triangle$).

vortices and the residence of the leading-edge vortices near the top surface.

In the case of larger aspect-ratio wings, there are benefits from both effects before the flow becomes overwhelmed with strong nonlinear interaction of the wake vortices at high angles of attack (i.e., $\alpha \approx 40°$). In such high-angle-of-attack flows, downward blowing is not able to keep the trailing-edge vortex sheet from interacting with other vortices and results in no significant increase in the strength of the tip vortices (unless perhaps with much stronger blowing). Nonetheless, this actuator setup seems to be effective overall for various cases of flow regimes (steady and unsteady periodic/aperiodic states as discussed in the uncontrolled flow section). The strip of steady blowing at the trailing edge is especially attractive for $AR \gtrsim 2$ and $\alpha \lesssim 30°$ as the lift-to-drag ratio shows substantial increase as well.

To demonstrate that the increase in lift is attributed to the strengthening of the tip vortices, we compute the relative increase in lift and streamwise circulation of the tip vortex:

$$R_L \equiv \operatorname{avg} C_L / \operatorname{avg} C_L^* \quad \text{and} \quad R_\Gamma \equiv \operatorname{avg} \Gamma / \operatorname{avg} \Gamma^*, \tag{4.3}$$

respectively, where $*$ is used here to denote the unactuated results. The circulation of the tip vortex is evaluated at a streamwise location of $x/c = 2.5$ using $\Gamma = \oint \mathbf{u} \cdot d\mathbf{l}$, where the contour is chosen to enclose the patch of vorticity (tip vortex) above 1% of the maximum value. These relative increases are plotted against each other in Figure 4.7 for actuated cases with $C_\mu = 0.51\%$ and 1.0% around wings of $AR = 1$, 2, and 4. Based on Figure 4.7, the correlation coefficient $\rho(R_\Gamma, R_L)$ is found to be 0.9515, which indeed suggests that strengthening the tip vortices have positive influence on the lift enhancement for low-aspect-ratio wings at post-stall angles of attack. With the current flow control arrangement, an increase in lift as high as about 2.5 times the unactuated value has been achieved for one case.

4.3 Summary

We considered the application of steady blowing to separated flows behind low-aspect-ratio rectangular wings at a low Reynolds number. The objective of the flow control was to enhance lift at post-stall angles of attack by changing the dynamics of the wake vortices and not by suppressing the unstable modes or reattaching the flow. Flow control was simulated with the immersed boundary projection method and the actuator was modeled by a body force near the top surface of the wing to represent steady blowing. Various setups were considered and the downstream blowing along the trailing edge was found to be most effective in enhancing lift. This controller strengthened the tip vortices by engulfing the trailing-edge vortex sheet to increase the downward thrust and the downward-induced velocity onto the leading-edge vortices. The low-pressure cores of the leading-edge vortices were moved closer to the top surface contributing to the increase in lift. In some ways, the present control mechanism is similar to circulation control (Englar, 2000). However, instead of increasing the spanwise circulation, we have increased the streamwise circulation of the tip vortices here. The tip vortices that are traditionally considered as an aerodynamic nuisance, have been used in favor to increase lift in post-stall flows for the considered low-aspect-ratio wings.

Chapter 5

Concluding Remarks

5.1 Conclusions

We presented a new formulation of the immersed boundary method that is algebraically identical to the traditional fractional step algorithm. This method, called the immersed boundary projection method, allows for the simulations of incompressible flows over arbitrarily shaped bodies under motion and/or deformation in both two and three dimensions. The no-slip condition along the immersed boundary is enforced simultaneously with the incompressibility constraint through a single projection. The boundary force is determined implicitly without any constitutive relations for the rigid body formulation, which in turn allows the use of high CFL numbers in our simulations compared to past methods. Results from simulations of two- and three-dimensional flow examples showed excellent agreement with previous experimental and numerical studies. Furthermore, an accelerated immersed boundary projection method that utilizes the Fast Fourier Transform and a multi-domain far field boundary conditions is presented in Appendix B.

The above immersed boundary projection method was used to analyze three-dimensional separated flows around low-aspect-ratio flat-plate wings at low Reynolds numbers. Both the initial transient and long time behavior of the flow

were studied by simulating an impulsively started wing in pure translation. The unsteady nature of the separated flow and vortex dynamics were highlighted.

A number of simulations were performed for $Re = 300$ and 500 with various aspect ratios, angles of attack, and planform geometries. The aspect ratio and angle of attack were found to have a large influence on the stability of the wake and the force experienced by the low-aspect-ratio wing. At early times, topologies of the wake vortices were found to be the same across different aspect ratios and angles of attack. Behind low-aspect-ratio rectangular plates, leading-edge vortices formed and eventually separated as hairpin vortices following the initial impulsive translation. This phenomenon was found to be similar to dynamic stall observed behind pitching plates. The detached structure would then interact with the tip vortices, reducing the downward velocity induced by the tip vortices acting upon the leading-edge vortex. At large time, depending on the aspect ratio and angles of attack, the wakes reached one of the three states: (*i*) a steady state, (*ii*) a periodic unsteady state, or (*iii*) an aperiodic unsteady state. The aperiodic unsteady state is found to be asymmetric in the spanwise direction and is caused by the strong interaction between the leading-edge, trailing-edge, and tip vortices.

Elliptic, semicircular, and delta wings were also considered. The wakes behind non-rectangular wings were observed to be different from the cases of rectangular planforms in terms of the shedding pattern (stability) and the influence of the tip vortices. However, the overall trend for the lift and drag histories were found to be similar to those of the rectangular case.

Three-dimensional separated flows behind low-aspect-ratio plates were found to be vastly different from the analogous two-dimensional flows. We have observed that the tip effects in three-dimensional flows can stabilize the flow and also exhibit nonlinear interaction with the shedding vortices. Even when the aspect ratio is increased to 4, the flow along the mid-span does not approach the two-dimensional von Kármán vortex shedding since spanwise cellular structures (stall cells) emerge. Asymmetric wakes about the mid-span were also observed for aperiodic flows around rectangular wings at high angles of attack. Furthermore, the tip vortices

and their interaction with the other wake vortices were significantly influenced by the planform geometry.

At last, we applied steady blowing to separated flows behind low-aspect-ratio rectangular wings at a low Reynolds number. The objective of the flow control was to enhance lift at post-stall angles of attack by changing the dynamics of the wake vortices. Various setups were considered and the downstream blowing along the trailing edge was found to be most effective in enhancing lift. This controller strengthened the tip vortices by engulfing the trailing-edge vortex sheet to increase the downward thrust and the downward-induced velocity onto the leading-edge vortices. The low-pressure cores of the leading-edge vortices were moved closer to the top surface, contributing to the increase in lift. The tip vortices that are traditionally considered as an aerodynamic nuisance, have been used favorably to increase lift in post-stall flows for the considered low-aspect-ratio wings.

5.2 Future directions

Here, we comment on the possible continuation of the research presented in this thesis.

First, there is room for improvement with the present immersed boundary projection method. The spatial accuracy for the two-dimensional problem considered (Chapter 2) with the current approach is $\mathcal{O}(\Delta x^{1.5})$ in the L_2 norm. It would be desirable to increase the accuracy to second order. Future research can consider alternative formulation of the interpolation (E) and regularization (H) operators, not based upon the discrete delta function used here but constructed using additional geometric information of the immersed boundary, such as the curvature. Furthermore, augmenting the discrete gradient (G) and divergence (D) operators with corrective terms to account for the pressure jump condition may be necessary, as considered by Lee & LeVeque (2003).

While the immersed boundary projection method described in Chapter 2 was only applied to stationary bodies in Chapters 3 and 4, flows around moving or

deforming bodies can also be investigated by the same method without difficulty. For example, vortex dynamics around a pitching plate and flapping wings can be simulated. Preliminary results for three-dimensional flows around such bodies are presented in Figures 5.1 and 5.2.

$U_\infty t/c = 0$	$U_\infty t/c = 10$	$U_\infty t/c = 15$	$U_\infty t/c = 20$
($\alpha = 0°$)	($\alpha = 18.9°$)	($\alpha = 29.3°$)	($\alpha = 30.0°$)
	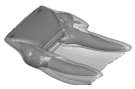	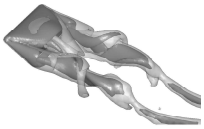	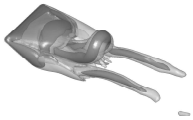

Figure 5.1: Snapshots of the wake evolution behind a rectangular flat plate of $AR = 2$ pitching from $\alpha = 0°$ to $30°$ at $Re = 300$. Isosurfaces of $\|\boldsymbol{\omega}\| = 3$ and $Q = 3$ are shown in gray and aquamarine, respectively. Viewing downward from the port side of the plate.

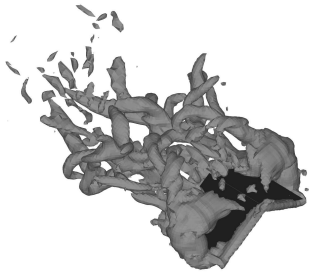

Figure 5.2: Snapshots of the wake evolution behind flat plates at $Re = 1000$. Isosurfaces of $Q = 3$ are shown in gray and aquamarine, respectively. Freestream flow is directed from bottom right to top left.

Fluid-structure interactions can also be combined with the immersed boundary methods. Some initial results with predictor-corrector coupling of the fluid and structural dynamics have shown promising results. In fact, such coupled simulations are currently performed to study particulate flows using an axisymmetric version of the immersed boundary projection method by Ms. Xiaobai

Li and Prof. Melany Hunt. Three-dimensional flows around flexible surfaces and flow-induced vibrations can be explored in the future for applications in small-scale vehicles and biological flows.

The steady flow control considered in Chapter 4 was exploratory as a first step in understanding the influence of actuation to the wake vortex dynamics. Ongoing investigations in feedback control applied to analogous two-dimensional flows by Joe *et al.* (2008) and Ahuja & Rowley (2008) can be extended to three-dimensional flows around low-aspect-ratio wings. The use of their adjoint analysis will be useful in identifying effective actuator placement. Of course, similar control studies can be performed on flows around non-rectangular wings, such as semicircular or delta-shaped planforms. Furthermore, demonstrating the robustness of the feedback controller will prove useful for the implementation of the controller on an actual micro air vehicle that operates under constant perturbations.

We hope that the immersed boundary projection method developed here will be useful for future endeavors in studying three-dimensional incompressible flows over various bodies. In addition, it is hoped that the analyses of the three-dimensional low-Reynolds-number flows around low-aspect-ratio wings have shed light on the importance of three-dimensionality in vortex dynamics.

Appendix A

Discretization of the Immersed Boundary Projection Method

This appendix describes the details on how the incompressible Navier-Stokes equations Eqs. (2.10) to (2.12) are discretized on a finite-volume staggered mesh to reach the form of Eq. (2.13). A two-dimensional case is presented, although an extension to three dimensions is straightforward. Here, the underlying spatial discretization is taken to be a non-uniform Cartesian staggered mesh (x_i, y_j) with the immersed surface represented by a set of Lagrangian points (ξ_k, η_k), as shown previously in Figure 2.1. Readers can also consult the works of Perot (1993) and Chang *et al.* (2002) for details on the fractional step method for staggered grid formulation.

The incompressible Navier-Stokes equations with a boundary forcing function, Eqs. (2.10) to (2.12), can be discretized with the second-order Adam–Bashforth and Crank–Nicolson methods for the convective and viscous terms, respectively:

$$\frac{u^{n+1}-u^n}{\Delta t} + \frac{3}{2}\hat{N}(u^n) - \frac{1}{2}\hat{N}(u^{n-1}) = -\hat{G}p + \frac{1}{2}\hat{L}\left(u^{n+1}+u^n\right) + \widehat{bc}_1 + \hat{H}f, \quad \text{(A.1)}$$

$$\hat{D}u^{n+1} = bc_2, \quad \text{(A.2)}$$

$$\hat{E}u^{n+1} = u_B^{n+1}, \quad \text{(A.3)}$$

Operator	Discrete	Continuous
Divergence	$\hat{D}$	$\nabla \cdot (\ )$
Gradient	$\hat{G}$	$\nabla(\ )$
Interpolation	$\hat{E}u^n$	$\int_{\mathbf{x}} \mathbf{u}(t^n)(\mathbf{x})\delta(\mathbf{x}-\boldsymbol{\xi})d\mathbf{x}$
Regularization	$\hat{H}f$	$\int_s \mathbf{f}(\boldsymbol{\xi}(s,t))\delta(\boldsymbol{\xi}-\mathbf{x})ds$
Laplacian	$\hat{L}$	$Re^{-1}\nabla^2(\ )$
Convection	$\hat{N}(u^n)$	$\nabla \cdot (\mathbf{u}(t^n)\mathbf{u}(t^n))$

Table A.1: Nomenclature of the discrete operators and their continuous analogs.

where u^{n+1}, p, and f are the discrete velocity, pressure, and boundary force. We order the discrete velocity and force vectors, $(u,v)^T$ and $(f_x,f_y)^T$, respectively. The spatial operators introduced above are listed side-by-side with their continuous analog in Table A.1. The discrete Laplacian and divergence operators generate inhomogeneous terms $\widehat{bc}_1$ and bc_2 resulting from the boundary conditions along $\partial\mathcal{D}$. Note that $\widehat{bc}_1$ depends on time levels n and $n+1$ (for CN method). For Eq. (A.2), bc_2 is a function of time level $n+1$. Details on $\hat{E}$ and $\hat{H}$ are provided in Section 2.3.2. If $\partial\mathcal{B}$ moves with velocity u_B^{n+1} over $\mathcal{D}$, operator $\hat{E}$ or more precisely the Lagrangian points are functions of time level $n+1$. As stated in Perot (1993), a staggered grid formulation with velocity boundary conditions requires no pressure boundary condition. Operators and vectors with hats are later transformed with a diagonal matrices for scaling purposes.

Collecting the unknowns on the left-hand side, Eqs. (A.1) to (A.3) can be written as

$$\begin{bmatrix} \hat{A} & \hat{G} & -\hat{H} \\ \hat{D} & 0 & 0 \\ \hat{E} & 0 & 0 \end{bmatrix} \begin{pmatrix} u^{n+1} \\ p \\ f \end{pmatrix} = \begin{pmatrix} \hat{r}^n \\ 0 \\ u_B^{n+1} \end{pmatrix} + \begin{pmatrix} \widehat{bc}_1 \\ bc_2 \\ 0 \end{pmatrix}, \tag{A.4}$$

where

$$\hat{A} \equiv \frac{1}{\Delta t} I - \frac{1}{2}\hat{L} \quad \text{and} \quad \hat{r}^n \equiv \left[\frac{1}{\Delta t} I + \frac{1}{2}\hat{L}\right] u^n - \frac{3}{2}\hat{N}(u^n) + \frac{1}{2}\hat{N}(u^{n-1}). \tag{A.5}$$

Although we omit the details, $\hat{A}$ can be made symmetric and positive-definite quite easily.

In order to solve the above system efficiently, symmetry among the sub-matrices are desired. First, let us make the gradient and divergence operators a transpose of each other by a simple transformation. Both operators can be scaled appropriately so that the entries consist solely of ± 1 by introducing R and $\hat{M}$:

$$R \equiv \begin{bmatrix} \Delta y_j & 0 \\ 0 & \Delta x_i \end{bmatrix} \quad \text{and} \quad \hat{M} \equiv \begin{bmatrix} \frac{1}{2}(\Delta x_i + \Delta x_{i-1}) & 0 \\ 0 & \frac{1}{2}(\Delta y_j + \Delta y_{j-1}) \end{bmatrix}, \tag{A.6}$$

where the nonzero sub-matrices are diagonal. For details on the construction of $\hat{G}$ and $\hat{D}$, refer to Chang *et al.* (2002). As a result $\hat{D}R^{-1} = -(\hat{M}\hat{G})^T$. Note that R transforms velocity u^{n+1} to velocity flux $q^{n+1} \equiv Ru^{n+1}$. Using these transforms in Eq. (A.4), we find

$$\begin{bmatrix} A & G & -\hat{M}\hat{H} \\ D & 0 & 0 \\ \hat{E}R^{-1} & 0 & 0 \end{bmatrix} \begin{pmatrix} q^{n+1} \\ p \\ f \end{pmatrix} = \begin{pmatrix} r^n \\ 0 \\ u_B^{n+1} \end{pmatrix} + \begin{pmatrix} bc_1 \\ bc_2 \\ 0 \end{pmatrix}, \tag{A.7}$$

where

$$A \equiv \hat{M}\hat{A}R^{-1}, \quad G \equiv \hat{M}\hat{G}, \quad D \equiv \hat{D}R^{-1} = -G^T, \quad r^n \equiv \hat{M}\hat{r}^n, \quad bc_1 \equiv \hat{M}\widehat{bc}_1. \tag{A.8}$$

Also, for ease of discussion in Sections 2.2 and 2.3, we define the mass matrix and the transformed Laplacian by $M \equiv \hat{M}R^{-1}$ and $L \equiv \hat{M}\hat{L}R^{-1}$ such that $A = \frac{1}{\Delta t}M - \frac{1}{2}L$. We note that A is symmetric and positive-definite by construction.

All steps presented up to this point in this Appendix are for the fractional step method and nothing special has been performed for the immersed boundary

portion of our formulation. We recover Eq. (2.3) if we remove f and the no-slip constraint from Eq. (A.7).

Finally, we re-define the interpolation and regularization operators by combining the diagonal matrices, R and $\hat{M}$:

$$E \equiv \hat{E}R^{-1} \quad \text{and} \quad H \equiv \hat{M}\hat{H}. \tag{A.9}$$

Combining Eqs. (A.7) and (A.9), we obtain Eq. (2.13):

$$\begin{bmatrix} A & G & -H \\ D & 0 & 0 \\ E & 0 & 0 \end{bmatrix} \begin{pmatrix} q^{n+1} \\ p \\ f \end{pmatrix} = \begin{pmatrix} r^n \\ 0 \\ u_B^{n+1} \end{pmatrix} + \begin{pmatrix} bc_1 \\ bc_2 \\ 0 \end{pmatrix}, \tag{A.10}$$

Before closing, we note again that $G = -D^T$ and $A = A^T$ by construction.

Appendix B

The Fast Immersed Boundary Projection Method

In incompressible flow simulations, solving the pressure Poisson equation is the largest computational burden, due to large condition number the discrete Poisson equation possesses. Hence, we consider the use of a nullspace approach that eliminates the need to solve such an elliptic equation. In this appendix, we describe the implementation of a nullspace/discrete streamfunction method (Hall, 1985; Chang *et al.*, 2002) that allows the divergence-free constraint to be analytically satisfied. Additionally, a far-field boundary condition/multi-domain solution compatible with the current nullspace approach is presented.

B.1 Nullspace approach

The *nullspace* or *discrete streamfunction* approach (Hall, 1985; Chang *et al.*, 2002) is a method for solving the system (2.13) without the immersed boundary formulation. In this case, the flow only needs to satisfy the incompressibility constraint, which leads us to the use of discrete streamfunction, s, such that

$$q = Cs, \tag{B.1}$$

where C represents the discrete curl operator. This operator is constructed with column vectors corresponding to the basis of the nullspace of D. Chang *et al.* (2002) should be consulted for details. Hence, these operators enjoy the following relation

$$DC \equiv 0, \tag{B.2}$$

which automatically enforces incompressibility at all time; $Dq^{n+1} = DCs^{n+1} = 0$. This discrete relation is consistent with the continuous version of the vector identity: $\nabla \cdot \nabla \times \equiv 0$.[1]

Pre-multiplying the momentum equation in Eq. (2.13) with C^T, the pressure gradient term can also be removed from the formulation since $C^T Gp = -(DC)^T p = 0$, resulting in only a single equation to be solved for each time step:

$$C^T ACs^{n+1} = C^T r_1^n. \tag{B.3}$$

In this method, the most computationally expensive component of the fractional step method, namely the pressure Poisson solver, is eliminated while the continuity equation is exactly satisfied. Moreover the fractional-step error arising from using an approximate A^{-1} is not present since an approximate LU decomposition is not required. This feature led Chang *et al.* (2002) to call this technique the *exact fractional step method*.

We note that the operator C^T is another discrete curl operation, and that:

$$\gamma = C^T q, \tag{B.4}$$

is a second-order-accurate approximation to the circulation in each dual cell (vorticity multiplied by the cell area normal to the vorticity component).

This method may in general be used on unstructured staggered meshes in two

[1]Note that we have set $bc_2 = 0$ in Eq. (2.13), which is the case for the boundary conditions we consider here. More general situations that require $bc_2 \neq 0$ can be handled by solving an appropriate Poisson equation (once and for all) for the given inhomogeneous vector and adding the solution to Eq. (B.1).

and three dimensions (Chang *et al.*, 2002), including, as a special case, the simple Cartesian mesh used in the immersed boundary methods. In two dimensions, the discrete streamfunction and circulation have a single component (in the direction normal to the plane), which is naturally defined at the cell *vertices* (see Figure B.1). In three dimensions there are three components of the streamfunction and circulation that are defined at the centers of the edges of the Voronoi (dual) cell, analogously to the velocity components on the primal mesh.

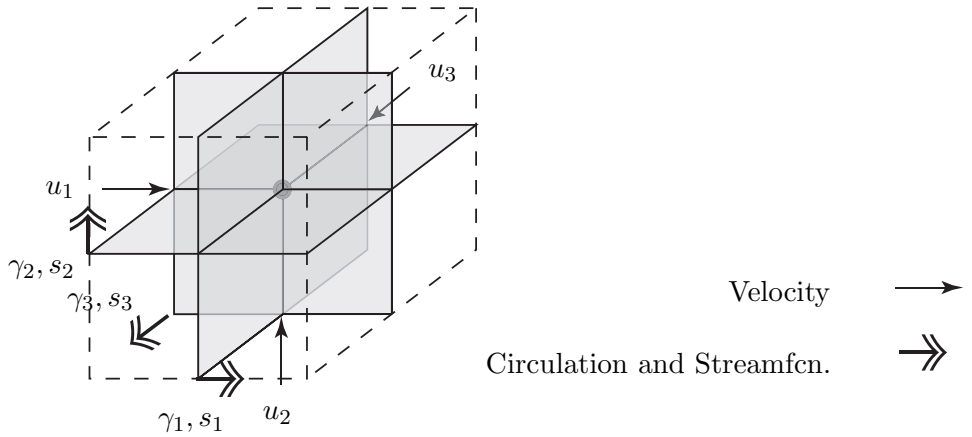

Figure B.1: Location of variables on staggered three-dimensional mesh. Velocity components are defined at the center of each edge. Streamfunction and circulation are defined similarly for the Voronoi cell.

B.2 Nullspace approach with an immersed boundary

In order to satisfy both the incompressibility and the no-slip conditions with the nullspace technique, it would be necessary to derive a basis for the nullspace of $Q^T = [G\ E^T]^T$. Although a singular value decomposition of Q^T can be performed to numerically determine the nullspace, the result is not in general a sparse representation, which is a necessity for computational feasibility. An analytical derivation of the nullspace operator does not seem to be an easy task

either. Moreover, in the general case where the body is moving, the nullspace representation would need to be recomputed at least once per timestep.

To circumvent this difficulty, we once again could rely on a projection approach. Consider the system that is obtained by incorporating C^T and $q^{n+1} = Cs^{n+1}$ to Eq. (2.21). The incompressibility constraint and the pressure variable are eliminated and we arrive at another KTT system:

$$\begin{bmatrix} C^T AC & C^T E^T \\ EC & 0 \end{bmatrix} \begin{pmatrix} s^{n+1} \\ \tilde{f} \end{pmatrix} = \begin{pmatrix} C^T r_1^n \\ u_B^{n+1} \end{pmatrix}. \tag{B.5}$$

The left-hand-side matrix is symmetric but in general indefinite, making a direct solution less efficient. The projection (fractional step) approach similar to Eqs. (2.25) to (2.27) would result in

$$C^T ACs^* = C^T r_1^n, \tag{B.6}$$

$$EC\left(C^T AC\right)^{-1}(EC)^T \tilde{f} = ECs^* - u_B^{n+1}, \tag{B.7}$$

$$s^{n+1} = s^* - \left(C^T AC\right)^{-1}(EC)^T \tilde{f}, \tag{B.8}$$

where we have as not yet inserted an approximation for the inverse of $C^T AC$. Direct solution of this system in the general case requires a nested iteration to solve the modified Poisson equation. This may be feasible in general (a rough operation count indicates that the work is similar to Eqs. (2.25) to (2.27)). In the case where the body is not moving, it is moreover possible to perform a Cholesky decomposition of $EC\left(C^T AC\right)^{-1}(EC)^T$ once and for all, since the dimension of the system scales with the number of Lagrangian points representing the immersed boundary. In this case, a system of equations of the form $C^T ACx = b$ need be solved once for each boundary force at the beginning of the computation.

B.3 Fast method for uniform grid and simple boundary conditions

Instead of persuing the projection approach outlined in Eqs. (B.6) to (B.8), let us return to the spatially discretized moment equation

$$M\frac{dq}{dt} + Gp + E^T\tilde{f} = \mathcal{N}(q) + Lq + bc_1, \tag{B.9}$$

along with the divergence-free and no-slip constraints. Next, let us consider solving the flow field with a uniform grid in all directions. We set the boundary conditions to be Dirichlet and Neumann for the normal and tangential velocities, respectively, for reasons that will be clear below. At the moment, we will focus on solving Eq. (B.9) efficiently.

Now, consider premultiplying Eq. (B.9) with C^T and change the unknown variable to $\gamma = C^T q$:

$$\frac{d\gamma}{dt} + C^T E^T\tilde{f} = -\beta C^T C\gamma + C^T\mathcal{N}(q) + bc_\gamma, \tag{B.10}$$

where we have used the relation $L = -\beta CC^T = -1/(Re\Delta x^2)CC^T$. Here C^TC is the discrete Laplacian for γ, which can be transformed into a diagonal matrix, Λ, using the discrete sine transform, S:

$$C^TC = S\Lambda S, \tag{B.11}$$

where $S^{-1} = S$ and the eigenvalues of C^TC in Λ are known (Press *et al.*, 1992). Applying the Crank-Nicolson and second-order Adam–Bashforth methods on the viscous and advective terms, respectively, Eq. (B.10) can be written as

$$\begin{aligned} S\left[I + \frac{\beta\Delta t}{2}\Lambda\right]S\gamma^{n+1} = &\left[I - \frac{\beta\Delta t}{2}C^TC\right]\gamma^n \\ &- \Delta tC^TE^T\tilde{f} + \frac{\Delta t}{2}\left[3\mathcal{N}(q^n) - \mathcal{N}(q^{n-1})\right] + \Delta tbc_\gamma. \end{aligned} \tag{B.12}$$

We now follow the fractional-step algorithm discussed in Section 2.2 for the above equation along with the no-slip condition, to obtain the following three-step system:

$$S\left[I+\frac{\beta\Delta t}{2}\Lambda\right]S\gamma^{*}=\left[I-\frac{\beta\Delta t}{2}C^{T}C\right]\gamma^{n} + \frac{\Delta t}{2}\left[3\mathcal{N}(q^{n})-\mathcal{N}(q^{n-1})\right]+\Delta t bc_{\gamma}, \quad \text{(B.13)}$$

$$EC\left[S\Lambda^{-1}\left(I+\frac{\beta\Delta t}{2}\Lambda\right)^{-1}S\right](EC)^{T}\tilde{f}=ECS\Lambda^{-1}S\gamma^{*}-u_{B}^{n+1}, \quad \text{(B.14)}$$

$$\gamma^{n+1}=\gamma^{*}-S\left[I+\frac{\beta\Delta t}{2}\Lambda\right]^{-1}S(EC)^{T}\tilde{f}. \quad \text{(B.15)}$$

The overall system becomes complete with a velocity solver

$$q^{n+1}=Cs^{n}+bc_{q}, \quad s^{n+1}=S\Lambda^{-1}S\gamma^{n}+bc_{s}, \quad \text{(B.16)}$$

where variables bc denote the appropriate boundary condition vectors indicated by the subscripts. The use of discrete streamfunction here guarantees that the velocity field is solenoidal.

The system of equations, Eq. (B.13) to (B.15), solves for the flow field in an efficient manner compared to the original immersed boundary projection method. First, the inversion of the left-hand-side matrix in Eq. (B.13) can now be performed algebraically; i.e., the inverse is simply $S(I+\frac{\beta\Delta t}{2}\Lambda)^{-1}S$. Second, the equation for the boundary force, $\tilde{f}$, is significantly smaller in size compared to the pressure Poisson equation for the discrete pressure. The dimension of the coefficient matrix is $n_B \times n_B$ and can be pre-decomposed (and stored) with a Cholesky decomposition since the matrix is symmetric and positive definite. This decomposition would be required only once at the beginning of the simulation for a stationary body. In the case of moving Lagrangian points, one can still use the conjugate gradient method.

Hence, we observe that significant speed-up can be achieved for the immersed boundary method with the use of uniform grid and simple boundary conditions.

However such boundary conditions would influence the flow field and necessitate a remedy to allow accurate simulations of flow over an immersed body in free-space. A solution to this problem is offered in the next section.

B.4 Far-field boundary conditions: a multi-domain approach

In the above section, we presented a technique to eliminate the pressure Poisson equation from the overall immersed boundary method with the assumption that the spatial domain is discretized with a uniform grid and the boundary conditions are simply Dirichlet and Neumann for the normal and tangential velocities, respectively. These assumptions restrict the entire computational domain to be discretized with a constant grid size even for the regions away from the body[2]. Hence the overall computational domain can be constrained in size and the corresponding flow field can suffer from a *blockage-like* effect with the use of the simple boundary conditions. Incompressible flows induced by the existence of bodies and vortices (of non-zero circulation) only decay algebraically in free space. Therefore, we need a corrective procedure to account for such decay of velocity profile by providing correct boundary conditions.

In order to obtain accurate boundary conditions for the velocities, we consider a multi-domain approach. In contrast to the commonly used multi-grid method used to zoom into fine flow structures, the multi-domain method here is employed to zoom out of the domain to determine accurate boundary conditions for the original computational domain. Thus, we coarsen the vorticity field onto increasingly large domains up to the N_g-th domain, denoted by $\mathcal{D}^{(1)}$, $\mathcal{D}^{(2)}$, $\cdots$,$\mathcal{D}^{(N_g)}$. An illustration of this process is shown on the top part of Figure B.2. For the largest domain, the simple boundary conditions of no-vorticity and no-stress are applied and the corresponding streamfunction is solved for through the pressure Poisson equation,

[2]It is possible to use Fourier transform even for a non-uniform grid to simulate an infinite domain for a certain choice of grid stretching (Cain *et al.*, 1984).

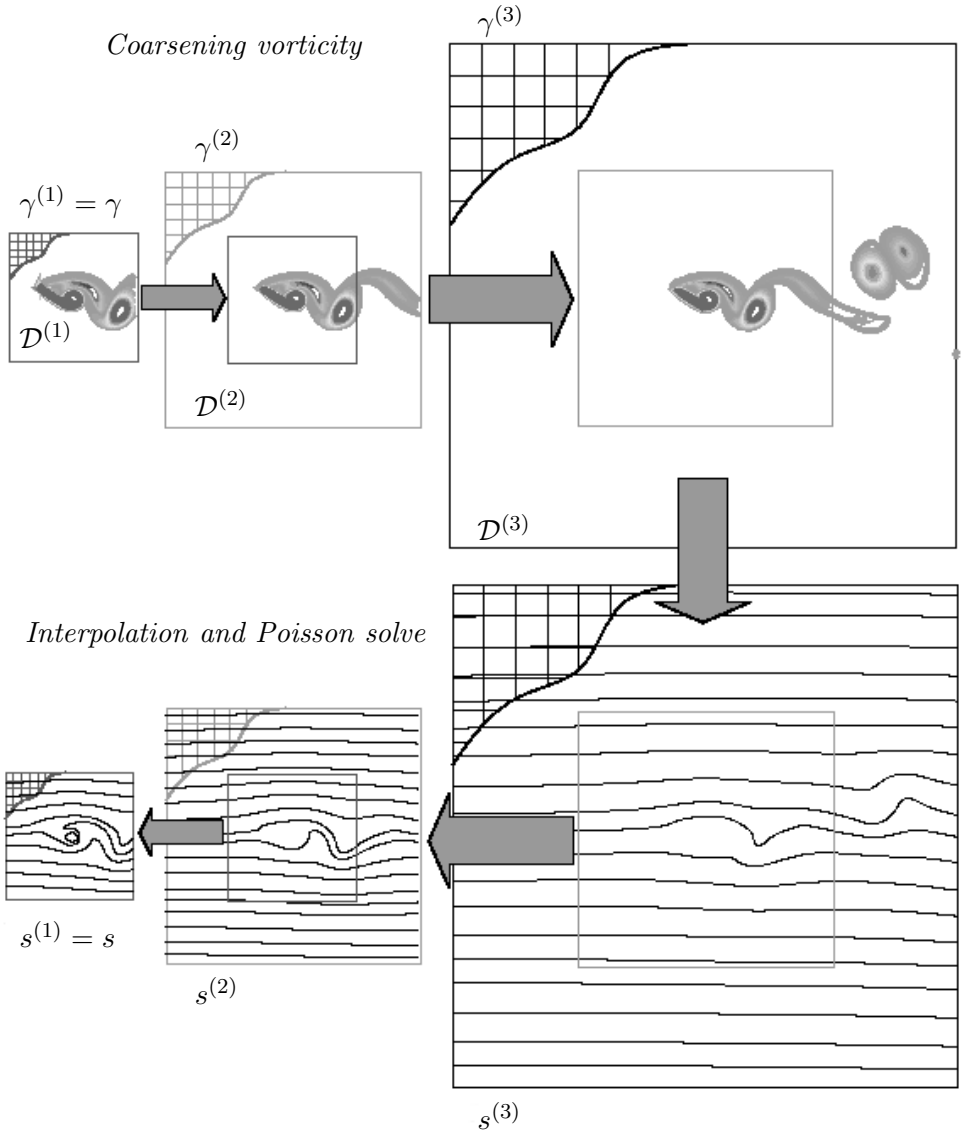

Figure B.2: Schematic of 3-level multi-domain solution of the Poisson equation.

$s^{n+1} = S\Lambda^{-1}S\gamma^n$.

With the streamfunction for the largest domain $\mathcal{D}^{(N_g)}$, its values are then interpolated onto the boundaries of the next inner domain $\mathcal{D}^{(N_g-1)}$. With this improved boundary condition, the streamfunction on $\mathcal{D}^{(N_g-1)}$ is solved and the interpolation of this solution is performed to yield the boundary condition for the next smaller domain. This process is continued until it reaches $\mathcal{D}^{(1)}$, as shown on the bottom part of Figure B.2.

This overall procedure can be summarized symbolically by the inversion of the Laplacian as:

$$s = S\overline{\Lambda^{-1}}S\gamma, \tag{B.17}$$

where $\tilde{s}$ is the streamfunction solution and $\tilde{\gamma}$ is the circulation for each grid ($\gamma_{i,j} = \omega_{i,j}\Delta x\Delta y$). The multi-domain operations are denoted with the operator $\overline{\Lambda^{-1}}$. The coarsening and interpolating operations, Eq. (B.17), can be expanded in the following manner:

$$\begin{aligned}
\gamma^{(1)} &= \gamma, \\
\gamma^{(k)} &= \begin{cases} \gamma^{(k)} & \text{where } x \in \mathcal{D}^{(k)} \setminus \mathcal{D}^{(k-1)}, \\ P^{(k-1)\to(k)}\left(\gamma^{(k-1)}\right) & \text{where } x \in \mathcal{D}^{(k-1)}, \end{cases} \\
& \qquad\qquad k = 2, 3, \cdots, N_g, \\
s^{(N_g+1)} &= 0, \\
s^{(k)} &= S\Lambda^{-1}S\gamma^{(k)} + bc_s\left[P^{(k+1)\to(k)}\left(s^{(k+1)}\right)\right], \\
& \qquad\qquad k = N_g, N_g-1, \cdots, 1, \\
s &= S\overline{\Lambda^{-1}}S\gamma = s^{(1)}\ .
\end{aligned}$$

Here $P^{(k-1)\to(k)}$ is a fine-to-coarse interpolation operator and $P^{(k)\to(k-1)}$ is its coarse-to-fine counterpart restricted to $\partial\mathcal{D}^{(k-1)}$ by bc_s. Without the loss of generality the streamfunction outside of the largest multi-domain is set to $\tilde{s}^{(N_g+1)} = 0$. However it can be specified accordingly for the problem of interest (i.e., uniform flow, potential flow, etc, ...).

The coarsening operation is considered to double the grid size Δx for each increasing grid level, and correspondingly quadruple the cell area size (eightfold in terms of cell volume for the three-dimensional case). In general, the coarsening operation can be performed for any factor of enlargement. In order to keep this multi-domain approach compatible with the sine transform and to reuse the same operators (with different constant factors to account for the different grid resolution), the grid for the larger domains is kept uniform as well. The interpolation operator can be made to any desirable accuracy, which in this case is set to second order. The coarsening should be performed to preserve circulation, such that spuriously generated circulation does not induce slowing decaying erroneous flow over space.

We note that the simple boundary conditions are also used for the outflow boundary at the largest multi-domain level. While the exiting perturbation will leave a reflective signature, the largest boundary is assumed to have (or should have) been made large enough so that the flow field in the inner domain is not significantly affected. For further discussion on the outflow boundary conditions, we refer readers to Appendix C.

In summary, with this multi-domain approach to account for the far-field boundary conditions, the fast method can be reformulated as:

$$S\left[I+\frac{\beta\Delta t}{2}\Lambda\right]S\gamma^{(k)*}=\left[I+\frac{\beta\Delta t}{2}C^TC\right]\gamma^{(k)^n}+\frac{\Delta t}{2}C^T\left[3\mathcal{N}(q^{(k)^n})-\mathcal{N}(q^{(k)^{n-1}})\right]+\frac{\Delta t}{2}bc_\gamma\left[P^{(k+1)\to(k)}\left(\gamma^{(k+1)^*}\right)+P^{(k+1)\to(k)}\left(\gamma^{(k+1)^n}\right)\right] \tag{B.18}$$

$$EC\left[S\overline{\Lambda^{-1}}\left(I+\frac{\beta\Delta t}{2}\Lambda\right)^{-1}S\right](EC)^T\tilde{f}=ECS\overline{\Lambda^{-1}}S\gamma^{(1)^*}-u_B^{n+1}, \tag{B.19}$$

$$\gamma^{n+1}=\gamma^{(1)^*}-S\left[I+\frac{\beta\Delta t}{2}\Lambda\right]^{-1}S(EC)^T\tilde{f}, \tag{B.20}$$

$$s^{n+1}=S\overline{\Lambda^{-1}}S\gamma^{n+1}. \tag{B.21}$$

The added computations by the use of the multi-domain approach increase linearly with larger N_g. However, the overall speed-up achieved by Eqs. (B.18) to (B.21) is still quite remarkable compared to the original immersed boundary projection method. In the following sections, we provide two numerical examples to assess the accuracy of the far-field boundary conditions, as well as the speed-up obtained from the fast method. In order to provide only the essential outline of this fast method, some level of details have been left out of this appendix. Readers are asked to refer to Colonius & Taira (2008) for further information.

B.5 Results

In this section, we present two problems that verify and validate the fast immersed boundary projection method and the use of the multi grid presented above. First, the potential flow over a cylinder is considered to verify the performance of the multi-grid approach. The second problem of viscous flow over a cylinder verifies the overall immersed boundary method and also evaluates the speed-up achieved by the fast method in comparison to the original immersed boundary projection method.

B.5.1 Potential flow over a cylinder

As an example, we consider the potential flow induced at $t = 0^+$ by an impulsively started cylinder of diameter D. The cylinder is represented by 571 equally spaced Lagrangian points and the domain is defined snugly around the body, extending to $\pm 0.55D$ in each direction with a grid spacing $\Delta x/D = 0.0055$. We initiate a uniform flow with speed U_∞ and let the body materialize at $t = 0$. The solution is obtained by performing 1 time-step of the Navier-Stokes solution using the fast method with the multi-domain boundary conditions. A flow field obtained with $N_g = 4$ is presented with the exact potential flow solution in Figure B.3. The streamlines are found to be in agreement with a slight difference near the immersed boundary due to the regularized nature of the discrete delta function. In

Figure B.4, we compare the exact potential flow solution to the numerical solution along the top boundary of the innermost domain for different N_g. We observe the estimated $\mathcal{O}(4^{-N_g})$ convergence[3] down to a level of about 10^{-3}, after which the leading-order error is dominated by the truncation error arising from the discrete delta functions at the immersed boundary and the discretization of the Poisson equation.

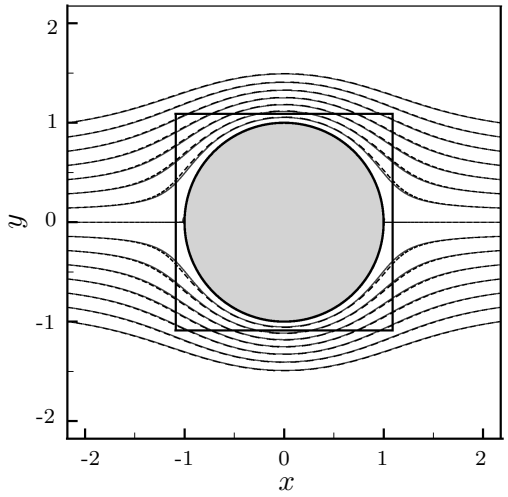

Figure B.3: Streamlines around a circular cylinder for potential flow for $N_g = 4$ with solutions from the first two inner multi domains shown. Present result (——) and the exact solution (----) are presented.

B.5.2 Performance of the fast method

Next, we measure the performance of the fast nullspace/multi-domain immersed boundary method compared to the original performance by the immersed boundary projection method. Simulated flows over a stationary circular cylinder of diameter D are compared to results in Tables 2.2 and 2.3. Computations are performed on the domain $\mathcal{D}^{(1)} = [-1, 3] \times [-2, 2]$ with $\Delta x/D = 0.02$ where N_g is

[3]This error estimate can be obtained by comparing the potential flow around a cylinder in free space and the potential flow around a doubly periodic array of cylinders. For a detailed derivation, see Colonius & Taira (2008).

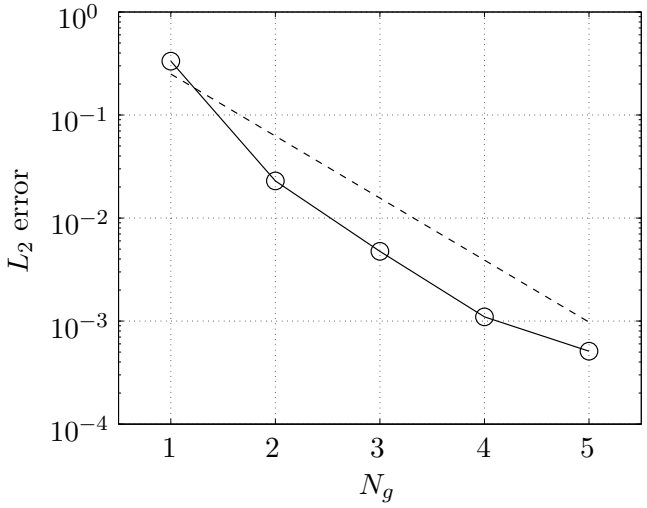

Figure B.4: Velocity error along the top boundary of the smallest domain for different N_g (∘). A guide of 4^{-N_g} is also shown (----).

varied between 1 and 5. A stationary circular cylinder is centered at the origin with the flow impulsively starting at $t = 0$. Since the Lagrangian points to not move, the Cholesky decomposition is used to solve Eq. (B.19).

After transient effects associated with the impulsively started flow have died away, we examine wake structures and forces on the cylinders for different values of N_g. These results are summarized in Tables B.1 and B.2, respectively, for $Re = 40$ and 200. For the steady flow at $Re = 40$, we report the characteristic dimensions of the recirculation bubble in the wake, and for the unsteady flow at $Re = 200$, we report the shedding frequency and the fluctuating lift and drag coefficients. Characteristic dimensions of the wake were illustrated and defined in Figure 2.6. It is evident that as N_g is increased, the fast method gives nearly identical results to the previously published data. It appears that $N_g = 4$ is sufficient to recover the previous results. Note that for the original immersed boundary projection method, computations are performed over a domain of $[-30, 30] \times [-30, 30]$ by 300×300 stretched grid points with the finest resolution of $\Delta x/D = \Delta y/D = 0.02$. The time steps for all cases are chosen to be $\Delta t = 0.01$ to limit the maximum Courant number to 1.

	l/d	a/d	b/d	θ	C_D	Speed-up
Present ($N_g = 2$)	1.69	0.60	0.55	53.4°	1.92	25.8
Present ($N_g = 3$)	2.01	0.67	0.58	54.0°	1.68	18.5
Present ($N_g = 4$)	2.17	0.70	0.59	53.8°	1.58	14.2
Present ($N_g = 5$)	2.20	0.70	0.59	53.5°	1.55	11.3
Linnick & Fasel (2005)	2.28	0.72	0.60	53.6°	1.54	-
Taira & Colonius (2007)	2.30	0.73	0.60	53.7°	1.54	1

Table B.1: Comparison of results from the fast-method with previously reported values for steady-state flow around a cylinder at $Re = 40$.

	St	C_D	C_L	Speed-up
Present ($N_g = 2$)	0.206	1.47±0.049	±0.66	121.1
Present ($N_g = 3$)	0.200	1.40±0.052	±0.70	84.7
Present ($N_g = 4$)	0.197	1.36±0.046	±0.70	65.4
Present ($N_g = 5$)	0.195	1.34±0.045	±0.68	53.0
Linnick & Fasel (2005)	0.197	1.34±0.044	±0.69	-
Taira & Colonius (2007)	0.196	1.35±0.048	±0.68	1

Table B.2: Comparison of results from the fast-method with previously reported values for unsteady flow around a cylinder at $Re = 200$.

In the tables, speed-up is defined as the time required to compute the last 50 time steps in the simulations normalized by the time elapsed for the original immersed boundary projection method. By measuring the last 50 time steps, we give a conservative estimate for speed-up since the original method is iterative and typically requires many more iterations for earlier times. Thus with $N_g = 4$ the fast method reduces the computational time by a factor of about 15 for the steady flow and 65 for the unsteady flow. We have found similar speed-ups in a variety of problems on which we have tested the code. We note that we have thus far only implemented the fast method in two dimensions (the original algorithm has been validated in both two and three dimensions). Speed-ups for three-dimensional problems are likely to be more dramatic and are to be tested in the near future.

At last, we compare the speed-up from a translating circular cylinder simulated by moving the Lagrangian boundary points. Now Eq. (B.19) is solved iteratively with the conjugate-gradient method. A cylinder originally at the origin at $t = 0$ is impulsively translated to the left with unit velocity with $Re = 200$. The innermost domain is selected as $\mathcal{D}^{(1)} = [-5, 1]\times[-1, 1]$ with $\Delta x/D = 0.02$, and we use $N_g = 4$ multi-domains. Inside this highly confined $\mathcal{D}^{(1)}$, the translating cylinder generates two counter-rotating vortices in the wake as shown in Figure B.5 for $t = 3.5$. The vorticity profile is in accord with previous results reported in Section 2.5 and Taira & Colonius (2007). Compared to a computation performed with the original approach, the present computation is found to be 43.4 times faster. Recall that a speed-up of 53.0 is observed for a stationary cylinder (Table B.2), which suggests that the overall algorithm is still solved efficiently even with a moving immersed boundary.

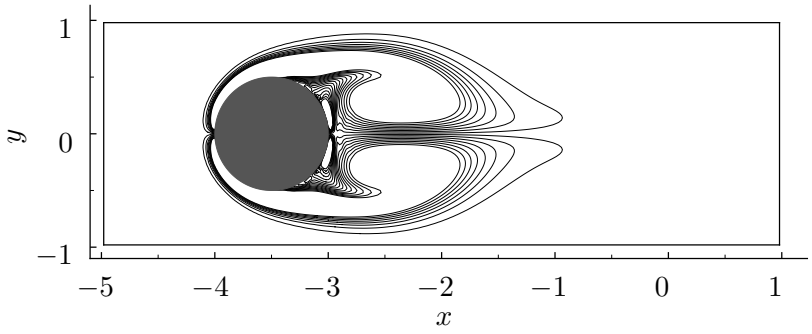

Figure B.5: Vorticity field around an impulsively started cylinder at $t = 3.5$ for $Re = 200$ with contour levels from -3 to 3 in increments of 0.4. The box shows the innermost domain $\mathcal{D}^{(1)}$.

Appendix C

Outflow Boundary Conditions for Incompressible Flows

Numerical simulations of physical phenomena on a unbounded domain are forced to truncate the domain to a computationally feasible size. This truncation introduces a need for artificial boundary conditions along the edge of the truncated domains to allow the physics to freely cross the truncated boundary. The specification of the correct artificial boundary conditions pose a great challenge since the exact artificial boundary conditions in general are *nonlocal in space or in the temporal variable* as Tsynkov (1998) states. General reviews on the artificial boundary conditions can be found in Givoli (1991), Tsynkov (1998), and Hagstrom (1999).

It is also possible to map the computational domain to an unbounded domain for simulations. However, this method suffers from reflective errors if disturbances propagate in the mapped direction. The exiting disturbance will have a finite length scale associated with itself, while this structure would be placed over a largely stretched grid. The numerical method would fail to resolve the wave structures and eventually cause aliasing. This in turn reflects non-physical waves back into the interior of the computational domain. Hence this technique is commonly applied only in the direction normal to the direction of exiting disturbances.

In the field of fluid mechanics, the treatment of domain truncation and development of artificial boundary condition have been extensively investigated in compressible flows and aeroacoustics. We can list a few techniques that have been successful. The nonlinear characteristics method for inviscid hyperbolic systems was introduced by Thompson (1987, 1990) and later extended to viscous flow by Poinsot & Lele (1992). Artificial damping was considered over a buffer zone for the boundary condition proposed by Freund (1997) to damp outgoing disturbances such that the outflow would reach a desired target state. Perfectly matched layer method, originally developed for absorbing electro-magnetic waves (Berenger, 1994), has been applied to inviscid flow by Abarbanel *et al.* (1999) and recently to the nonlinear Euler and Navier-Stokes equations by Hu *et al.* (2008). Spalart (1988) presented fringe methods for solving non-periodic spatially evolving wall-bounded turbulence on a periodic domain by smoothly matching the inflow and the outflow condition. We refer readers to a review article by Colonius (2004) on compressible artificial boundary treatments.

In contrast to the large amount of research performed on compressible artificial boundary conditions, not much attention has been paid to those of incompressible flows. Incompressible flows on unbounded domains have mostly been modeled with the use of some local artificial boundary conditions. Presently, the most popular incompressible outflow boundary condition seems to be the *convective boundary condition* and is known to perform quite well. However, there is a mathematical dilemma that the exact boundary condition should be *global* in time and space. The convective boundary condition and its variants do not seem to overcome this dilemma and suffer from instability as the strength of the exiting disturbance or the nonlinearity becomes strong. Sani & Gresho (1994) reviewed a number of incompressible boundary conditions and noted that further research is necessary for deeper understanding.

A recent paper by Colonius & Ran (2002) proposed a novel alternative to the artificial boundary conditions for compressible flow. While traditional methods have placed their emphasis on wave analysis or domain mappings, Colonius and

Ran approached the problem in an analogous manner to the sub-grid-scale models in turbulence. The governing equations can be modified to account for the physics on the unbounded domain. This can be achieved by windowing the governing equations (filtering in real space) and providing a model for the far-field disturbances (Colonius & Ran, 2002). The model was referred as the super-grid-scale model since the flow structures of interest are too large to fit on the computational domain. The super-grid-scale model is based on techniques used in Large Eddy Simulations (LES), in which the the Navier-Stokes equations are filtered in wave space and a tensor-diffusivity model (sub-grid scale) is used to represent filtered products (Meneveau & Katz, 2000; Pope, 2000).

The super-grid-scale model is not limited to its use on simulations of compressible flows but can also be extended to incompressible flows. Using a windowing function, $h(\mathbf{x})$, for the filtering operation and performing some manipulations following Colonius & Ran (2002), the vorticity transport equation can be modified. An example of the windowing function is illustrated in Figure C.1. The resulting governing equations with the super-grid-scale model become:

$$\frac{\partial \omega_k}{\partial t} + \sum_{j=1}^{3} \left(h_j + (\Delta x_j)^2 h_j'' \right) \frac{\partial F_{jk}(\boldsymbol{\omega})}{\partial x_j} = 2U_\infty \sum_{j=1}^{3} (\Delta x_j)^2 \left| h_j' \right| \frac{\partial^2 \omega_k}{\partial x_j^2} + \nu \frac{\partial^2 \omega_k}{\partial x_j \partial x_j}, \tag{C.1}$$

where

$$\frac{\partial F_{jk}(\boldsymbol{\omega})}{\partial x_j} \equiv \frac{\partial}{\partial x_j} \left(u_j \omega_k - \omega_j u_k \right). \tag{C.2}$$

The velocity field in the above equation is retrieved from the Poisson equation of

$$\nabla^2 \mathbf{u} = -\nabla \times \boldsymbol{\omega}, \tag{C.3}$$

which is trivial to solve in Fourier space for periodic domains. Note that the solution to the above system does indeed satisfy the incompressibitily constraint. Equation (C.1) is modified to window the spatial domain and to damp out the exiting disturbances with the added terms on the right-hand side. For further details on deriving the above equation, readers should consult Colonius

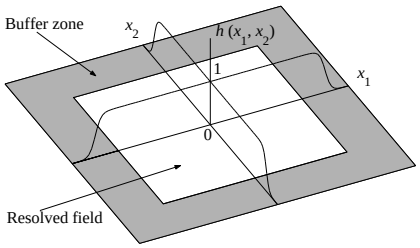

Figure C.1: An example of a two-dimensional windowing function $h(x_1, x_2)$. The windowing function takes $h = 1$ in the resolved field whereas $0 \leq h < 1$ in the shaded buffer zone.

& Ran (2002), which develops a super-grid-scale model for a general conservation equation. This model is global in space due to the nature of the operation and can be with used with the Fourier spectral method, which makes the overall method attractive due to its spectral accuracy.

In future work, it would be interesting to see if one can improve upon the current choice of outflow boundary condition in the immersed boundary solver. Here we briefly present a comparison of (*i*) the convective boundary condition, which was used in Chapter 2:

$$\frac{\partial \mathbf{u}}{\partial t} + U_\infty \frac{\partial \mathbf{u}}{\partial x} = 0, \tag{C.4}$$

(*ii*) the boundary condition by Jin & Braza (1993), derived from splitting the wave operator and finding its analogy for the incompressible Navier-Stokes equations:

$$\frac{\partial u_1}{\partial t} + u_1 \frac{\partial u_1}{\partial x_1} - \nu \frac{\partial^2 u_1}{\partial x_2^2} = 0 \quad \text{and} \quad \frac{\partial u_2}{\partial t} + u_1 \frac{\partial u_2}{\partial x_1} - \nu \frac{\partial^2 u_2}{\partial x_2^2} = 0, \tag{C.5}$$

and (*iii*) the super-grid-scale model. For numerical examples in Chapter 2, any errors associated with this boundary condition were kept away from the inner domain by employing grid stretching for the region away from the immersed body of interest.

Let us consider a two-dimensional example of convection of 50 randomly generated Taylor vortices in a square domain. The background flow is superposed

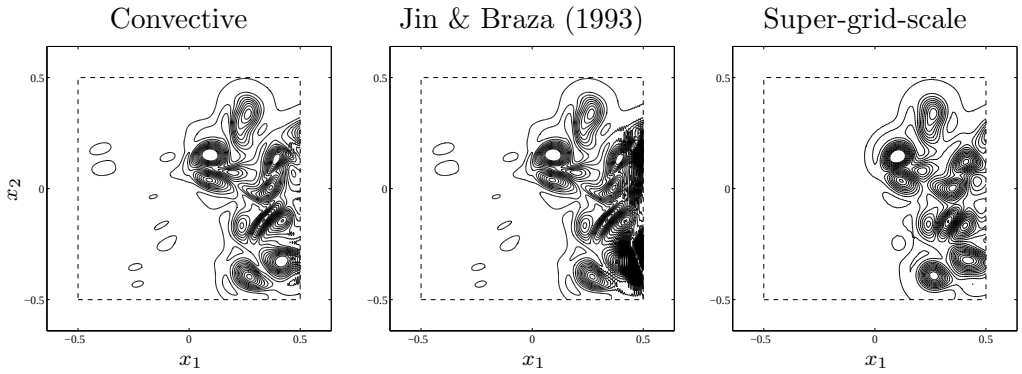

Figure C.2: Comparison of the vorticity fields with the use of different outflow boundary conditions at $t = 0.5$.

from left to right with $U_\infty = 1$. The domain is taken to be unit length in each direction and is shown with the dashed square in Figure C.2. There is a buffer zone surrounding the resolved field shown between the dashed and solid boxes. The computations for the boundary conditions of (*i*) and (*ii*) are performed over the larger solid box as well. Solutions are shown only in the resolved field to compare the two local boundary conditions with the super-grid-scale model with some fairness. For (*i*) and (*ii*), a second-order staggered-grid finite-volume method is used with second-order temporal accuracy. The super-grid-scale solver employs the Fourier spectral collocation method with the fourth-order Runge–Kutta time integration. In all cases there are 100 points across the resolved field in each direction and the viscosity is set to $\nu = 10^{-4}$.

Comparison of the vorticity fields at $t = 0.5$ show that the local boundary conditions of (*i*) and (*ii*) exhibit spatial oscillations in the vicinity of the outflow boundary. In contrast, the flow field obtained with the use of the super-grid-scale model remains free of spatial oscillations developing at the boundary. Hence it would seem attractive to use such a model in future extension of the immersed boundary method. Moreover, the super-grid-scale model was able to convect strong vortices (that induces flow back into the domain from the buffer) out of the computational domain without significant errors. Local boundary conditions

were not able to handle such strong exiting disturbances.

Nonetheless all three boundary conditions considered here suffer from the elliptic nature of the incompressible flow. Any finite truncation of the computational domain results in an error caused by the algebraically decaying potential flow field induced by an object in the domain or a non-zero circulation ($1/r$ decay in the velocity field). Hence, on top of the outflow boundary condition, it would be necessary to apply a correction to account for the slowly decaying incompressible flow field either with the use of the multi-domain approach used in Appendix B or with a method by Rennich & Lele (1997) that computes and patches the correct far-field velocity field analytically. The multi-domain approach does indeed place the outflow boundary far from the domain of interest but cannot damp out exiting perturbations, which again would prompt the use of a better outflow boundary condition on the largest domain. For the low-Reynolds-number flows considered in this thesis, the error associated with the far-field or outflow boundary conditions were not much of a concern. However, use of the current boundary conditions (namely the convective and stress-free boundary conditions) with the immersed-boundary or any incompressible flow solver at much higher Reynolds number may be problematic since additional unstable modes may be excited to alter the flow unintentionally as warned by Pradeep & Hussain (2004).

Appendix D

Experimental Setup

In this appendix, we describe the experimental setup used for the validation of the numerical simulations presented in Section 3.2.2. We acknowledge that the companion experiments were performed by Dr. William B. Dickson (Bioengineering, California Institute of Technology). Previous experiments conducted with the same setup have been reported in Dickson & Dickinson (2004).

The experiments were carried out in a tow-tank ($1m \times 2.4m \times 1.2m$) filled with mineral oil in which a rectangular flat plate of dimension $88mm \times 164mm \times 3mm$ ($AR = 2$) is translated. Setup of the experiment is illustrated in Figure D.1. The mineral oil has density of $\rho = 0.88 \times 10^3\, kg\, m^{-3}$ and kinematic viscosity of $\nu = 115\, cSt$ at room temperature (Chevron Superla® white oil, Texaco Corporation). The flat plate is rigidly mounted to a six-axis force sensor at one wing tip to limit lift due to backlash in the gearbox. This setup is attached to a translation sled equipped with a servo motor providing control of the translational velocity. A constant translation velocity is maintained by the plate after an initial swift ramping acceleration from rest. Based on the constant translational velocity the Reynolds number is $Re = U_{\text{trans}} c/\nu = 100$.

Stereo digital particle image velocimetry (DPIV) (Poelma *et al.*, 2006) was used to quantify the flow field around the plate at several spanwise positions with a vector field size of 57×82. Slices of the flow field are captured from the midspan

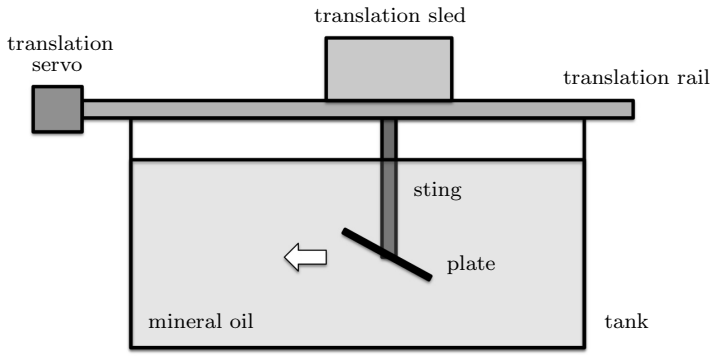

Figure D.1: Setup of the tow-tank experiment.

to $0.22c$ off the wing tip at eleven locations.

In Section 3.2.2, the vorticity fields from the DPIV measurements and the numerical simulations are compared and are found to be in good agreement (Figures 3.2 and 3.3). Furthermore, the steady lift and drag coefficients measured from experiments and simulations also were in good accord (Figure 3.4).

Bibliography

Abarbanel, S., Gottlieb, D. & Hesthaven, J. S. 1999 Well-posed perfectly matched layers for advective acoustics. *J. Comput. Phys.* **154**, 266–283.

Ahuja, S. & Rowley, C. W. 2008 Low-dimensional models for feedback stabilization of unstable steady states. *AIAA Paper 2008-553*.

Ahuja, S., Rowley, C. W., Kevrekidis, I. G., Colonius, T. & Tadmor, G. 2007 Low-dimensional models for control of leading-edge vortices: equilibria and linearized models. *AIAA Paper 2007-709*.

Anderson, J. D. 1999 *Aircraft performance and design*. Boston: McGraw-Hill.

Atta, E. 1981 Component-adaptive grid interfacing. *AIAA Paper 81-0382*.

Baker, T. J. 2005 Mesh generation: Art or science? *Prog. Aero. Sci.* **41**, 29–63.

Bar-Lev, M. & Yang, H. T. 1997 Initial flow field over an impulsively started circular cylinder. *J. Fluid Mech.* **72(4)**, 625–647.

Belov, A., Martinelli, L. & Jameson, A. 1995 A new implicit algorithm with multigrid for unsteady incompressible flow calculations. *AIAA Paper 95-0049*.

Berenger, J. P. 1994 A perfectly matched layer for the absorption of electromagnetic waves. *J. Comput. Phys.* **114**, 185–200.

Beyer, R. P. & LeVeque, R. J. 1992 Analysis of a one-dimensional model for the immersed boundary method. *SIAM J. Numer. Anal.* **29(2)**, 332–364.

Birch, J. M. & Dickinson, M. H. 2001 Spanwise flow and the attachment of the leading-edge vortex on insect wings. *Nature* **412**, 729–733.

Birch, J. M., Dickson, W. B. & Dickinson, M. H. 2004 Force production and flow structure of the leading edge vortex on flapping wings at high and low Reynolds numbers. *J. Exp. Biol.* **207**, 1063–1072.

Blondeaux, P., Fornarelli, F., Guglielmini, L., Triantafyllou, M. S. & Verzicco, R. 2005 Numerical experiments on flapping foils mimicking fish-like locomotion. *Phys. Fluids* **17**, 113601.

Bochev, P. & Lehoucq, R. B. 2005 On the finite element solution of the pure Neumann problem. *SIAM Rev.* **47(1)**, 50–66.

Bos, F. M., Lentink, D., Van Oudheusden, B. W. & Bijl, H. 2008 Influence of wing kinematics on aerodynamic performance in hovering insect flight. *J. Fluid Mech.* **594**, 341–368.

Braza, M., Faghani, D. & Persillon, H. 2001 Successive stages and role of natural vortex dislocations in three-dimensional wake transition. *J. Fluid Mech.* **439**, 1–41.

Brown, D. L., Cortez, R. & Minion, M. L. 2001 Accurate projection methods for the incompressible Navier-Stokes equations. *J. Comput. Phys.* **168**, 464–499.

Buchholz, J. H. J. & Smits, A. J. 2006 On the evolution of the wake structure produced by a low-aspect-ratio pitching panel. *J. Fluid Mech.* **546**, 433–443.

Cain, A. B., Ferziger, J. H. & Reynolds, W. C. 1984 Discrete orthogonal function expansions for non-uniform grids using the fast Fourier transform. *J. Comput. Phys.* **56**, 272–286.

Campbell, J. F. 1976 Augmentation of vortex lift by spanwise blowing. *J. Aircraft* **13(9)**, 727–732.

Carr, L. W. 1988 Progress in analysis and prediction of dynamic stall. *J. Aircraft* **25(1)**, 6–17.

Chang, W., Giraldo, F. & Perot, B. 2002 Analysis of an exact fractional step method. *J. Comput. Phys.* **180**, 183–199.

Choi, H., Jeon, W.-P. & Kim, J. 2008 Control of flow over a bluff body. *Annu. Rev. Fluid Mech.* **40**, 113–139.

Chorin, A. J. 1967 A numerical method for solving incompressible viscous flow problems. *J. Comput. Phys.* **2(1)**, 12–26.

Chorin, A. J. 1968 Numerical solution of the Navier-Stokes equations. *Math. Comput.* **22**, 745–762.

Codina, R. 2001 Pressure stability in fractional step finite element methods for incompressible flows. *J. Comput. Phys.* **170**, 112–140.

Collins, W. M. & Dennis, S. C. R. 1973 Flow past an impulsively started circular cylinder. *J. Fluid Mech.* **60(1)**, 105–127.

Colonius, T. 2004 Modeling artificial boundary conditions for compressible flow. *Annu. Rev. Fluid Mech.* **36**, 315–345.

Colonius, T. & Ran, H. 2002 A super-grid-scale model for simulating compressible flow on unbounded domains. *J. Comput. Phys.* **182**, 191–212.

Colonius, T. & Taira, K. 2008 A fast immersed boundary method using a nullspace approach and multi-domain far-field boundary conditions. *Comput. Methods Appl. Mech. Engrg.* **197**, 2131–2146.

Cosyn, P. & Vierendeels, J. 2006 Numerical investigation of low-aspect-ratio wings at low Reynolds numbers. *J. Aircraft* **43(3)**, 713–722.

Cottet, G., Koumoutsakos, P. & Salihi, M. L. O. 2000 Vortex methods with spatially varying cores. *J. Comput. Phys.* **162**, 164–185.

Coutanceau, M. & Bouard, R. 1977*a* Experimental determination of the main features of the viscous flow in the wake of a circular cylinder in uniform translation. Part 1. Steady flow. *J. Fluid Mech.* **79(2)**, 231–256.

Coutanceau, M. & Bouard, R. 1977*b* Experimental determination of the main features of the viscous flow in the wake of a circular cylinder in uniform translation. Part 2. Unsteady flow. *J. Fluid Mech.* **79(2)**, 257–272.

Dennis, S. C. R. & Chang, G. 1970 Numerical solutions for steady flow past a circular cylinder at Reynolds number up to 100. *J. Fluid Mech.* **42(3)**, 471–489.

Dickinson, M. H. & Götz, K. G. 1993 Unsteady aerodynamic performance of model wings at low Reynolds numbers. *J. Exp. Biol.* **174**, 45–64.

Dickson, W. B. & Dickinson, M. H. 2004 The effect of advance ratio on the aerodynamics of revolving wings. *J. Exp. Biol.* **207**, 4269–4281.

Dong, H., Mittal, R. & Najjar, F. M. 2006 Wake topology and hydrodynamic performance of low-aspect-ratio flapping foils. *J. Fluid Mech.* **566**, 309–343.

Drucker, E. G. & Lauder, G. V. 1999 Locomotor forces on a swimming fish: three dimensional vortex wake dynamics quantified using digital particle image velocimetry. *J. Exp. Biol.* **202**, 2393–2412.

Duraisamy, K. & Baeder, J. D. 2006 Numerical simulation of the effects of spanwise blowing on tip vortex formation. *J. Aircraft* **43(4)**, 996–1006.

Ellington, C. P., van den Berg, C., Willmott, A. P. & Thomas, A. L. R. 1996 Leading-edge vortices in insect flight. *Nature* **384**, 626–630.

Englar, R. J. 2000 Circulation control pneumatic aerodynamics: blown force and moment augmentation and modification; past, present & future. *AIAA Paper 2000-2541.*

Fadlun, E. A., Verzicco, R., Orlandi, P. & Mohd-Yusof, J. 2000 Combined immersed-boundary finite-difference methods for three-dimensional complex flow simulations. *J. Comput. Phys.* **161**, 35–60.

Freund, J. B. 1997 Proposed inflow/outflow boundary condition for direct computation of sound. *AIAA J.* **35(4)**, 740–742.

Freymuth, P., Finaish, F. & Bank, W. 1987 Further visualization of combined wing tip and starting vortex systems. *AIAA J.* **25(9)**, 1153–1159.

Gharib, M., Rambod, E. & Shariff, K. 1998 A universal time scale for vortex ring formation. *J. Fluid Mech.* **360**, 121–140.

Givoli, D. 1991 Non-reflecting boundary conditions. *J. Comput. Phys.* **94(1)**, 1–29.

Glowinski, R., Pan, T. W. & Périaux, J. 1998 Distributed Lagrange multiplier methods for incompressible viscous flow around moving rigid bodies. *Comput. Methods Appl. Mech. Engrg.* **151**, 181–194.

Goldstein, D., Handler, R. & Sirovich, L. 1993 Modeling a no-slip flow boundary with an external force field. *J. Comput. Phys.* **105**, 354–366.

Greenblatt, D., Neuburger, D. & Wygnanski, I. 2001 Dynamic stall control by intermittent periodic excitation. *J. Aircraft* **38(1)**, 188–190.

Guermond, J.-L. & Quartapelle, L. 1998 On stability and convergence of projection methods based on pressure Poisson equation. *Int. J. Numer. Meth. Fluids* **26**, 1039–1053.

Gursul, I., Gordnier, R. & Visbal, M. 2005 Unsteady aerodynamics of nonslender delta wings. *Prog. Aero. Sci.* **41**, 515–557.

Hagstrom, T. 1999 Radiation boundary conditions for the numerical simulation of waves. *Acta Numerica* **8**, 47–106.

Hall, C. A. 1985 Numerical solution of Navier-Stokes problems by the dual variable method. *SIAM J. Alg. Disc. Meth.* **6(2)**, 220–236.

Hamdani, H. & Sun, M. 2000 Aerodynamic forces and flow structures of an airfoil in some unsteady motions at small Reynolds number. *Acta Mech.* **145**, 173–187.

Helmbold, H. B. 1942 Der unverwundene ellipsenflugel als tragende flanche. *Jahrbuch 1942 der Deutch Luftfahrtforsch* pp. I111–I113.

Holloway, A. G. L. & Richardson, S. 2007 Development of a trailing vortex formed with spanwise tip jets. *J. Aircraft* **44(3)**, 845–857.

Hornung, H. 1989 Vorticity generation and transport. 10th Australasian fluid mechanics conference, *Paper KS-3*.

Hu, F. Q., Li, X. D. & Li, D. K. 2008 Absorbing boundary conditions for nonlinear Euler and Navier-Stokes equations based on the perfectly matched layer technique. *J. Comput. Phys.* **227(9)**, 4398–4424.

Hunt, J. C. R., Wray, A. A. & Moin, P. 1988 Eddies, stream, and convergence zones in turbulent flows. *Tech. Rep.* CTR-S88. Center for Turbulent Research.

Jeon, D. & Gharib, M. 2004 On the relationship between the wake vortex formation process and cylinder wake vortex patterns. *J. Fluid Mech.* **519**, 161–181.

Jin, G. & Braza, M. 1993 A nonreflecting outlet boundary condition for incompressible unsteady Navier-Stokes calculations. *J. Comput. Phys.* **107**, 239–253.

Joe, W. T., Taira, K., Colonius, T., MacMynowski, D. G. & Tadmor, G. 2008 Closed-loop control of vortex shedding on a two-dimensional flat-plate airfoil at a low Reynolds number. *AIAA Paper 2008-634*.

Johnson, T. A. & Patel, V. C. 1999 Flow past a sphere up to a Reynolds number of 300. *J. Fluid Mech.* **378**, 19–70.

Kim, J., Kim, D. & Choi, H. 2001 An immersed-boundary finite-volume method for simulations of flow in complex geometries. *J. Comput. Phys.* **171(1)**, 132–150.

Kim, J. & Moin, P. 1985 Application of a fractional-step method to incompressible Navier-Stokes equations. *J. Comput. Phys.* **59**, 308–323.

Koumoutsakos, P. & Leonard, A. 1995 High-resolution simulations of the flow around an impulsively started cylinder using vortex methods. *J. Fluid Mech.* **296**, 1–38.

Lai, M. & Peskin, C. S. 2000 An immersed boundary method with formal second-order accuracy and reduced numerical viscosity. *J. Comput. Phys.* **160**, 705–719.

Lee, C. S., Tavella, D., Woods, N. J. & Roberts, L. 1989 Flow structure and scaling laws in lateral wing-tip blowing. *AIAA J.* **27(8)**, 1002–1007.

Lee, L. & LeVeque, R. J. 2003 An immersed interface method for incompressible Navier-Stokes equations. *SIAM J. Sci. Comput.* **25(3)**, 832–856.

Linnick, M. N. & Fasel, H. F. 2005 A high-order immersed interface method for simulating unsteady incompressible flows on irregular domains. *J. Comput. Phys.* **204**, 157–192.

Liu, C., Zheng, X. & Sung, C. H. 1998 Preconditioned multigrid methods for unsteady incompressible flows. *J. Comput. Phys.* **139**, 35–57.

Marchuk, G. I. 1975 *Methods of numerical mathematics*. Springer-Verlag.

Meneveau, C. & Katz, J. 2000 Scale-invariance and turbulence models for large-eddy simulation. *Annu. Rev. Fluid Mech.* **32**, 1–32.

Milano, M. & Gharib, M. 2005 Uncovering the physics of flapping flat plates with artificial evolution. *J. Fluid Mech.* **534**, 403–409.

Mittal, R. & Iaccarino, G. 2005 Immersed boundary methods. *Annu. Rev. Fluid Mech.* **37**, 239–261.

Mittal, S. & Tezduyar, T. E. 1995 Parallel finite element simulation of 3D incompressible fluid-structure interactions. *Int. J. Numer. Meth. Fluids* **21**, 933–953.

Mohd-Yusof, J. 1997 Combined immersed-boundary/B-spline methods for simulations of flow in complex geometries. *Tech. Rep.* Annual Research Briefs, 317-327. Center for Turbulence Research.

Mori, Y. & Peskin, C. S. 2008 Implicit second-order immersed boundary methods with boundary mass. *Comput. Methods Appl. Mech. Engrg.* **197**, 2049–2067.

Mueller, T. J., ed. 2001 *Fixed and flapping wing aerodynamics for micro air vehicle applications*, *Progress in Astronautics and Aeronautics*, vol. 195. AIAA.

Mueller, T. J. & DeLaurier, J. D. 2003 Aerodynamics of small vehicles. *Annu. Rev. Fluid Mech.* **35**, 89–111.

Newren, E. P., Fogelson, A. L., Guy, R. D. & Kirby, R. M. 2007 Unconditionally stable discretizations of the immersed boundary equations. *J. Comput. Phys.* **222**, 702–719.

Nocedal, J. & Wright, S. J. 1999 *Numerical optimization*. Springer.

Parker, K., von Ellenrieder, K. D. & Soria, J. 2007 Morphology of the forced oscillatory flow past a finite-span wing at low Reynolds number. *J. Fluid Mech.* **571**, 327–357.

Pelletier, A. & Mueller, T. J. 2000 Low Reynolds number aerodynamics of low-aspect-ratio, thin/flat/cambered-plate wings. *J. Aircraft* **37(5)**, 825–832.

Perot, J. B. 1993 An analysis of the fractional step method. *J. Comput. Phys.* **108**, 51–53.

Peskin, C. S. 1972 Flow patterns around heart valves: a numerical method. *J. Comput. Phys.* **10**, 252–271.

Peskin, C. S. 1977 Numerical analysis of blood flow in the heart. *J. Comput. Phys.* **25**, 220–252.

Peskin, C. S. 2002 The immersed boundary method. *Acta Numerica* **11**, 479–517.

Pines, D. J. & Bohorquez, F. 2006 Challenges facing future micro-air-vehicle development. *J. Aircraft* **34(2)**, 290–305.

Poelma, C., Dickson, W. B. & Dickinson, M. H. 2006 Time-resolved reconstruction of the full velocity field around a dynamically-scaled flapping wing. *Exp. Fluids* **41**, 213–225.

Poinsot, T. J. & Lele, S. K. 1992 Boundary conditions for direct simulations of compressible viscous flows. *J. Comput. Phys.* **101**, 104–129.

Pope, S. B. 2000 *Turbulent Flows*. New York: Cambridge Univ. Press.

Pradeep, D. S. & Hussain, F. 2004 Effects of boundary condition in numerical simulations of vortex dynamics. *J. Fluid Mech.* **516**, 115–124.

Press, W. H., Teukolsky, S. A., Vetterling, W. T. & Flannery, B. P. 1992 *Numerical Recipes in FORTRAN: the art of scientific computing*, 2nd edn. Cambridge Univ. Press.

Pullin, D. I. & Wang, Z. J. 2004 Unsteady forces on an accelerating plate and application to hovering insect flight. *J. Fluid Mech.* **509**, 1–21.

Rennich, S. C. & Lele, S. K. 1997 Numerical method for incompressible vortical flows with two unbounded directions. *J. Comput. Phys.* **137**, 101–129.

Ringuette, M. J., Milano, M. & Gharib, M. 2007 Role of the tip vortex in the force generation of low-aspect-ratio normal flat plates. *J. Fluid Mech.* **581**, 453–468.

Roma, A. M., Peskin, C. S. & Berger, M. J. 1999 An adaptive version of the immersed boundary method. *J. Comput. Phys.* **153**, 509–534.

Roshko, A. 1954 On the development of turbulent wakes from vortex streets. *Tech. Rep.* Report 1191. NACA.

Sani, R. L. & Gresho, P. M. 1994 Résumé and remarks on the open boundary condition minisymposium. *Int. J. Numer. Meth. Fluids* **18**, 983–1008.

Seifert, A., Darabi, A. & Wygnanski, I. 1996 Delay of airfoil stall by periodic excitation. *J. Aircraft* **33(4)**, 691–698.

Shyy, W., Lian, Y., Tang, J., Viieru, D. & Liu, H. 2008 *Aerodynamics of low Reynolds number flyers*. New York: Cambridge Univ. Press.

Sirovich, L. 1987 Turbulence and the dynamics of coherent structures, Parts I–III. *Q. Appl. Math.* **XLV**, 561–590.

Spalart, P. R. 1988 Direct numerical study of leading edge contamination, in *fluid dynamics of three-dimensional turbulent shear flows and transition* (AGARD, Cesme, Turkey) **68**, 5.1.

Spalart, P. R. 1998 Airplane trailing vortices. *Annu. Rev. Fluid Mech.* **30**, 107–138.

Strikwerda, J. C. & Lee, Y. S. 1999 The accuracy of the fractional step method. *SIAM J. Numer. Anal.* **37(1)**, 37–47.

Sun, M. 2005 High-lift generation and power requirements of insect flight. *Fluid Dyn. Res.* **37**, 21–39.

Sunada, S., Yasuda, T., Yasuda, K. & Kawachi, K. 2002 Comparison of wing characteristics at an ultralow Reynolds number. *J. Aircraft* **39(2)**, 331–338.

Taira, K. & Colonius, T. 2007 The immersed boundary method: a projection approach. *J. Comput. Phys.* **225**, 2118–2137.

Taira, K. & Colonius, T. 2008 Three-dimensional separated flows around low-aspect-ratio flat plates. *J. Fluid Mech.* **submitted**.

Taira, K., Dickson, W. B., Colonius, T., Dickinson, M. H. & Rowley, C. W. 2007 Unsteadiness in flow over a flat plate at angle-of-attack at low Reynolds numbers. *AIAA Paper 2007-710*.

Témam, R. 1969 Sur l'approximation de la solution des équations de Navier-Stokes par la méthode des pas fractionnaires (I). *Arch. Rat. Mech. Anal.* **32(2)**, 135–153.

Thompson, K. W. 1987 Time-dependent boundary conditions for hyperbolic systems. *J. Comput. Phys.* **68**, 1–24.

Thompson, K. W. 1990 Time-dependent boundary conditions for hyperbolic systems, II. *J. Comput. Phys.* **89**, 439–461.

Torres, G. E. & Mueller, T. J. 2004 Low-aspect-ratio wing aerodynamics at low Reynolds numbers. *AIAA J.* **42(5)**, 865–873.

Tritton, D. J. 1959 Experiments on the flow past a circular cylinder at low Reynolds number. *J. Fluid Mech.* **6**, 547–567.

Tsynkov, S. V. 1998 Numerical solution of problems on unbounded domains. A review. *Appl. Numer. Math.* **27**, 465–532.

Usherwood, J. R. & Ellington, C. P. 2002 The aerodynamics of revolving wings, I model hawkmoth wings. *J. Exp. Biol.* **205**, 1547–1564.

von Ellenrieder, K. D., Parker, K. & Soria, J. 2003 Flow structures behind a heaving and pitching finite-span wing. *J. Fluid Mech.* **490**, 129–138.

Wang, Z. J. 2000*a* Two dimensional mechanism for insect hovering. *Phys. Rev. Let.* **85(10)**, 2216–2219.

Wang, Z. J. 2000*b* Vortex shedding and frequency selection in flapping flight. *J. Fluid Mech.* **410**, 323–341.

Wang, Z. J. 2004 The role of drag in insect hovering. *J. Exp. Biol.* **207**, 4147–4155.

Winkelmann, A. E. & Barlow, J. B. 1980 Flowfield model for a rectangular planform wing beyond stall. *AIAA J.* **18(8)**, 1006–1007.

Yanenko, N. N. 1971 *The method of fractional steps: the solution of problems of mathematical physics in several variables*. Springer-Verlag.

Yon, S. A. & Katz, J. 1998 Study of the unsteady flow features on a stalled wing. *AIAA J.* **36(3)**, 305–312.

Zhu, Q., Wolfgang, M. J., Yue, D. K. P. & Triantafyllou, M. S. 2002 Three-dimensional flow structures and vorticity control in fish-like swimming. *J. Fluid Mech.* **468**, 1–28.